UNIVERSITAT POLITÈCNICA DE VALÈNCIA

I.U.I. CMT - Clean Mobility & Thermofluids

DOCTORAL THESIS:

"Analysis of the internal thermofluid-dynamics in a uniflow scavenged engine"

Presented by: ADITYA DARBHAMALLA
Supervised by: DR. HÉCTOR CLIMENT PUCHADES

in fulfillment of the requirements for the degree of

Doctor of Philosophy

Valencia, February 2024

Doctoral Thesis

"Analysis of the internal thermofluid-dynamics in a uniflow scavenged engine"

Presented by: ADITYA DARBHAMALLA
Supervised by: DR. HÉCTOR CLIMENT PUCHADES

THESIS EXAMINERS

DR. CHAITANYA PATIL
DR. JACOBO PORTEIRO FRESCO
DR. XAVIER TAUZIA

DEFENSE COMMITTEE

Chairman: DR. JOSÉ GALINDO LUCAS
Secretary: DR. FRANCISCO VERA GARCIA
Member: DR. CHAITANYA PATIL

Valencia, February 2024

Abstract

Transportation on land is one of the major contributors to emissions and has an impact on climatic changes and health hazards. To address these issues, the automotive industry is moving toward sustainable mobility, where new technologies such as hybrid vehicles and electric vehicles are being assessed. However, given the lack of competence in fossil fuel-free alternatives for electricity production, dependence on internal combustion engines (ICEs) to be used as range extenders and electricity production is being addressed. These range extenders are usually two-stroke engines. Due to their design and operating range, these ICEs can be compact, be heavily downsized, and have fewer emissions. Hence it is essential to understand the performances of these new ICE concepts, showcase potential benefits, and aid in further improvements.

Aiming towards the above objective in this thesis work a two-stroke uniflow scavenged engine concept is assessed. Experimental data from an engine test cell using two exhaust layouts, three engine speeds, and two load conditions is obtained. A 1D gas dynamic model is developed and validated against all tested points. A 3D replica of the engine is modeled and used in 3D CFD simulation. Fluid dynamically validated 1D model results are used as initial and boundary conditions to assess the thermal and scavenging metrics of this particular engine. On comparing 1D and CFD results, it was observed that temperature and short-circuiting of air were not well captured using state-of-the-art heat transfer and scavenging models during the scavenging process. This led to the proposal of a new heat transfer model and a synthetic scavenging curve.

In-cylinder heat transfer is a phenomenon that affects the temperature of burnt gases and fresh air in an internal combustion engine. Compared to the four-stroke units, this influence is more critical in two-stroke engines during the scavenging process since gas velocity filed inside the cylinder evolves rapidly in space and time. This study proposes a new convective heat transfer coefficient model beyond those based on Reynolds number calculation with the piston mean velocity. The model uses semi-empirical equations with non-dimensional numbers since it has to be integrated within the frame of a physical engine model, where thermo and fluid dynamic properties of the gases inside the engine are solved using 0D or 1D approaches. In this particular application, the temperature deviation led to a poor prediction of trapped mass in the

cylinder. The proposed convective heat transfer coefficient is calculated using a pseudo-velocity of the gases inside the cylinder based on the mass flow rates in the intake and exhaust ports during scavenging.

Scavenging in a two-stroke engine presents a complex process, distinct from the four-stroke cycle, as the intake and exhaust processes occur simultaneously for a significant portion of the gas exchange period. Due to this overlapping nature and shorter gas exchange duration compared to a four-stroke engine, accurately modeling the in-cylinder gas dynamics becomes crucial. This modeling process aims to ensure the effective retention of the fresh charge delivered and the efficient extraction of residual gases from the previous engine cycle during the gas exchange phase. Such modeling is particularly crucial in advanced two-stroke engines to obtain reliable estimations of the trapped mixture composition and predict engine performance accurately.

Comparing 3D CFD results to 1D data, the 1D model showcased robustness in capturing both the heat transfer and gas dynamic phenomena during scavenging process. Furthermore, perspective analysis is performed comparing state-of-the-art models to proposed models for engine performance, depicting the potentiality of the proposed models. On comparing the proposed heat transfer model to the existing heat transfer correlation under similar CFD initial conditions it is observed that the state-of-the-art correlations led to a peak deviation in temperature by 85 °C resulting in a deviation of 12% in trapped mass. On the other hand the proposed heat transfer model showed a peak deviation of 25 °C in temperature and negligible error in trapped mass.

Perspective analysis under similar combustion settings, comparing Woschni heat transfer model and proposed heat transfer correlation showed differences in trapped mass of upto 6%. This translated to a further cooling of the gases inside the cylinder by almost 85 °C resulting in 12% difference in IMEP. A sensitivity analysis is performed to evaluate the impact of the model constants on the engine operation. These constants included both Woschni and the proposed heat transfer correlation during scavenging. In this analysis, coefficient b (correction coefficient of proposed heat transfer correlation) was changed by $\pm 50\%$ from the mean value, and coefficient a (correction coefficient of Woschni heat transfer correlation) was changed by $\pm 42\%$. Results depicted that coefficient b had a more significant impact on trapped mass. A sweep along varying coefficient b and at constant coefficient a can lead to a 15% change in trapped mass. Conversely, a sweep along varying coefficient a and at constant coefficient b can lead to a maximum difference of 5% in trapped mass.

To accurately capture the short-circuiting of air, a synthetic scavenging (SS) model is proposed. The SS curve consists of four characteristic points: the initial point, transition point, anchor point, and target point. The calibrated SS curve is studied to accurately capture the start and peak of the short-circuiting of air. The transition point indicates the start of the short-circuiting, while the anchor point is calibrated to achieve the peaks of short-circuiting, which is influenced by engine speed, load condition, and exhaust configuration. For example, at 2000 RPM with similar combustion, port settings, and load conditions, using config-1 exhaust layout results in a peak short-circuiting of air of 0.22g, while config-2 exhaust layout provides 0.10g of short-circuiting is observed.

The impact of the exhaust manifold layout on the gas behavior inside the cylinder is analyzed, focusing on pressure pulses observed inside the cylinder and exhaust manifold, as well as the mass flow rate in the exhaust. With config-1, higher forward pressure near the exhaust port closing leads to greater gas extraction at the end of the scavenging process is seen. Conversely, with config-2, higher exhaust gases are extracted during the port opening phase, where exhaust gases and fresh charge are not perfectly mixed. This results in lower short-circuiting of air aided by higher exhaust pressure. The lower short-circuiting of air, along with higher trapped mass and constant air-fuel ratio, led to a 19% increase in IMEP.

A sensitivity analysis is conducted by analyzing all the calibrated SS curves and selecting extreme operating conditions (ExC1 and ExC2). Results depict that trapped mass is enhanced by an average of 12% when changing from ExC2 to ExC1. Throughout the operating conditions, an average of 16% change in air mass fraction, 49% reduction in gas mass fraction, and 35% reduction in air short-circuiting are observed. This results in an average increase of 16 points in scavenging efficiency, 11 points in trapping efficiency, and 11 points in charging efficiency.

Keywords: Uniflow scavenged engine; Range extenders; Heat transfer; Scavenging; Two-stroke engine; Thermo-fluids modeling

Resumen

El transporte terrestre es uno de los principales contribuyentes a las emisiones y tiene un impacto en los cambios climáticos y los peligros para la salud. Para abordar estos problemas, la industria automotriz se está moviendo hacia la movilidad sostenible, donde se están evaluando nuevas tecnologías como vehículos híbridos y vehículos eléctricos. Sin embargo, dado la falta de competencia en alternativas libres de combustibles fósiles para la producción de electricidad, se está abordando la dependencia de motores de combustión interna (ICEs) para ser utilizados como extensores de autonomía y producción de electricidad. Estos extensores de autonomía son generalmente motores de dos tiempos. Debido a su diseño y rango de operación, estos ICE pueden ser compactos, tener una gran reducción de tamaño y producir menos emisiones. Por lo tanto, es esencial comprender el rendimiento de estos nuevos conceptos de ICE, mostrar beneficios potenciales y ayudar en mejoras adicionales.

Con el objetivo anterior en este trabajo de tesis, se evalúa un concepto de motor de dos tiempos de barrido uniflow. Se obtienen datos experimentales de una celda de prueba de motor utilizando dos disposiciones de escape, tres velocidades de motor y dos condiciones de carga. Se desarrolla y valida un modelo gasodinámico 1D con respecto a todos los puntos probados. Se modela una réplica en 3D del motor y se utiliza en una simulación CFD en 3D. Los resultados del modelo 1D validados fluidodinámicamente se utilizan como condiciones iniciales y de contorno para evaluar las métricas térmicas y de barrido de este motor en particular. Al comparar los resultados 1D y CFD, se observó que la temperatura y el cortocircuito de aire no se capturaron bien utilizando modelos de transferencia de calor y barrido de última generación durante el proceso de barrido. Esto llevó a la propuesta de un nuevo modelo de transferencia de calor y una curva sintética de barrido.

La transferencia de calor en el cilindro es un fenómeno que afecta la temperatura de los gases quemados y el aire fresco en un motor de combustión interna. En comparación con las unidades de cuatro tiempos, esta influencia es más crítica en los motores de dos tiempos durante el proceso de barrido, ya que el campo de velocidad del gas dentro del cilindro evoluciona rápidamente en el espacio y el tiempo. Este estudio propone un nuevo modelo de coeficiente de transferencia de calor convectivo más allá de aquellos basados en el cálculo del número de Reynolds con la velocidad media del pistón. El modelo utiliza ecuaciones semiempíricas con números adimensionales ya que debe integrar-

se en el marco de un modelo físico de motor, donde las propiedades termo y fluidodinámicas de los gases dentro del motor se resuelven mediante enfoques 0D o 1D. En esta aplicación particular, la desviación de temperatura llevó a una predicción deficiente de la masa atrapada en el cilindro. El coeficiente propuesto se calcula utilizando una pseudo-velocidad de los gases dentro del cilindro basada en las tasas de flujo de masa en los puertos de admisión y escape durante el barrido.

El barrido en un motor de dos tiempos presenta un proceso complejo, distinto del ciclo de cuatro tiempos, ya que los procesos de admisión y escape ocurren simultáneamente durante una parte significativa del período de intercambio de gases. Debido a esta naturaleza superpuesta y a la duración más corta del intercambio de gases en comparación con un motor de cuatro tiempos, modelar con precisión la dinámica de gas dentro del cilindro se vuelve crucial. Este proceso de modelado tiene como objetivo garantizar la retención efectiva de la carga fresca suministrada y la extracción eficiente de los gases residuales del ciclo de motor anterior durante la fase de intercambio de gases. Este modelado es particularmente crucial en motores avanzados de dos tiempos para obtener estimaciones confiables de la composición de la mezcla atrapada y predecir con precisión el rendimiento del motor.

Al comparar los resultados CFD en 3D con los datos 1D, el modelo 1D demostró solidez al capturar tanto los fenómenos de transferencia de calor como los dinámicos de gas durante el proceso de barrido. Además, se realiza un análisis de perspectiva comparando modelos de última generación con modelos propuestos para el rendimiento del motor, demostrando el potencial de los modelos propuestos. Al comparar el modelo propuesto de transferencia de calor con la correlación de transferencia de calor existente bajo condiciones iniciales de CFD similares, se observa que las correlaciones de última generación llevaron a una desviación máxima en la temperatura de 85 °C, lo que resultó en una desviación del 12 % en la masa atrapada. Por otro lado, el modelo propuesto de transferencia de calor mostró una desviación máxima de 25 °C en la temperatura y un error insignificante en la masa atrapada.

En un análisis de perspectiva bajo condiciones de combustión similares, comparando el modelo de transferencia de calor de Woschni y la correlación de transferencia de calor propuesta, se observaron diferencias en la masa atrapada de hasta el 6 %. Esto se tradujo en un enfriamiento adicional de los gases dentro del cilindro en casi 85 °C, lo que resultó en una diferencia del 12 % en el IMEP. Se realiza un análisis de sensibilidad para evaluar el impacto de las

constantes del modelo en la operación del motor. Estas constantes incluyeron tanto Woschni como la correlación de transferencia de calor propuesta durante el barrido. En este análisis, el coeficiente b (coeficiente de corrección de la correlación de transferencia de calor propuesta) se cambió en $\pm 50\%$ desde el valor medio, y el coeficiente a (coeficiente de corrección de la correlación de transferencia de calor de Woschni) se cambió en $\pm 42\%$. Los resultados mostraron que el coeficiente b tenía un impacto más significativo en la masa atrapada. Un barrido variando el coeficiente b y a un coeficiente a constante puede llevar a un cambio del 15\% en la masa atrapada. Por otro lado, un barrido variando el coeficiente a y a un coeficiente b constante puede llevar a una diferencia máxima del 5\% en la masa atrapada.

Para capturar con precisión el cortocircuito de aire, se propone un modelo de barrido sintético (SS). La curva SS consta de cuatro puntos característicos: el punto inicial, el punto de transición, el punto de anclaje y el punto objetivo. La curva SS calibrada se estudia para capturar con precisión el inicio y el pico del cortocircuito de aire. El punto de transición indica el inicio del cortocircuito, mientras que el punto de anclaje se calibra para alcanzar los picos del cortocircuito, que están influenciados por la velocidad del motor, la condición de carga y la configuración del escape. Por ejemplo, a 2000 RPM con una combustión similar, configuraciones de puerto y condiciones de carga, utilizando la disposición de escape config-1 resulta en un pico de cortocircuito de aire de 0.22 g, mientras que la disposición de escape config-2 proporciona 0.10 g de cortocircuito observado.

Se analiza el impacto de la disposición del colector de escape en el comportamiento del gas dentro del cilindro, centrándose en los pulsos de presión observados dentro del cilindro y el colector de escape, así como en la tasa de flujo de masa en el escape. Con la config-1, una mayor presión hacia adelante cerca del cierre del puerto de escape conduce a una mayor extracción de gas al final del proceso de barrido. Por otro lado, con la config-2, se extraen mayores gases de escape durante la fase de apertura del puerto, donde los gases de escape y la carga fresca no están perfectamente mezclados. Esto resulta en un menor cortocircuito de aire ayudado por una mayor presión de escape. El menor cortocircuito de aire, junto con una mayor masa atrapada y una relación aire-combustible constante, condujo a un aumento del 19\% en el IMEP.

Se realiza un análisis de sensibilidad analizando todas las curvas SS calibradas y seleccionando condiciones de operación extremas (ExC1 y ExC2). Los resultados muestran que la masa atrapada se mejora en un promedio del

12 % al cambiar de ExC2 a ExC1. A lo largo de las condiciones de operación, se observa un cambio promedio del 16 % en la fracción de masa de aire, una reducción del 49 % en la fracción de masa de gas y una reducción del 35 % en el cortocircuito de aire. Esto resulta en un aumento promedio de 16 puntos en la eficiencia de barrido, 11 puntos en la eficiencia de trampa y 11 puntos en la eficiencia de carga.

Palabras clave: Motor de barrido uniflow; Extensores de autonomía; Transferencia de calor; Barrido; Motor de dos tiempos; Modelado termo-fluido.

Resum

El transport terrestre és un dels principals contribuents a les emissions i té un impacte en els canvis climàtics i els riscos per a la salut. Per abordar aquests problemes, la indústria automobilística es mou cap a la mobilitat sostenible, on s'estan avaluant noves tecnologies com ara vehicles híbrids i vehicles elèctrics. No obstant això, donada la manca de competència en alternatives lliures de combustibles fòssils per a la producció d'electricitat, s'està abordant la dependència dels motors de combustió interna (ICEs) per ser utilitzats com a extensors d'autonomia i producció d'electricitat. Aquests extensors d'autonomia són normalment motors de dos temps. A causa del seu disseny i rang operatiu, aquests ICEs poden ser compactes, força reduïts de mida, i emetre menys. Per tant, és essencial entendre les actuacions d'aquests nous conceptes de ICE, mostrar els beneficis potencials, i ajudar en millores addicionals.

Amb l'objectiu anterior en aquest treball de tesi, es valora un concepte de motor de dos temps de flux uniflow. S'obtenen dades experimentals d'una cel·la de prova de motor utilitzant dues disposicions d'escapament, tres velocitats de motor i dues condicions de càrrega. Es desenvolupa i valida un model gasodinàmic 1D amb tots els punts provats. Es modela una rèplica en 3D del motor i s'utilitza en una simulació CFD en 3D. Els resultats del model 1D validats fluidodinàmicament s'utilitzen com a condicions inicials i de contorn per avaluar les mètriques tèrmiques i de flux de gas d'aquest motor en particular. En comparar els resultats 1D i CFD, es va observar que la temperatura i el tall-circuit d'aire no es van capturar bé utilitzant models de transferència de calor i flux de gas de última generació durant el procés de flux. Això va portar a la proposta d'un nou model de transferència de calor i una corba sintètica de flux.

La transferència de calor al cilindre és un fenomen que afecta la temperatura dels gasos cremats i l'aire fresc en un motor de combustió interna. En comparació amb les unitats de quatre temps, aquesta influència és més crítica en els motors de dos temps durant el procés de flux, ja que el camp de velocitat del gas dins del cilindre evoluciona ràpidament en l'espai i el temps. Aquest estudi proposa un nou model de coeficient de transferència de calor convectiu més enllà dels basats en el càlcul del número de Reynolds amb la velocitat mitjana del pistó. El model utilitza equacions semiempíriques amb nombres no-dimensionals ja que ha de ser integrat dins del marc d'un model físic de motor, on les propietats termo i fluidodinàmiques dels gasos dins del motor

es resolen mitjançant enfocaments 0D o 1D. En aquesta aplicació particular, la desviació de temperatura va portar a una predicció deficient de la massa atrapada al cilindre. El coeficient de transferència de calor convectiu proposat es calcula utilitzant una pseudo-velocitat dels gasos dins del cilindre basada en les taxes de flux de massa en els ports d'entrada i d'escapament durant el flux.

El flux en un motor de dos temps presenta un procés complex, diferent del cicle de quatre temps, ja que els processos d'admissió i d'escapament ocorren simultàniament durant una part significativa del període d'intercanvi de gasos. A causa d'aquesta naturalesa superposada i de la durada més curta de l'intercanvi de gasos en comparació amb un motor de quatre temps, modelar amb precisió la dinàmica del gas dins del cilindre es torna crucial. Aquest procés de modelatge té com a objectiu assegurar la retenció efectiva de la càrrega fresca lliurada i l'extracció eficient dels gasos residuals del cicle de motor anterior durant la fase d'intercanvi de gasos. Aquest modelatge és particularment crucial en motors avançats de dos temps per obtenir estimacions fiables de la composició de la mescla atrapada i predir amb precisió el rendiment del motor.

Comparant els resultats CFD en 3D amb les dades 1D, el model 1D va mostrar robustesa en capturar tant la transferència de calor com els fenòmens dinàmics de gas durant el procés de flux. A més, es realitza un anàlisi de perspectiva comparant models de última generació amb models proposats pel rendiment del motor, mostrant el potencial dels models proposats. En comparar el model de transferència de calor proposat amb la correlació de transferència de calor existent sota condicions inicials de CFD similars, es va observar que les correlacions de última generació van conduir a una desviació màxima en la temperatura de 85 °C, amb una desviació del 12% en la massa atrapada. D'altra banda, el model de transferència de calor proposat va mostrar una desviació màxima de 25 °C en la temperatura i un error negligible en la massa atrapada.

L'anàlisi de perspectiva sota paràmetres de combustió similars, comparant el model de transferència de calor de Woschni i la correlació de transferència de calor proposada, va mostrar diferències en la massa atrapada d'fins a un 6%. Això es va traduir en un refredament addicional dels gasos dins del cilindre de gairebé 85 °C, amb una diferència del 12% en l'IMEP. Es realitza una anàlisi de sensibilitat per avaluar l'impacte de les constants del model en el funcionament del motor. Aquestes constants van incloure tant Woschni com

la correlació de transferència de calor proposada durant el flux. En aquest anàlisi, el coeficient b (coeficient de correcció de la correlació de transferència de calor proposada) es va canviar en $\pm 50\%$ des del valor mitjà, i el coeficient a (coeficient de correcció de la correlació de transferència de calor de Woschni) es va canviar en $\pm 42\%$. Els resultats van mostrar que el coeficient b tenia un impacte més significatiu en la massa atrapada. Un balanç variant el coeficient b i a un coeficient a constant pot conduir a un canvi del 15% en la massa atrapada. Al contrari, un balanç variant el coeficient a i a un coeficient b constant pot conduir a una diferència màxima del 5% en la massa atrapada.

Per capturar amb precisió el tall-circuit d'aire, es proposa un model sintètic de flux (SS). La corba SS consta de quatre punts característics: el punt inicial, el punt de transició, el punt d'àncora i el punt objectiu. La corba SS calibrada es estudia per capturar amb precisió l'inici i el pic del tall-circuit d'aire. El punt de transició indica l'inici del tall-circuit, mentre que el punt d'àncora es calibrat per assolir els pics del tall-circuit, que estan influïts per la velocitat del motor, la condició de càrrega i la configuració de l'escapament. Per exemple, a 2000 RPM amb una combustió similar, paràmetres de port i condicions de càrrega, utilitzant la disposició de l'escapament config-1 resulta en un pic de tall-circuit d'aire de 0.22 g, mentre que la disposició de l'escapament config-2 proporciona 0.10 g de tall-circuit observat.

S'analitza l'impacte de la disposició del col·lector d'escapament en el comportament del gas dins del cilindre, centrant-se en els polsos de pressió observats dins del cilindre i el col·lector d'escapament, així com en la taxa de flux de massa a l'escapament. Amb la config-1, una major pressió cap endavant prop del tancament del port d'escapament condueix a una major extracció de gas al final del procés de flux. Al contrari, amb la config-2, s'extreuen majors gasos d'escapament durant la fase d'obertura del port, on els gasos d'escapament i la càrrega fresca no estan perfectament barrejats. Això resulta en un menor tall-circuit d'aire ajudat per una major pressió d'escapament. El menor tall-circuit d'aire, juntament amb una major massa atrapada i una relació aire-combustible constant, va conduir a un augment del 19% en l'IMEP.

Es realitza una anàlisi de sensibilitat analitzant totes les corbes SS calibrades i seleccionant condicions d'operació extremes (ExC1 i ExC2). Els resultats mostren que la massa atrapada s'amplifica en un promig del 12% quan es passa de l'ExC2 a l'ExC1. Al llarg de les condicions d'operació, es produeix un canvi mitjà del 16% en la fracció de massa d'aire, una reducció del 49% en la fracció de massa de gas, i una reducció del 35% en el tall-circuit d'aire. Això

resulta en un augment mitjà de 16 punts en l'eficiència de flux, 11 punts en l'eficiència de trampa, i 11 punts en l'eficiència de càrrega.

Paraules clau: Motor d'escombrat uniflow; Extensors d'autonomia; Transferència de calor; Barrido; Motor de dos temps; Modelatge termo-fluid.

List of publications

This thesis is based on the work contained in the following papers:

[1] J. R. Serrano, H. Climent, P. Piqueras, and A. Darbhamalla. "Energy recovery potential by replacing the exhaust gases recirculation valve with an additional turbocharger in a heavy-duty engine". *Energy Conversion and Management* 271 (Nov. 2022), p. 116307. ISSN: 01968904. DOI: 10.1016/j.enconman.2022.116307

[2] J. R. Serrano, H. Climent, A. Gomez-Vilanova, A. Darbhamalla, and S. Guilain. "Assessment of Variable Geometry Orifice Compressor Technology Impact in a New Generation of Compression Ignition Powertrains at Low-End and Transient Operation". *Applied Sciences* 12 (24 Dec. 2022), p. 12869. ISSN: 2076-3417. DOI: 10.3390/app122412869

[3] H. Climent, A. Tiseira, J. Gomez-Soriano, and A. Darbhamalla. "In-Cylinder Heat Transfer Model Proposal Compatible with 1D Simulations in Uniflow Scavenged Engines". *Applied Sciences* 13 (6 Mar. 2023), p. 3996. ISSN: 2076-3417. DOI: 10.3390/app13063996

Acknowledgements

In the first place, I wish to thank Dr. Héctor Climent for sharing his time, knowledge, and valuable guidance through my Ph.D. journey. I would also like to thank all the staff in CMT-Clean Mobility & Thermofluids that make from the research department and home from Monday to Friday. Special remarks to José María Desantes, who opened the doors for me from the first day and welcomed me to the research institute, I will always remember that day. I would like to thank Universitat Politècnica de València for their support with FPI grant with reference FPI-2020-S2-21414.

I would also like to grate my desk colleagues, who made my journey an enjoyable trip that I will always keep in mind. Especially to Rossana, Vishnu, Alejandro, David, Juan, Vitor, and Paulina, with whom I have shared most of my time during the last year. I would also like to thank Chaitanya and Varun, with whom I have shared countless moments, talks, and meetings.

And, of course, to my fan club member made up of my mom and dad, Haripriya and Venugopal, my brother Teja and my wife Nimeshika, to whom I owe all my achievements, happiness, and motivation with which I live every day, I am infinitely grateful to you all.

Valencia, January 2024.

"Dream is not that which you see while sleeping it is something that does not let you sleep."

Dr. A.P.J. Abdul Kalam

Contents

List of Tables

List of Figures

xxviii

List of symbols

Latin characters

a	Correction coefficient of Woschni correlation	
A	Area	m^2
b	Correction coefficient of proposed correlation	
b	Damper coefficient	Ns/m
B	Bore	m
c	Velocity	m/s
C_0, C_1, C_2	Correction coefficients	
c_p, c_v	Heat capacities at constant pressure and volume, respectively	J/kgK
D	Diameter	m
F	Force	N
h	Convective heat transfer coefficient	W/m^2K
IMEP	Indicated mean effective pressure	bar
k	Spring constant	N/m
K	Thermal conductivity	W/mK
m	Mass	g
$\dot{m}$	Mass flow rate	kg/s
Nu	Nusselt number	
p	Pressure	Pascal
Pr	Prandlt number	
$\dot{Q}$	Rate heat released	J/s
Re	Reynolds number	
t	Time	s
T	Temperature	K
U_p	Piston velocity	m/s
V	Volume	m^3
x	Displacement	m
$\dot{x}$	Velocity	m/s
$\ddot{x}$	Acceleration	m/s^2

Greek characters

α	Crank angle
α_0	Crank angle at which the combustion starts
Δ	Variation
$\Delta\alpha$	Combustion duration
k	Constant parameter that replaces the ratio of specific heat
θ	Angle
ρ	Density
μ	Dynamic viscosity

Sub- and Superscripts

$-$	Mean
$*$	Pseudo
$Air, Cylinder$	Air inside the cylinder
$Burnt$	Burnt gases
c	Cylinder
cc	Combustion chamber
$disp$	Displacement
$exhaust$	Exhaust gases
f	Fuel
F	Fluid
fb	fuel burned
$fresh$	Fresh air
g	Gas
i	Respective iterative number
in	Inlet
$in, cylinder$	Inlet of cylinder
out	Outlet
r, ref	Reference
res	Residuals
ret	Retained
$short$	Short-circuit
$trap$	Trapped
w	Combustion chamber wall

Acronyms

0D	Zero dimensional
1D	One dimensional
3D	Three dimensional
AFR	Air-to-Fuel Ratio
AHR	Apparent heat release
AMR	Adaptive mesh refinement
ANN	Artificial neural network
ASU	Air separation unit
BC	Boundary conidition
BDC	Bottom dead center
BEV	Battery electric vehicle
BMEP	Brake mean effective pressure
BSFC	Break specific fuel consumption
CAD	Crank angle degrees
CBR	Cylinder residual ratio
CC	Cubic centimeters
CE	Charging efficiency
CFD	Computational fluid dynamics
CH_4	Methane
CI	Compression ignited
CO	Carbon monoxide
CO_2	Carbon dioxide
Config	Configuration
COV	Coefficient of variation
CR	Compression ratio
DI	Direct injection
DOC	Diesel oxidation catalyst
DPF	Diesel particulate filter
DR	Delivery ratio
EBR	Exhaust residual ratio
ECU	Engine control unit
EGR	Exhaust gas recirculation
ExC	Extreme condition
FL	Full load
FPE	Free-piston engine
GWP	Global warming potential
HC	Hydrocarbon
HCHO	Methanol

HCCI	Homogeneous charge compression ignition
HD	Heavy duty
HDV	Heavy-duty vehicle
HEV	Hybrid electric Vehicle
HRR	Heat release rate
HP-EGR	High pressure EGR
HSDI	High-speed direct injection
IC	Initial condition
ICE	Internal combustion engine
IMEP	Indicated mean effect pressure
LDA	Laser droplet anemometer
LDV	Light-duty vehicle
LES	Large eddy simulation
LPG	Liquefied petroleum gas
LP-EGR	Low pressure EGR
MAPO	Maximum amplitude of pressure oscillations
MIEC	Mixed ionic–electronic conducting
NEDC	New European driving cycle
NH_3	Ammonia
NO_2	Nitrogen dioxide
NO_x	Mono-nitrogen oxides
O_2	Oxygen dioxides
OEM_x	Oxymethylene dimethyl ethers
ORC	Organic Rankine cycles
PD	Perfect displacement
PDF	Pseudo derivative feedback
PISO	Pressure implicit with splitting of operators
PIV	Particle image velocimetry
PL	Partial Load
PM	Perfect mixture
$PODE_x$	Polyoxymethylene dimethyl ether
PSD	Power spectral density
PWM	Pulse width modulation
RANS	Reynolds-Averaged Navier-Stokes
RCCI	Reactivity controlled compression ignition
RDE	Real driving emissions
RMSE	Root mean square error
RPM	Revolution per minute

SE	Scavenging efficiency
SI	Spark ignited
SRC	Solar Rankine cycle
SS	Synthetic scavenging
TC	Turbocharger
TDC	Top dead centre
TR	Trapping efficiency
TWh	Tera Watt hour
URANS	Unsteady Reynolds averaged Navier-Stokes
VEMOD	Virtual engine model
VGT	Variable geometry turbine
VGC	Variable geometry compressor
VGO	Variable geometry orifices
VIGV	Variable inlet guide vane
VNGV	Variable nozzle guide vane
VSV	Variable stator Vane
WCAC	Water charged air cooler
WLTP	Worldwide harmonized light-duty cycle

Chapter 1

Introduction

Contents

1.1 Background

Internal combustion engines (ICEs) have always been the major propulsion systems in the road transportation industry. However, new emissions laws are being defined every few years to reduce greenhouse gas emissions and their environmental impact. New norms call for the future development of existing technology by providing potential solutions for sustainable mobility. Nevertheless, specifically in Europe, the latest emission laws (Euro-7 in proposal stage) favor the rise of new technology for sustainable mobility, electric vehicles. Are these favorable norms the downfall of the ICEs? Is emerging technology the only viable solution? Does the electric grid system have enough resources to fully aid the functionality of electric cars? Are there any other potential solutions for road transportation? This introductory section discusses the potentialities and weak links for such futuristic road transportation in the above context. Along with presenting the motivation of this thesis work for further development of existing state-of-the-art road transportation for future mobility.

The recent policies and objectives for zero emissions in Europe are presented in Fit-for-55 package [4]. The norms from Fit-for-55 depict that, by 2030, a reduction of 55% in greenhouse gases must be achieved while comparing targets from 1990. Although these reforms are not only subjected to emissions from the automotive sector but also to construction, energy production, and any carbon border mechanisms. The norms are the consequences of air pollution and the health risks associated with such anomalies. Over the years, due to the implementation of several regulatory policies to control air pollution, a vast majority of the urban population is still exposed to concentrations above the limit defined by the ambient air quality directives [5]. It is estimated that about 300 000 premature death occurs due to air pollution [6]. Despite other sectors playing a vital role in air pollution, it is argued that road transport contributes to most of the air pollution. Studies state that, on average, 39% of NO_x emissions occur from road transportation, and numbers are even higher in urban areas estimating up to 47% [7]. Data related to CO_2 emissions show that the transportation industry is responsible for 11% of the total emissions related to CO_2 [8].

To abide by the Fit-for-55 norms, new legislative policies are reformed for the automotive industry in Euro-7 [9]. To decarbonize the existing technology for propulsion on land, the European Commission has proposed some policies

over the last couple of years. Firstly, on July 2020, to regulate CO_2 emissions, performance standards for cars and vans were established [10]. Furthermore, it ensured a clear pathway toward zero-emission mobility. On December 2020, the commission adopted strategies towards sustainable and smart mobility [11]. To accelerate the path towards decarbonization in May of 2021, the commission released action plans for zero emissions [12]. In ordains with the policies and strategies of the European Commission, road transportation should become less polluting, specifically in urban regions. To attain such high emission standards, Euro-7 norms are considered an essential part of the transition toward clean mobility.

From the above legislative policies, it is understood that ICE are being banned from the transportation industry. Aiming toward the current topic, it is presented with some weak links that can be attributed to future sustainable mobility. The so-called electric vehicle or Battery Electric Vehicles (BEVs) are presented. Primarily, it must be understood that electricity does not exist as a source; it must be generated and stored. The storage of high-quality energy requires the use of large power stations, and the energy must be used immediately; otherwise, it may result in significant losses. Different means of energy storage technologies are available, and these are as follows:

- Flywheel Storage [13]

- Battery Storage [14]

- Super-capacitor Storage [15]

- Hydrogen Storage [16]

- Pneumatic Storage [17]

    - Liquid Piston
    - Compressed air

- Pumped storage [18]

Using mechanical storage systems calls for issues related to packing factors, i.e., occupying more space. This is because bigger storage systems must be used to observe potential benefits. For instance, larger inertia means more energy can be stored in flywheel storage technologies. Also, mechanical systems

are highly unstable. Therefore, the systems must be tuned with at-most precision, such as pneumatic architecture, leading to issues related to the costs of making the technology. Limitations in usability can also be an issue, as vibrations may lead to a highly tuned system moving away from optimum working conditions. High-vibration noises can be seen in and around the vehicle. Finally, left with battery storage technology, which has its own set of im-maturities to deal with. Although this technology has proven that it occupies the space of an IC engine and can withstand vibrations usually seen around a vehicle, in itself, BEVs are quieter than ICE. But it must be understood that batteries have been known to mankind for several years, and still, in most battery technologies, energy storage happens chemically. And the necessary range of operation in providing power and energy is lower when compared with technologies such as ICEs. Also, this technology comes with some potholes, although not limited to but are as follows:

- Deterioration of the battery over long-term usage includes charging and discharging under high-power conditions. This high-power charging is necessary to save time and can lead to a thermal runaway in batteries [19]. Researchers are focusing on optimizing the battery life to increase durability, as depicted by Carter et al. [20], minimizing losses [21], and improving charging systems [22].

- Issues related to the production of high-density power to drive the power train for road transportation. Although extensive research is being conducted to address this issue [23].

- Due to prolonged usage of the battery and its deterioration, servicing and changing the battery is needed, which means that additional cost is incurred to maintain the BEVs, compared to ICEs [24].

- Nonetheless, raw materials are needed to manufacture the battery. For BEVs, lithium-ion batteries are used, including lithium and rare metals such as cobalt, magnesium, copper, and many other minerals. These metals need to mined under hazards, and dangerous conditions, which can be attributed to lack of safety during mining, abusing labor laws, and mining itself leading to additional greenhouse gas emissions. In any case, if the minerals are safely extracted, few countries, such as China, have the necessary refineries to build state-of-the-art batteries. Adding to the insecurities in supply from China due to its geopolitical stand, leading to an increase in the products price [25].

Secondly, the manner in which the electricity is produced must also be considered. Figure 1.1 shows the electricity production information for each source over the past 35 years [26]. To date, it can be observed that about 40% of the electric energy production comes from coal. And the share of non-renewable sources of energy production is more than 60%. For 2021, about 2700 TWh of energy is generated using nuclear energy, while almost double the energy is produced from hydropower generation. While merely 11% of the total energy produced comes from renewable energy sources. The energy production of renewable energy sources is low due to their unpredictable characteristic in the variability of power output [27].

Source: Our World in Data based on BP Statistical Review of World Energy (2022); Ember's Global and European Electricity Reviews (2022)
Note: 'Other renewables' includes waste, geothermal, wave and tidal.
OurWorldInData.org/energy • CC BY
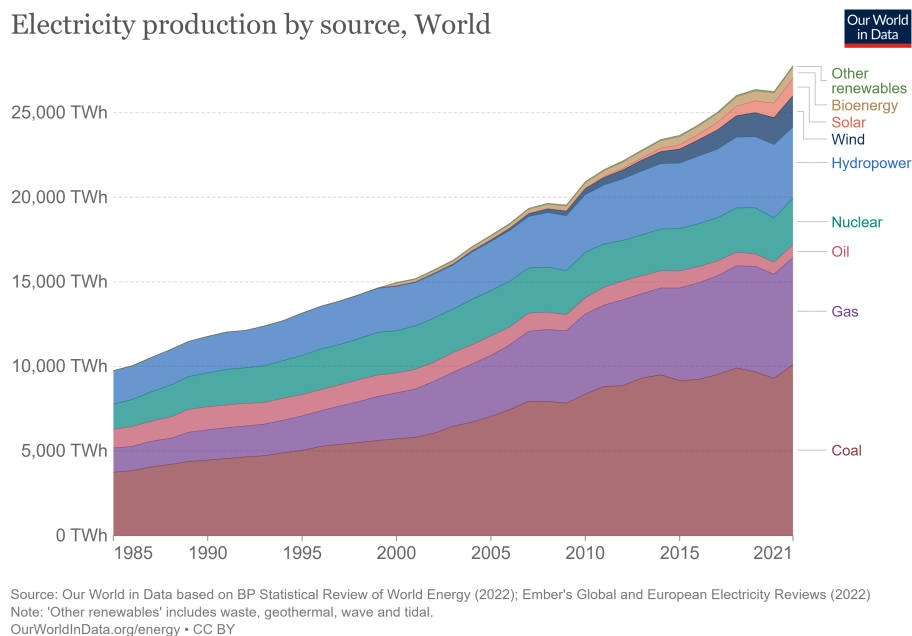
Figure 1.1: World energy production

Several countries, such as the USA, India, Germany, and Russia, rely on coal for their electricity production. While other nations such as China and Australia are moving towards hydropower regeneration to meet their specific power demands. In Europe, most Norwegian nations produce electricity from wind energy, and the produced energy is self-sufficient to their necessity. Some countries like France are committed to nuclear power generation despite the

catastrophes it may be led to, as seen in Japan and Chernobyl. Due to the different mix in power generation, BEVs are not the viable solution for zero emissions as the power generation and distribution system needs further development to overcome their power losses. Along with the decrease in the usage of fossil fuels for power generation as they produce most of the greenhouse gases.

Figure 1.2 depicts information related to sector-wise greenhouse gas emissions. Observing the trends from Figure 1.2 for the past ten years, it can be said that the electricity and heating industry produces most of the greenhouse gases, as they mostly rely on fossil fuels. Moreover, the transportation industry takes second place in its emissions due to the same issue of fossil fuel usage.
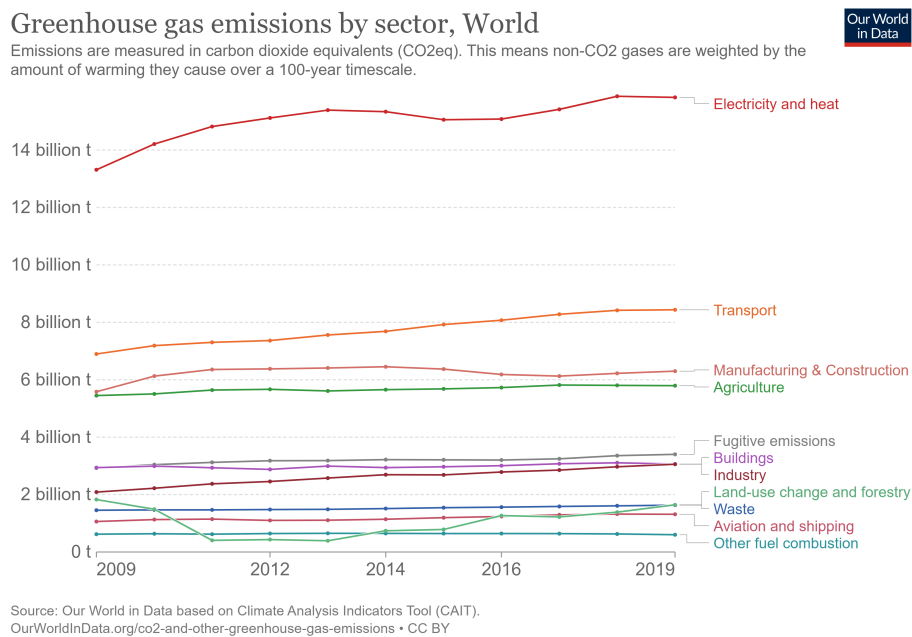

Figure 1.2: Sector wise contribution towards CO_2 emissions all over the world [28]

Observing trends in energy production from Figure 1.1 and greenhouse gas emissions from Figure 1.2, transitioning from pure ICE to BEVs leads to further greenhouse gases, which is not a reliable solution. A plethora of

studies supporting the above statement is available in the literature. According to Verma et al. [29], who conducted Life Cycle Analysis (LCA) and Life Cycle Cost (LCC) on an electric vehicle and ICE concluded that BEVs have a more toxicity impact on humans due to constant exposure to heavy metals, chemicals, and high voltage batteries. Adding on to the higher initial cost at the time of purchase as batteries are more expensive. According to LCA conducted by Kawamoto et al.[30] for estimating CO_2 emissions over the entire life cycle of BEVs and ICEs show that BEVs produce more CO_2 considering their build and maintenance. Moreover, adding the battery disposal problems would further increase the emission.

The following conclusions can be drawn from the above-depicted information:

- Eliminating fossil fuel usage for electricity production and focusing on other energy production sources, such as renewable sources, must be developed. This includes further research and development of the infrastructure and control of constant power generation from such systems.

- Minimizing power losses in electricity distribution and charging stations.

- Improvements in battery manufacturing, management for optimum performance, maintenance, and services. Nevertheless, battery disposal and reuse are also important.

- Focusing on current ICEs for improvements in the reduction of emissions. Moreover, these ICEs can be further downsized and used as range extenders for Hybrid Electric Vehicles (HEVs).

Using ICEs as range extenders, the load for electricity production through renewable energy sources can be reduced. Giving adequate time for researchers and investors to research and develop the infrastructure for BEVs can be accomplished. This is because the BEVs is a young technology that has been in the limelight for the past 10 years and needs improvements over the well-established ICEs which has over 110 years of research and development.

1.2 Motivation

As per the Global Warming Potential (GWP) index, road transportation contributes to 11.9% of the total greenhouse gas emission [28]. While from the same, it can be observed that 45% of greenhouse gases are emitted through energy production using fossil fuels. Replacing ICEs with BEVs means relying more on energy production where non-renewable sources of energy are used, leading to increased emissions as net-zero emission sources of energy production contribute to only 15% of the overall energy production.

As the years progress, new emissions standards and regulations are added to existing testing criteria. Firstly, it is important to understand how the emissions standards have been classified and implemented over the years. Majorly in Europe, three driving cycles are used: the New European Driving Cycle (NEDC)[31], the Worldwide Harmonized Light-duty cycle (WLTC)[32], and Real Driving Emissions (RDE)[33]. Each testing standard has its own norms to be met for qualification. RDE is considered the most realistic cycle test, considering a wide range of engine loads, vehicle speeds, ambient temperature, and boost pressure. RDE cycle specifications are differentiated into three domains: Urban, Rural, and Motorways. Also, the norms differ for Light-duty vehicles (LDV) and heavy-duty vehicles (HDV).

The information depicted in Table 1.1 and Table 1.2 are the new testing standards incorporated in Euro-7 emissions norms over the existing standards of Euro-6D for LDV and HDV, respectively. The new norms show that tailpipe emissions have become more stringent by adding restrictions for new gas emissions, which were not accounted for in previous emission standards of the RDE cycle. To achieve the new regulation standards, several researchers are focusing on using new fuel types such as Hydrogen, Ammonia, and additives to diesel to reduce emissions.

Table 1.1: Real Driving Emission standards for LDV

RDE Regulation	Euro-7	Euro-6D
Ambient Temperature	$-10°C$ to $45°C$	$-7°C$ to $35°C$
Maximum Altitude	1800 m	1400 m
Pollutants	Euro 6D + PM_{10}, CH_4, NH_3	$CO_2, HC, CO, NO_x, PM_{25}$

Table 1.2: Real Driving Emission standards for HDV

RDE Regulation	Euro-7	Euro-6D
Pollutants	Euro 6D + $PM_{10}, CH_4, NH_3, N_2O, HCHO$	$CO_2, HC, CO, NO_x, PM_{25}$
Payload	< 10% extended	Not existed

Studies can be found focusing on the usage of ammonia (NH_3) and hydrogen as their working fluid in both Spark Ignition (SI) and Compression Ignition (CI) settings. Dinesh et al.[34] showed NH_3 could lead to higher Compression Ratios (CR) in SI engines without knocking. Along with providing concrete evidence that no greenhouse gas emissions at lower CR are seen. Results depicting a reduction in peak heat release rate (HRR) after adding NH_3 can be seen in [35]. This reduction in HRR is due to prolonged flame development and increased flame propagation duration. Usage of NH_3 in marine engines has shown to attain similar engine load range and thermal efficiency along with negligible amounts of NO_x and CO_2 emissions [36], and the same has been confirmed for a dual fuel CI engine by Kurien et al.[37]. The advantages and disadvantages of using ammonia as engine fuel and its future pathway are summarized in [38]. Due to the lack of carbon-free atoms, hydrogen as fuel in SI engine has shown promising results in attaining higher engine power output, efficiency, and low emissions [39]. A detailed review of the usage of hydrogen in SI, CI, and LPG engines is studied, and several parameters influencing its low-emission performance are presented in [40] and [41]. A study on hydrogen production, storage, and role in futuristic combustion engines is depicted in [42].

Several research groups have focused on synthetic fuels such as OEM_x[43], hydro-treated vegetable oil[44], biomass[45], and Polyoxymethylene Dimethyl Ether ($PODE_3$)[46] depicting their advantages in low emissions can be seen. These surrogate fuels provided benefits due to their chemical properties which had higher molecular weight. Due to this reason, benefits in prolonged flame development, combustion duration, and lower HRR are achieved, drastically reducing pollutant formation. The development in such surrogate fuels can also be found in [47].

Although the above-depicted information is related to fuel, combustion, and HRR, these techniques have proved to reduce pollutant formation and, thereby, emissions. From the air management point of view, downsizing of engines along with turbocharging [2], oxyfuel combustion using Mixed Ionic-

9

electronic Conducting membrane (MIEC) [48], Exhaust Gas Recirculation (EGR) techniques [1], prototype testing of advanced two-stroke engines, and many other downsizing techniques can be seen. Nonetheless, these advanced two-stroke powertrains can be used as range extenders for hybrid powertrains or produce the necessary electricity to charge a battery. By doing so, the range and self-sustainability of HEVs can be improved. Due to its compactness and fewer moving parts in such downsized engines, losses in terms of frictional and mechanical are minimized. Due to a small range of operating conditions, such ICE emissions can also be reduced.

1.3   Objectives

The main objectives of the this thesis work are :

- To develop the novel engine in a 1D mode. To achieve this particular objective VEMOD software has been used. The model uses geometrical data for its model development and is validated against experimental data.

- Understand the in-cylinder thermo-fluid dynamic. The 1D model results for the temperature and trapped mass inside the cylinder during scavenging process were compared with CFD simulation data. Deviations in the 1D model predictability using state-of-the-art heat transfer model were observed, leading to the proposal of a new heat transfer model during scavenging. The new heat transfer model developed in this thesis work is referred as proposed heat transfer model.

- To assess the gas dynamics inside the cylinder with change in engine speed, load conditions and exhaust layout, in order to evaluate the differences in scavenge related parameters.

This work studies an advanced two-stroke engine for its novel engine design over its operating range and thermofluid-dynamic assessment. For this purpose, an experimental campaign has been developed, and necessary information on the engine performance has been captured. Taking advantage of the experimental data, a 1D gas dynamic model has been validated for fluid dynamic performance. This is established to overcome any experimental uncertainties that may influence the engine performance and for future prospective

analysis. Once coherence in results was obtained, 1D results were used as initial and boundary conditions for CFD simulations to assess heat transfer and scavenging phenomenons. On observing the results, it was found that the existing state-of-the-art heat transfer model fails to predict the temperature during scavenging, leading to a new heat transfer model proposal. The procedure followed in this thesis work is as follows:

- Chapter 2 provides a detailed literature review on state-of-the-art technologies related to advanced two-stroke engines for sustainable mobility.

- Chapter 3 describes the experimental and modeling tools used in this thesis work. A detailed description of the 1D model, 3D CFD model, and engine tests are provided. Engine simulations from 1D are used to analyze fluid dynamic properties and provide IC for CFD, while experimental results are used for validating and calibrating the model. Furthermore, CFD simulations are used to analyze thermal effects.

- Chapter 4 includes information on the literature review for the heat transfer model and scavenging processes. It also provides details of the state-of-the-art heat transfer model used to study the novel engine and the proposed heat transfer and scavenging model description.

- Chapter 5 presents the results of virtual model validation using experimental data, proposed heat transfer model calibration using CFD simulation results, and potential observations on the engine performance using the proposed heat transfer model. Moreover, using the proposed scavenging model, the results of the short-circuit of air are depicted. Information from CFD is used to validate the proposed scavenging model in chapter 5.

- Chapter 6 provides the main conclusion and potential future studies derived from the research carried out in the current thesis.

Chapter 1 references

[1]   J. R. Serrano, H. Climent, P. Piqueras, and A. Darbhamalla. "Energy recovery potential by replacing the exhaust gases recirculation valve

with an additional turbocharger in a heavy-duty engine". *Energy Conversion and Management* 271 (Nov. 2022), p. 116307. ISSN: 01968904. DOI: 10.1016/j.enconman.2022.116307 (cit. on pp. xvii, 10).

[2] J. R. Serrano, H. Climent, A. Gomez-Vilanova, A. Darbhamalla, and S. Guilain. "Assessment of Variable Geometry Orifice Compressor Technology Impact in a New Generation of Compression Ignition Powertrains at Low-End and Transient Operation". *Applied Sciences* 12 (24 Dec. 2022), p. 12869. ISSN: 2076-3417. DOI: 10.3390/app122412869 (cit. on pp. xvii, 9).

[4] S. Schlacke, H. Wentzien, E.-M. Thierjung, and M. Köster. "Implementing the EU Climate Law via the 'Fit for 55' package". *Oxford Open Energy* 1 (Jan. 2022). ISSN: 2752-5082. DOI: 10.1093/ooenergy/oiab002 (cit. on p. 2).

[5] M. Langkamp and V. Bayma. "Evaluation of the Directive 2008/50/EC on Ambient Air Quality". *Science for Sustainability Journal* 3 (Jan. 2019). DOI: 10.53466/VERI6053.S4SLAB (cit. on p. 2).

[6] M. Iriti, P. Piscitelli, E. Missoni, and A. Miani. *Air pollution and health: the need for a medical reading of environmental monitoring data.* 2020 (cit. on p. 2).

[7] D. Bart, P. Enrico, P. Emanuela, D. M. Alexander, M.-F. Fabio, B. Katalin, M. Alessandro, A.-L. Maria, T. Philippe, and V. Elisabetta. "Urban NO2 Atlas" (2019) (cit. on p. 2).

[8] Z. Zhongming, L. Linong, Y. Xiaona, L. Wei, et al. "Emissions of most harmful air pollutants dropped in 2018, marking EU progress under UN Convention" (2020) (cit. on p. 2).

[9] J. Cross and J. Bølstad. "Openness and censorship in the European Union: An interrupted time series analysis". *European Union Politics* 16 (May 2014), pp. 216–240. DOI: 10.1177/1465116514560066 (cit. on p. 2).

[10] R. Čižinská and J. Chládková. "Selected Impacts of Regulation (EU) 2019/631 On Value Creation in the Automative Industry". *Financial Internet Quarterly* 17 (Sept. 2021), pp. 76–87. DOI: 10.2478/fiqf-2021-0022 (cit. on p. 3).

[11] K. Gkoumas, F. Marques dos Santos, M. Stępniak, and F. Pekár. "Research and Innovation Supporting the European Sustainable and Smart Mobility Strategy: A Technology Perspective from Recent European Union Projects". *Applied Sciences* 11 (Dec. 2021), p. 11981. DOI: 10.3390/app112411981 (cit. on p. 3).

[12] N. Sadeleer. "Environmental Law in the EU: A Pathway Toward the Green Transition". In: Mar. 2023, pp. 21–33. ISBN: 978-3-031-24887-0. DOI: 10.1007/978-3-031-24888-7_2 (cit. on p. 3).

[13] M. Amiryar and K. Pullen. "A Review of Flywheel Energy Storage System Technologies and Their Applications". *Applied Sciences* 7 (3 Mar. 2017), p. 286. ISSN: 2076-3417. DOI: 10.3390/app7030286 (cit. on p. 3).

[14] S. Y. Khan. "A comparative study and analysis of PHES and UGPHES systems." PhD thesis. 2015 (cit. on p. 3).

[15] A. Allagui, A. S. Elwakil, M. E. Fouda, and A. G. Radwan. "Capacitive behavior and stored energy in supercapacitors at power line frequencies". *Journal of Power Sources* 390 (June 2018), pp. 142–147. ISSN: 03787753. DOI: 10.1016/j.jpowsour.2018.04.035 (cit. on p. 3).

[16] F. Zhang, P. Zhao, M. Niu, and J. Maddy. "The survey of key technologies in hydrogen energy storage". *International Journal of Hydrogen Energy* 41 (33 Sept. 2016), pp. 14535–14552. ISSN: 03603199. DOI: 10.1016/j.ijhydene.2016.05.293 (cit. on p. 3).

[17] C. Wang, F. Wang, C. Li, W. Chen, H. Wang, and L. Lu. "Investigation on energy conversion instability of pump mode in hydro-pneumatic energy storage system". *Journal of Energy Storage* 53 (Sept. 2022), p. 105079. ISSN: 2352152X. DOI: 10.1016/j.est.2022.105079 (cit. on p. 3).

[18] S. Rehman, L. M. Al-Hadhrami, and M. M. Alam. "Pumped hydro energy storage system: A technological review". *Renewable and Sustainable Energy Reviews* 44 (Apr. 2015), pp. 586–598. ISSN: 13640321. DOI: 10.1016/j.rser.2014.12.040 (cit. on p. 3).

[19] J. Du, Y. Liu, X. Mo, Y. Li, J. Li, X. Wu, and M. Ouyang. "Impact of high-power charging on the durability and safety of lithium batteries used in long-range battery electric vehicles". *Applied Energy* 255 (Dec. 2019), p. 113793. ISSN: 03062619. DOI: 10.1016/j.apenergy.2019.113793 (cit. on p. 4).

[20] R. Carter, A. Cruden, and P. J. Hall. "Optimizing for Efficiency or Battery Life in a Battery/Supercapacitor Electric Vehicle". *IEEE Transactions on Vehicular Technology* 61 (4 May 2012), pp. 1526–1533. ISSN: 0018-9545. DOI: 10.1109/TVT.2012.2188551 (cit. on p. 4).

[21] M. Amiri, M. Esfahanian, M. R. Hairi-Yazdi, and V. Esfahanian. "Minimization of power losses in hybrid electric vehicles in view of the prolonging of battery life". *Journal of Power Sources* 190 (2 May 2009), pp. 372–379. ISSN: 03787753. DOI: 10.1016/j.jpowsour.2009.01.072 (cit. on p. 4).

[22] A. A. A. Al-karakchi, G. Lacey, and G. Putrus. "A method of electric vehicle charging to improve battery life". In: IEEE, Sept. 2015, pp. 1–3. ISBN: 978-1-4673-9682-0. DOI: 10.1109/UPEC.2015.7339846 (cit. on p. 4).

[23] M. A. Rahman, X. Wang, and C. Wen. "A review of high energy density lithium–air battery technology". *Journal of Applied Electrochemistry* 44 (1 Jan. 2014), pp. 5–22. ISSN: 0021-891X. DOI: 10.1007/s10800-013-0620-8 (cit. on p. 4).

[24] H. Farzin, M. Fotuhi-Firuzabad, and M. Moeini-Aghtaie. "A Practical Scheme to Involve Degradation Cost of Lithium-Ion Batteries in Vehicle-to-Grid Applications". *IEEE Transactions on Sustainable Energy* 7 (4 Oct. 2016), pp. 1730–1738. ISSN: 1949-3029. DOI: 10.1109/TSTE.2016.2558500 (cit. on p. 4).

[25] B. Jones, R. J. Elliott, and V. Nguyen-Tien. "The EV revolution: The road ahead for critical raw materials demand". *Applied Energy* 280 (Dec. 2020), p. 115072. ISSN: 03062619. DOI: 10.1016/j.apenergy.2020.115072 (cit. on p. 4).

[26] H. Ritchie, M. Roser, and P. Rosado. "Energy". *Our World in Data* (2022). https://ourworldindata.org/energy (cit. on p. 5).

[27] D. Akinyele and R. Rayudu. "Review of energy storage technologies for sustainable power networks". *Sustainable Energy Technologies and Assessments* 8 (Dec. 2014), pp. 74–91. ISSN: 22131388. DOI: 10.1016/j.seta.2014.07.004 (cit. on p. 5).

[28] H. Ritchie, M. Roser, and P. Rosado. "CO and Greenhouse Gas Emissions". *Our World in Data* (2020). https://ourworldindata.org/co2-and-greenhouse-gas-emissions (cit. on pp. 6, 8).

[29] S. Verma, G. Dwivedi, and P. Verma. "Life cycle assessment of electric vehicles in comparison to combustion engine vehicles: A review". *Materials Today: Proceedings* 49 (2022), pp. 217–222. ISSN: 22147853. DOI: 10.1016/j.matpr.2021.01.666 (cit. on p. 7).

[30] R. Kawamoto, H. Mochizuki, Y. Moriguchi, T. Nakano, M. Motohashi, Y. Sakai, and A. Inaba. "Estimation of CO2 Emissions of Internal Combustion Engine Vehicle and Battery Electric Vehicle Using LCA". *Sustainability* 11 (9 May 2019), p. 2690. ISSN: 2071-1050. DOI: 10.3390/su11092690 (cit. on p. 7).

[31] E. Directive. *90/C81/01,"Emission Test Cycles for the Certification of light duty vehicles in Europe", EEC Emission Cycles, 1999* (cit. on p. 8).

[32] M. Tutuianu, P. Bonnel, B. Ciuffo, T. Haniu, N. Ichikawa, A. Marotta, J. Pavlovic, and H. Steven. "Development of the World-wide harmonized Light duty Test Cycle (WLTC) and a possible pathway for its introduction in the European legislation". *Transportation Research Part D: Transport and Environment* 40 (Oct. 2015), pp. 61–75. ISSN: 13619209. DOI: 10.1016/j.trd.2015.07.011 (cit. on p. 8).

[33] J. Merkisz and J. Pielecha. "Selected remarks about RDE test". *Combustion Engines* 166 (3 Aug. 2016), pp. 54–61. ISSN: 2300-9896. DOI: 10.19206/CE-2016-340 (cit. on p. 8).

[34] M. Dinesh, J. K. Pandey, and G. Kumar. "Study of performance, combustion, and NOx emission behavior of an SI engine fuelled with ammonia/hydrogen blends at various compression ratio". *International Journal of Hydrogen Energy* 47 (60 July 2022), pp. 25391–25403. ISSN: 03603199. DOI: 10.1016/j.ijhydene.2022.05.287 (cit. on p. 9).

[35] G. Xin, C. Ji, S. Wang, H. Meng, K. Chang, and J. Yang. "Effect of ammonia addition on combustion and emission characteristics of hydrogen-fueled engine under lean-burn condition". *International Journal of Hydrogen Energy* 47 (16 Feb. 2022), pp. 9762–9774. ISSN: 03603199. DOI: 10.1016/j.ijhydene.2022.01.027 (cit. on p. 9).

[36] L. Liu, Y. Wu, and Y. Wang. "Numerical investigation on the combustion and emission characteristics of ammonia in a low-speed two-stroke marine engine". *Fuel* 314 (Apr. 2022), p. 122727. ISSN: 00162361. DOI: 10.1016/j.fuel.2021.122727 (cit. on p. 9).

[37] C. Kurien and M. Mittal. "Review on the production and utilization of green ammonia as an alternate fuel in dual-fuel compression ignition engines". *Energy Conversion and Management* 251 (Jan. 2022), p. 114990. ISSN: 01968904. DOI: 10.1016/j.enconman.2021.114990 (cit. on p. 9).

[38] D. Han, Y. Liu, and Z. Huang. *The Use of Ammonia as a Fuel for Combustion Engines.* 2022. DOI: 10.1007/978-981-16-8717-4_16 (cit. on p. 9).

[39] H. L. Yip, A. Srna, A. C. Y. Yuen, S. Kook, R. A. Taylor, G. H. Yeoh, P. R. Medwell, and Q. N. Chan. "A Review of Hydrogen Direct Injection for Internal Combustion Engines: Towards Carbon-Free Combustion". *Applied Sciences* 9 (22 Nov. 2019), p. 4842. ISSN: 2076-3417. DOI: 10.3390/app9224842 (cit. on p. 9).

[40] D. Akal, S. Öztuna, and M. K. Büyükakın. "A review of hydrogen usage in internal combustion engines (gasoline-Lpg-diesel) from combustion performance aspect". *International Journal of Hydrogen Energy* 45 (60 Dec. 2020), pp. 35257–35268. ISSN: 03603199. DOI: 10.1016/j.ijhydene.2020.02.001 (cit. on p. 9).

[41] B. Shadidi, G. Najafi, and T. Yusaf. "A Review of Hydrogen as a Fuel in Internal Combustion Engines". *Energies* 14 (19 Sept. 2021), p. 6209. ISSN: 1996-1073. DOI: 10.3390/en14196209 (cit. on p. 9).

[42] A Onorati et al. "The role of hydrogen for future internal combustion engines". *International Journal of Engine Research* 23 (4 Apr. 2022), pp. 529–540. ISSN: 1468-0874. DOI: 10.1177/14680874221081947 (cit. on p. 9).

[43] A. Omari, B. Heuser, and S. Pischinger. "Potential of oxymethylenether-diesel blends for ultra-low emission engines". *Fuel* 209 (Dec. 2017), pp. 232–237. ISSN: 00162361. DOI: 10.1016/j.fuel.2017.07.107 (cit. on p. 9).

[44] J. V. Pastor, J. M. García-Oliver, C. Micó, A. A. García-Carrero, and A. Gómez. "Experimental Study of the Effect of Hydrotreated Vegetable Oil and Oxymethylene Ethers on Main Spray and Combustion Characteristics under Engine Combustion Network Spray A Conditions". *Applied Sciences* 10 (16 Aug. 2020), p. 5460. ISSN: 2076-3417. DOI: 10.3390/app10165460 (cit. on p. 9).

[45] H. L. Chum and R. P. Overend. "Biomass and renewable fuels". *Fuel Processing Technology* 71 (1-3 June 2001), pp. 187–195. ISSN: 03783820. DOI: 10.1016/S0378-3820(01)00146-1 (cit. on p. 9).

[46] T. He, Z. Wang, X. You, H. Liu, Y. Wang, X. Li, and X. He. "A chemical kinetic mechanism for the low- and intermediate-temperature combustion of Polyoxymethylene Dimethyl Ether 3 (PODE3)". *Fuel* 212 (Jan. 2018), pp. 223–235. ISSN: 00162361. DOI: 10.1016/j.fuel.2017.09.080 (cit. on p. 9).

[47] W. J. Pitz and C. J. Mueller. "Recent progress in the development of diesel surrogate fuels". *Progress in Energy and Combustion Science* 37 (3 June 2011), pp. 330–350. ISSN: 03601285. DOI: 10.1016/j.pecs.2010.06.004 (cit. on p. 9).

[48] J. Serrano, F. Arnau, L. García-Cuevas, and V. Farias. "Oxy-fuel combustion feasibility of compression ignition engines using oxygen separation membranes for enabling carbon dioxide capture". *Energy Conversion and Management* 247 (Nov. 2021), p. 114732. ISSN: 01968904. DOI: 10.1016/j.enconman.2021.114732 (cit. on p. 10).

Chapter 2

State of the art

Contents

2.1 Introduction

This chapter reviews small-capacity engines for their potentiality in moving toward sustainable mobility. In the above context state-of-the-art two-stroke uniflow scavenged engines are presented.

2.2 Two stroke technology

The term "two-stroke" refers to a type of ICE that finishes the power cycle in just two strokes of the piston, as shown in Figure 2.1. This power cycle is completed in one crankshaft revolution, whereas in a four-stroke ICE, it is completed in two crankshaft revolutions. In a two-stroke engine, the end of the combustion stroke and the start of the compression stroke occur simultaneously, and both intake and exhaust ports open simultaneously in a process called scavenging.
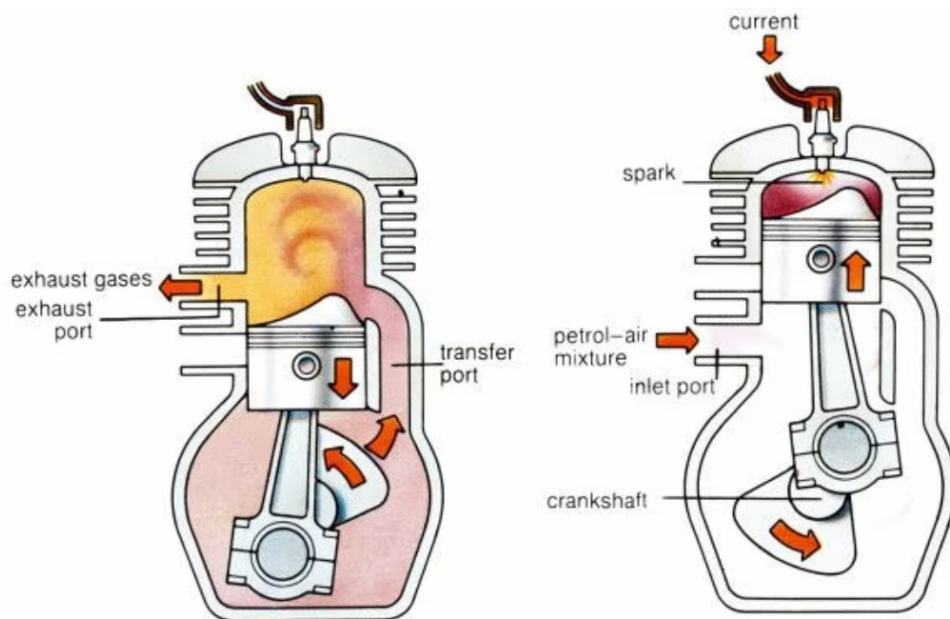

Figure 2.1: Conventional two-stroke engine design and functionality
[49]

Although the main principle of the working of the two-stroke ICE remains the same, the mechanical details vary for each type. These design types are differentiated based on their methods of taking the intake charge, scavenging process, and exhausting the cylinder.

- Piston-controlled inlet port [50]

- Reed inlet valve [51]

- steeped piston engine [52]

- cross-flow scavenging [53]

- Loop scavenging [54]

- Uniflow scavenging

2.2.1 Uniflow scavenging engines

Uniflow scavenging engines are being studied for their potential to lower emissions for sustainable mobility. Due to their design and operating range, these engines can be compact, be heavily downsized, and have fewer emissions. Different uniflow scavenging prototype engines are studied for their performance. These technologies are as follows but are not limited to:

2.2.1.1 Two-stroke rod-less piston engines

Also known as the Free-Piston Engine (FPE), it is a prime example of a two-stroke rod-less piston engine. "Free piston" refers to an engine that operates without a traditional crankshaft and instead has a piston that is free to move back and forth within the cylinder. The piston motion is a resultant force acting on the piston, which is exerted due to combustion pressure on one side and the other due to the rebound device. Some of the advantages of FPE are:

- As there are fewer moving parts in FPE, it results in a lower frictional loss. Also, for the same reason, the FPEs can achieve a higher power-to-weight ratio than conventional engines.

- The piston motion relies on the forces from the combustion process and rebound load, resulting in the possibility of a variable compression ratio.

- Due to the variable compression ratio, using different fuels and combustion regimes is also possible.

The main components of the FPE are a combustion chamber, a loading device, and a rebound device. Usually, the load device of FPE is a linear alternator, which converts the kinetic energy into electrical energy. The linear alternator can also be used as a linear motor to start the engine. The rebound device is used to counteract the combustion forces and provide the necessary force to return the piston from the bottom dead center (BDC) to the top dead center (TDC). Based on the number of pistons and the direction of motion, these engines are classified as single-piston FPE, opposed-piston FPE, and dual-piston FPE.

- Single-piston FPE: An example of the single piston is depicted in Figure 2.2. In this specific FPE, an air spring chamber is used as a rebound device to revert the piston at BDC. The potentiality of such FPEs is the accuracy by which the piston and operating frequency can be controlled. However, because of the imbalances in the alternator assembly, high noise and vibration levels can be seen in this FPE. Furthermore, these types of engines have only one combustion event per cycle, resulting in lower power density than dual-piston FPEs [55].
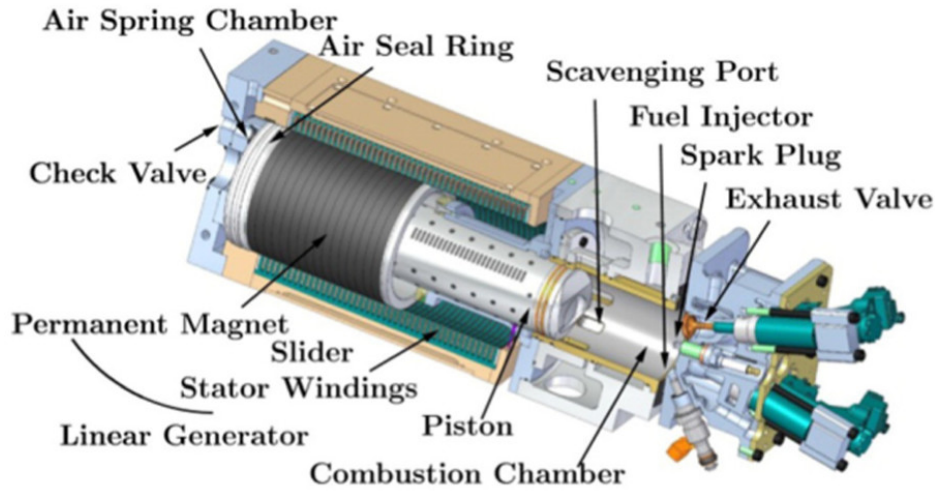
Figure 2.2: Single piston FPE
[55]

- Opposed-piston FPE: Consists of two pistons sharing a common combustion chamber. Due to the lack of a piston head, the heat transfer losses in such FPE are minimal. Due to its significant design, the engine provides vibration-free operation. However, the motion of the pistons must be synchronized, which needs additional mechanical links or high-speed piston motion control. This either increases the weight and frictional loss or the cost of the build. One such engine is studied by Serrano et al. [56], where the pistons in this engine are controlled by a rotary mechanism that uses a crankshaft with cams facing perpendicular to the skirts of the opposed pistons. Figure 2.3 depicts the engine and the working mechanism of opposed-piston FPE.
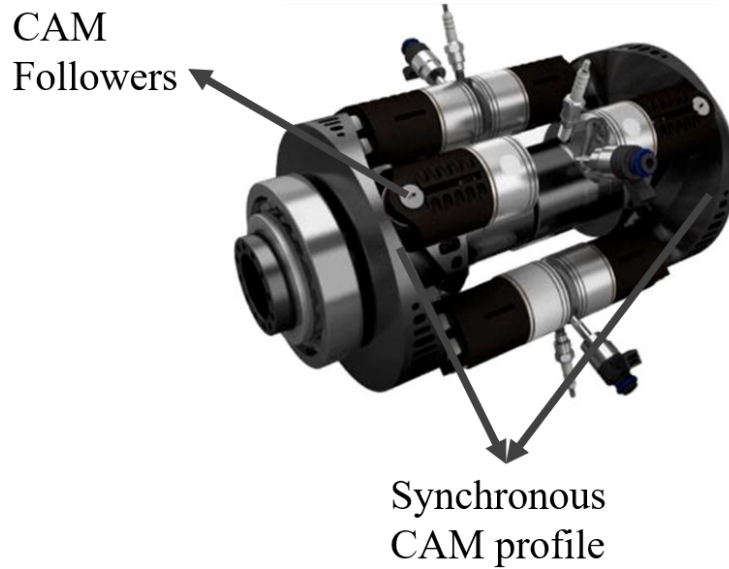
Figure 2.3: 2-Stroke rod-less opposed piston engine
[56]

- Dual-piston FPE: dual-piston FPE is an extended version of single-piston FPE with two crowns oscillating between two opposite combustion chambers [57]. Each combustion chamber acts as a rebound device for the opposite cylinder in which the expansion stroke in one cylinder provides the energy for the compression stroke of the opposite cylinder as shown in Figure 2.4. The advantage of the dual-piston FPE is the high power density, as there are two power strokes in a cycle. However, because of the inter-dependency between the combustion chambers, piston motion is more sensitive to combustion cyclic variations, which may lead to misfires and significant loss in power density. This phenomenon makes engine control more challenging.
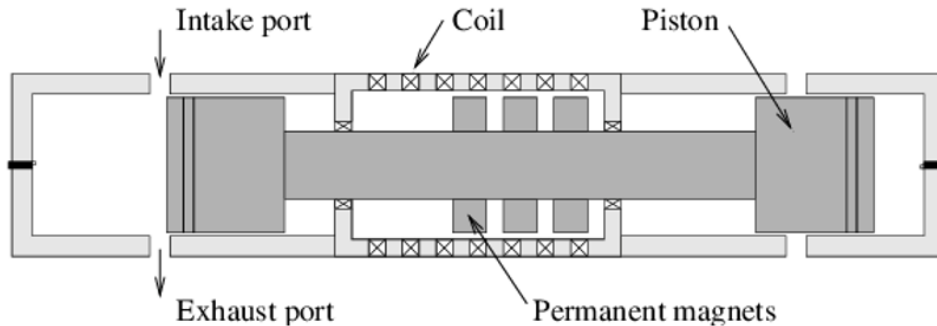
Figure 2.4: Illustration of a dual-piston FPE
[57]

Despite the challenges depicted for each FPE configuration, additional challenges associated with FPE are:

- Lack of a crankshaft and dependency on force balance for piston control, a high-speed controller is needed. Moreover, the lack of reliable control strategies for transient operation is a major limitation on the wide usage of FPE.

- Most FPEs are restricted to two-stroke operation because of the explicit necessity of one combustion event per cycle.

- Two-stroke engines come with their own challenges associated with the gas exchange process, where a portion of fresh air escapes with the exhaust gases. This exchange process is known as short-circuiting and impacts engine performance.

- Two-stroke engines have a lower effective compression ratio than their geometric compression ratio leading to reduced thermal efficiency compared to four-stroke engines.

- The unrestricted piston motion can lead to metal contact between the piston and the head causing significant structural damage.

To overcome the above challenges and fully control the piston position/motion, opposed piston architectures with crankshafts are proposed.

2.2.1.2 Two-stroke cranked piston engines

The piston motion is not free in these engine types, and the crankshaft controls the piston motion. Due to the addition of the crankshaft, it may be considered a conventional two-stroke engine. However, due to the number of pistons, scavenging process, and engine design, these engines are classified as:

- Single piston cranked engines: This thesis focuses on analyzing the thermo-fluid dynamic stability and performance of the aforementioned engine type. chapter 3 of this thesis provides a comprehensive overview of the engine design, experimental campaign, data captured, and modeling in both 1D and 3D CFD.

- Opposed-piston cranked engines: The gas path mechanism of this engine is very similar to that of opposed piston FPE. However, the piston motion is controlled using a crankshaft as depicted in Figure 2.5. This means that there is a margin possibility for the variable compression ratio. A detailed description of the development, working mechanism, and advantages of this engine is depicted by Regner et al. in [58].
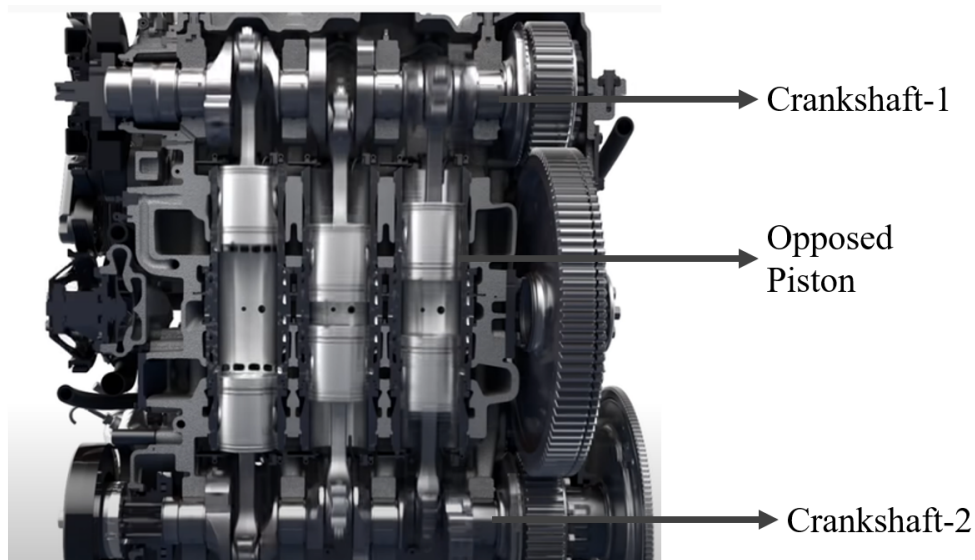

Figure 2.5: Opposed-piston cranked engine
[58]

Chapter 2 references

[49] K. Cameron. *Two-Stroke Engines: Defining Their Purpose.* Apr. 2015. URL: https://www.cycleworld.com/2015/04/06/two-stroke-motorcycle-engines-explained-tech-talk-by-kevin-cameron/ (cit. on p. 20).

[50] W. A. Woods and A. Allison. "Effective Flow Area of Piston Controlled Exhaust and Inlet Ports". In: Feb. 1977. DOI: 10.4271/770411 (cit. on p. 21).

[51] A. Dave, A. Siddiqui, D. Probst, and G. J. Hampson. "Development of a Reed Valve Model for Engine Simulations for Two-Stroke Engines". In: Mar. 2004. DOI: 10.4271/2004-01-1455 (cit. on p. 21).

[52] P. R. Hooper, T. Al-Shemmeri, and M. J. Goodwin. "An experimental and analytical investigation of a multi-fuel stepped piston engine". *Applied Thermal Engineering* 48 (Dec. 2012), pp. 32–40. ISSN: 13594311. DOI: 10.1016/j.applthermaleng.2012.04.034 (cit. on p. 21).

[53] D. L. Endicott and W. J. Tervo. "Combustion Chamber Design for Two-Stroke Cross-Flow Outboard Engines". In: Jan. 1962. DOI: 10.4271/620170 (cit. on p. 21).

[54] Z. Xu, F. Ji, S. Ding, Y. Zhao, Y. Wang, Q. Zhang, F. Du, and Y. Zhou. "Simulation and experimental investigation of swirl-loop scavenging in two-stroke diesel engine with two poppet valves". *International Journal of Engine Research* 22 (6 June 2021), pp. 2021–2034. ISSN: 1468-0874. DOI: 10.1177/1468087420916083 (cit. on p. 21).

[55] Y. Zhou, A. Sofianopoulos, B. Lawler, and S. Mamalis. "Advanced combustion free-piston engines: A comprehensive review". *International Journal of Engine Research* 21.(7) (2020), pp. 1205–1230. DOI: 10.1177/1468087418800612 (cit. on pp. 22, 23).

[56] J. Serrano, F. Arnau, P. Bares, A. Gomez-Vilanova, J. Garrido-Requena, M. Luna-Blanca, and F. Contreras-Anguita. "Analysis of a novel concept of 2-stroke rod-less opposed pistons engine (2S-ROPE): Testing, modelling, and forward potential". *Applied Energy* 282 (Jan. 2021), p. 116135. ISSN: 03062619. DOI: 10.1016/j.apenergy.2020.116135 (cit. on pp. 23, 24).

[57] R. Mikalsen and A. Roskilly. "A review of free-piston engine history and applications". *Applied Thermal Engineering* 27 (14-15 Oct. 2007), pp. 2339–2352. ISSN: 13594311. DOI: 10.1016/j.applthermaleng. 2007.03.015 (cit. on pp. 24, 25).

[58] G. Regner, D. Johnson, J. Koszewnik, E. Dion, F. Redon, and L. Fromm. "Modernizing the Opposed Piston, Two Stroke Engine for Clean, Efficient Transportation". In: Jan. 2013. DOI: 10.4271/2013-26-0114 (cit. on p. 26).

Chapter 3

Experimental and theoretical tools

Contents

3.1 Introduction

The primary tools utilized in this thesis are the 1D engine model, 3D CFD simulations, and the engine test bench. The 1D model is employed to analyze fluid dynamics phenomena in the combustion chamber, pipes, and volumes. Experimental results are then used to validate and calibrate the 1D model, enabling evaluation of the engine performance. Once fluid dynamic phenomena are captured, the findings from the 1D simulations served as initial conditions for CFD simulations to obtain temperature profiles. Further details on the utilization of these tools will be provided in chapter 4 and chapter 5, as applicable.

Therefore, this chapter is structured as follows: chapter 3 presents the working principle of the engine in Section 3.2, details of the experimental setup in Section 3.3, section 3.4 covers the development of the 1D model and section 3.5 provides information related to CFD modeling.

3.2 Engine description

This thesis utilizes a single-piston cranked engine, specifically a 2-stroke single-cylinder gasoline direct injection (GDI) engine. Figure 3.1 illustrates the engines schematic layout and working principle. The main engine attributes are provided in Table 3.1. A mechanical compressor mechanism is employed to achieve the needed pressure to promote the scavenging process, depicted as an air pump in Figure 3.1.
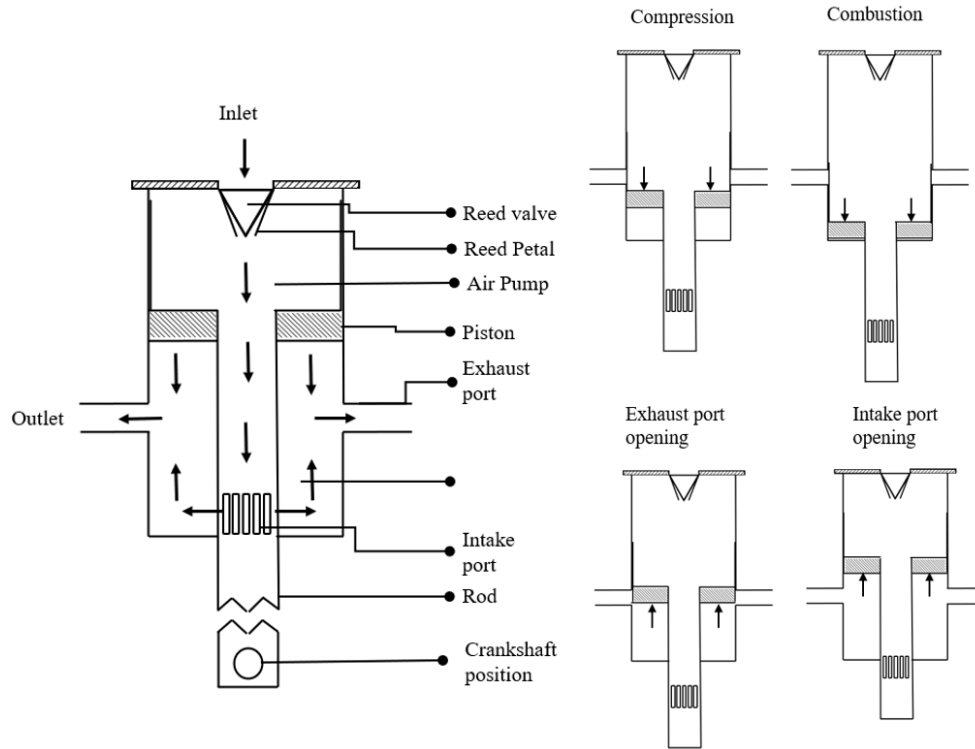
Figure 3.1: Schematic layout and working principle of the uniflow scavenged engine

Table 3.1: Engine Attributes

Attributes	Description
Displacement	755 cc
Bore/stroke	107/47.5 mm
Number of cylinders	1
Intake ports (slots/area)	16/730 [mm^2]
Exhaust ports (number/area)	13/1060 [mm^2]
Type of injection	Direct injection

This particular engine has a notably different intake port mechanism, as seen in Figure 3.1. The intake fresh charge enters the engine from the reed valve into the air pump and through the intake ports placed on the rod. The

intake ports are a series of slots opening into the combustion chamber. More-over, the exhaust ports open perpendicular to the intake ports, making the fluid flow as a uniflow scavenging engine. The 1D modeling subsection section 3.4 depicts a detailed description of the engine model control.

3.3 Experimental setup

The engine is installed and instrumented in a dynamic test rig with an AVL brake dynamometer, whose torque and rotational speeds are controlled by means of AVL PUMA software. The AVL Z133 spark plug is used to capture the necessary pressure pulsation in the combustion chamber with a sampling period of 0.5 crank-angle degrees. Kistler 601CAA piezoelectric-type sensors are employed to provide the pressure traces in the air pump and exhaust manifold. The average air and fuel mass flow are registered using AVL FLOW-SONIX Air and AVL 733S fuel balance, respectively. HORIBA MEXA 7100 DEGR is used to measure the raw emissions from the engine. A detailed description of the range and accuracy of these sensors is provided in Table 3.2.

Table 3.2: Engine test bench instruments

Variables	Equipment	Range	Accuracy
Speed	Dynamometer	6000 RPM	0.03% fs
Torque	Dynamometer	$\pm 415\ Nm$	0.05% fs
Cylinder Pressure	1AVL Z133	0 to 250 bar	0.3% lin.
Air Flow	AVL Flowsonix Air	20 to 720 kg/h	2%
Fuel Flow	AVL 733S Fuel meter	0-150 kg/h	0.2%
Mean Pressure	Kistler Piezo-Resistive Transmitter	0-10 bar	0.2% lin.
Gases Analysis	Horiba mexa 7100 DEGR	-	1-4 fs.
Temperature	K-type Thermocouple 7100	-200 to 1250 °C	-1.5 °C

Steady-state testing at three engines speeds and two exhaust layouts has been performed, and similar data using the depicted sensors are captured. The speeds include 2000 RPM with exhaust config-2 at full load and partial load conditions. Furthermore, using config-1 exhaust layout, full load tests are performed at 2250 and 2500 RPM. Table 3.3 depicts the information on the shape and geometry of each exhaust layout.

Table 3.3: Exhaust manifold configurations at different speeds and conditions

Exhaust Layout	Pipe details (mm)	Speed (RPM)	Load
Config-1 (C1)	1. Exhaust manifold with tapered pipe 2. Long pipe-1 (380 x 33.5) 3. Silencer (180 x 35) 4. Long pipe-2 (650 x 33.5)	2500 2250	Full Load (FL)
Config-2 (C2)	1. Exhaust manifold with tapered pipe 2. Long pipe-1 (274.5 x 35) 3. Silencer (280 x 109)-2 units 4. "U" pipe (213 x 35) 5. Long pipe-2 (650 x 33.5)	2000	Full Load Partial Load (PL)

The engine control unit (ECU) is provided with control of the injected fuel and throttle position, which is also integrated with an airflow meter placed at the intake of the air filter. Moreover, the instantaneous in-cylinder pressure signals are processed in real time to calculate the coefficient of variation (COV) and maximum amplitude of pressure oscillations (MAPO), combustion phase, and duration for every engine cycle. The COV is the measurement of cycle-to-cycle combustion variability, and the MAPO is the measurement of knock [59]. The combustion parameters are calculated by means of the apparent heat release (AHR). The AHR is an estimate of the heat released by the fuel, ignoring the heat transfer from the combustion chamber to the walls and by replacing the ratio of specific heat with a constant parameter k. Equation 3.1 presents with the first law of thermodynamics for the combustion chamber assuming ideal gas behavior, and Equation 3.2 provides with apparent heat release rate (AHRR), which is only a function of in-cylinder pressure and volume.

$$\frac{dQ_f}{dt} = \frac{c_p}{c_p - c_v} p_{cc} \frac{dV_{cc}}{dt} + \frac{c_v}{c_p - c_v} V_{cc} \frac{dp_{cc}}{dt} + \frac{dQ_w}{dt} \tag{3.1}$$

$$AHRR = \frac{k}{k-1} p_{cc} \frac{dV_{cc}}{dt} + \frac{1}{k-1} V_{cc} \frac{dp_{cc}}{dt} \tag{3.2}$$

Where p_{cc} and V_{cc} are the instantaneous pressure and volume of the combustion chamber, Q_f is the heat released by the fuel, Q_w is the heat transfer

from the combustion chamber to the walls, and the term c_p and c_v are the specific heat capacities of the in-cylinder gases at constant pressure and volume, respectively.

Using the aforementioned procedure and sensors, 100 consecutive engine cycles' information is captured, and the data for an engine speed of 2250 RPM is plotted in Figure 3.2 as an example. In the figure, plot A depicts the pressure evolution plotted against the volume inside the cylinder. The variability in the pV evolution can be attributed randomness of the air motion inside the cylinder. To overcome this problem, IMEP calculations are established, and the results for all the cycles are plotted. The results for the latter calculations are plotted in Figure 3.2B. For the engine speed of 2250 RPM, 3.6 bar is the most recurring engine cycle, which is plotted with a red solid line. A similar procedure is followed for all engine running conditions.
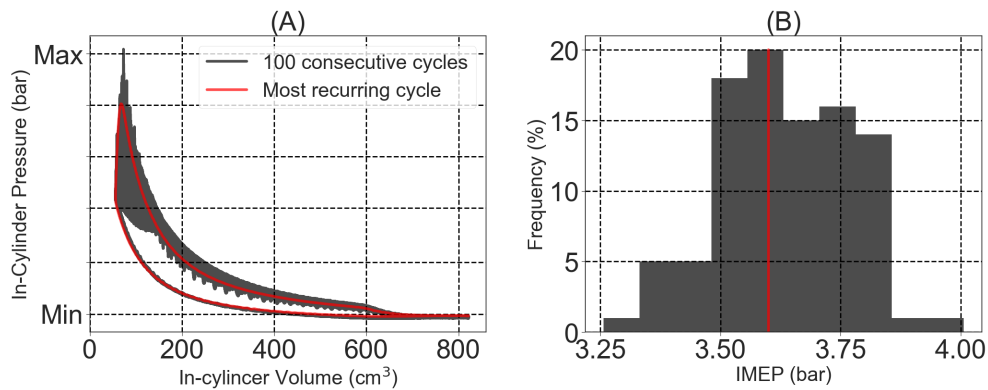

Figure 3.2: 2250 RPM Experimental data for A. pV diagram for 100 consecutive cycles, B. Frequency distribution for all IMEP engine cycles

From the above information, results presented in Figure 3.3 show the instantaneous pressure pulses inside the cylinder and exhaust manifold. The plot display the results for various engine speeds, load conditions, and exhaust layouts. These results will be used to validate the 1D model in chapter 5. Cycle-averaged results for intake air mass flow, injected fuel, and throttle position are also captured.
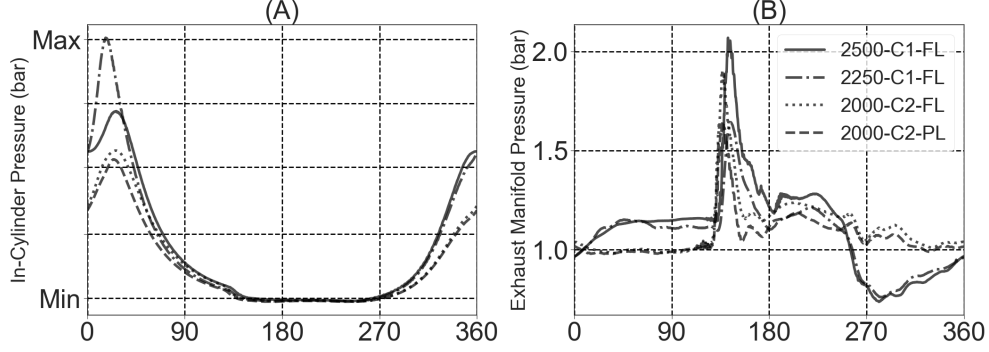
Figure 3.3: Experimental data for A. In-cylinder pressure, B. Exhaust manifold pressure

3.4   1D Modeling

The model used for the application is developed using Virtual Engine Model (VEMOD), internal software developed at CMT-Clean Mobility and Thermofluids [60] for visualizing the engine performance. The software groups elements as 0D or 1D elements depending on the spatial dimensions. In 0D elements, all the properties inside the element are constant, while in 1D elements, thermofluid dynamic properties vary versus the length of the element. These 1D elements are used as intake and exhaust lines, and when the length-to-diameter ratio is high enough, the flow inside the element is fully developed. So, the most important axis for the flow movement is the X-axis. Significantly reducing the calculation time as Y and Z axis are not relevant. This led to the proposal of a hyperbolic system of partial differential equations of simplified 1D Euler equations for unsteady compressible non-homentropic flow [60]. The most generic equation of the partial differential equation is provided in Equation 3.3.

$$\frac{\partial W}{\partial t} + \frac{\partial F}{\partial t} + C_1 + C_2 = 0 \tag{3.3}$$

Where W is the solution vector, F represents the flux vector for mass, momentum, and energy. While C_1 and C_2 include the source term that takes into account the effects of heat transfer, change in area, and friction. The flow properties can be obtained at every node of the duct and a given time

35

instant, considering different numerical methods, time marching, and spatial discretization techniques. Moreover, it is likely to estimate the inclusion of the chemical species transport equation to the governing equations system with the same level of precision as the applied numerical methods and without changes in the solution procedure. The chemical species conservation equation in vector form is:

$$\frac{\partial(\rho Y F)}{\partial t} + \frac{\partial(\rho u Y F)}{\partial x} = \rho F \dot{Y} \tag{3.4}$$

where Y is a vector including the mass fraction of n-1 different chemical species. Bearing in mind the chemical species transport in 1D elements, the governing equations system expressed in a conservative form is formulated as:

$$W(x,t) = \begin{bmatrix} \rho F \\ \rho u F \\ F(\rho \frac{U^2}{2} + \frac{p}{\gamma-1}) \\ \rho F Y \end{bmatrix}; F(W) = \begin{bmatrix} \rho u F \\ (\rho u^2 + p)F \\ uF(\rho \frac{U^2}{2} + \frac{\gamma p}{\gamma-1}) \\ \rho u F Y \end{bmatrix} \tag{3.5}$$

$$C1(x,W) = \begin{bmatrix} 0 \\ -p\frac{dF}{dX} \\ 0 \\ 0 \end{bmatrix}; C2(W) = \begin{bmatrix} 0 \\ g\rho F \\ -q\rho F \\ \rho F \dot{Y} \end{bmatrix} \tag{3.6}$$

The engine model, in addition to the pipes, also includes connections, valves, cylinders, and plenums. All the discharge coefficients of the ports and valves are tuned and validated against experimental or CFD data. These elements are used for modeling the novel engine with a 0D-1D approach. The developed model uses design data for its geometry and experimental results to validate engine performance, as will be described in the model validation sub-section.

Figure 3.4 gives information on the major details of the engine. The major parts are the reed valve, air pump, exhaust, intake ports, and main engine block consisting of piston and combustion chamber. The engine block developed in the model assessment uses an opposed 2-stroke engine, whose cylinder is considered as a 0D element. The piston position is set by comparing the volume of the combustion chamber with experimental results. Each major

element is controlled by a sub-model considering the piston position. These include the air pump volume, intake, and exhaust ports opening and closing. Several sensors capture necessary information on mass flow rate, volume, pressure, and temperature inside the cylinder and pipes. The information gathered is then used to develop the sub-systems for control of piston position, air pump volume, ports opening and closing, and reed valve petal opening. The modeling details of the sub-systems are as follows. A discharge coefficient is used for the intake and exhaust port opening and closing and is a function of the piston position. The discharge coefficient of the ports is calibrated to attain the instantaneous mass flow rates obtained in the CFD simulations.
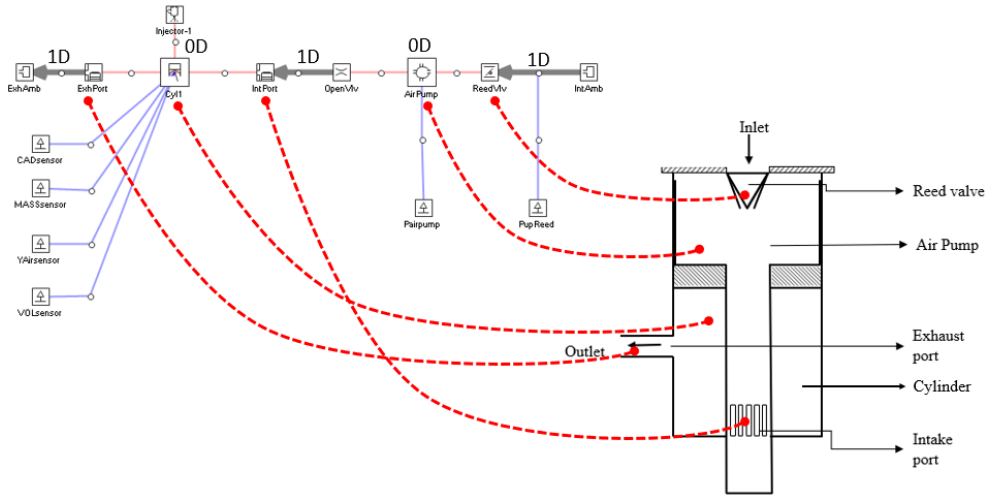

Figure 3.4: Simplified engine model in VEMOD with 0D or 1D elements

From Figure 3.1, it can be seen that the volume of the air pump changes with the piston position. For this reason, the air pump is modeled as a variable volume. The reed valve petal is assumed to be a punctual mass concentrated in the petal tip. The lift follows the classical mass-spring-damper model, where the external force depends on the pressure difference upstream and downstream of the valve. The force balance equation is used to deduce the tip lift given by:

$$F = m\ddot{x} - b\dot{x} - kx \tag{3.7}$$

Where x is the petal tip lift, k is the spring constant, m is the petal mass, b is the damper coefficient, and F is the external force calculated with:

$$F = (p_{airpump} - p_{upreed})A_{Petal} \tag{3.8}$$

Where A_{Petal} is the area of the petal, $p_{airpump}$ is the pressure downstream of the reed valve, and p_{upreed} is the pressure upstream of the reed valve. Once the petal lift is obtained, a discharge coefficient is calculated and used in the next simulation time.

For the combustion settings during the modeling stage, a simple Wiebe function model is selected due to its simplicity and low computational cost [59]. The Wiebe function is presented in Equation 3.9:

$$X_{fb} = 1 - exp\left(-C\left(\frac{\alpha - \alpha_0}{\Delta\alpha}\right)^{m+1}\right) \tag{3.9}$$

Where X_{fb}, α, α_0 and $\Delta\alpha$ are the mass fraction of fuel burned, the instantaneous crank angle, the crank angle at which the combustion starts, and the combustion duration. The adjustable parameters C and m define the combustion efficiency and the shape of the heat release rate. The value for m is usually around 2 for SI engines, and C is around 6, assuming that 99.9% of the fuel injected is burnt at the end of the combustion process. The accurate prediction of the pressure during combustion using the above methodology is depicted in chapter 5.

3.5   3D CFD model

A commercial Computational Fluid Dynamics (CFD) code was used to implement the numerical model of the cylinder. A summary of the main features of the numerical model is shown in Table 3.4. The most relevant physical models, numerical schemes, and mesh details are presented here. The basis of the model has been widely described in previous investigations [61].

Table 3.4: CFD model setup

Mesh Details	
Base Size	4 mm
Cell size intake/exhaust	2mm
Combustion chamber size	1mm
Walls refinement	0.5 mm
Minimum cell size by AMR	0.25 mm
Numerical schemes	
Spatial discretization	The second-order central difference scheme
Temporal discretization	the first-order central difference scheme
Momentum equation correction	PISO algorithm [62]
Physical models	
Turbulence	URANS RNG k-ϵ [63]
Heat transfer	O'Rourke and Amsden [64]

The computational domain obtained from the sketch of Figure 3.1 was meshed using a modified cut-cell Cartesian method directly in run time. The base grid mesh (4 mm) was reduced in those regions where flow features have higher complexity. For instance, intake/exhaust ports were refined to 2 mm in cell size. Moreover, an adaptive mesh refinement (AMR) strategy was considered to increase the grid resolution in those regions where the sub-grid field is more prominent. AMR cell size decreases to 0.25 mm when the sub-grid scale of velocity exceeds 1 m/s. A second-order central difference scheme was considered for spatial discretization, and a first-order scheme was considered for temporal discretization. The pressure-velocity coupling was solved by a modified Pressure Implicit with a Splitting of Operators (PISO) algorithm [65]. The in-cylinder turbulence was modeled in the frame of unsteady Reynolds-averaged Navier-Stokes (URANS) with the eddy-viscosity-based two-equation turbulence model (RNG k-ϵ model), widely extended in ICE applications [64].

Regarding the boundary conditions, the piston, liner, and cylinder head wall temperatures were estimated from the experiments by a lumped thermal model. All instantaneous signals at the intake/exhaust manifolds were obtained from the 1D model described in the previous section and provided as inflow/outflow boundary conditions. The wall heat transfer was estimated by the O'Rourke and Amsden model [66]. This approach is suitable for those simulations in which the turbulent boundary layer resolution is insufficient (i.e., in ICE simulations where the viscous sub-layer is not strictly resolved). The model calculates the wall heat transfer.

$$K\frac{\partial T}{\partial x_i} = \frac{\mu_m c_p T(T_f - T_w)n_i}{Pr_m y} \tag{3.10}$$

$$F = \begin{cases} 1 & y' < 11.05 \\ \dfrac{\dfrac{y'Pr_m}{Pr_t}}{\dfrac{1}{k}ln(y')+B+11.05(\frac{Pr_m}{Pr_t}-1)} & y' > 11.05 \end{cases} \tag{3.11}$$

$$y' = \frac{\rho u_\tau y}{\mu_m} \tag{3.12}$$

Where K is the molecular conductivity, Pr_m is the molecular Prandtl number, Pr_t is the turbulent Prandtl number, T_f is the fluid temperature, T_w is the temperature of the wall, the u_t is the shear speed, k is the Von Karman constant (0.4187), and B is a constant that depends on the turbulence model. The convective heat transfer in fluid during scavenging is calculated using the above model to predict the heat transfer coefficient. Then, this heat transfer coefficient will be used in subsequent studies.

Chapter 3 references

[59] J. Galindo, H. Climent, J. De la Morena, D. González-Domínguez, S. Guilain, and T. Besançon. "Assessment of air-management strategies to improve the transient performance of a gasoline engine under high EGR conditions during load-decrease operation". *International Journal of Engine Research* 24.(2) (2023), pp. 506–520 (cit. on pp. 33, 38).

[60] J. Galindo, J. R. Serrano, F. J. Arnau, and P. Piqueras. "Description of a Semi-Independent Time Discretization Methodology for a One-Dimensional Gas Dynamics Model". *Journal of Engineering for Gas Turbines and Power* 131 (3 May 2009). ISSN: 0742-4795. DOI: 10.1115/1.2983015 (cit. on pp. 35, 52).

[61]   A. Broatch, R. Novella, J. García-Tíscar, and J. Gomez-Soriano. "Potential of dual spray injectors for optimising the noise emission of gasoline partially premixed combustion in a 2-stroke HSDI CI engine". *Applied Thermal Engineering* 134 (Apr. 2018), pp. 369–378. ISSN: 13594311. DOI: 10.1016/j.applthermaleng.2018.01.108 (cit. on p. 38).

[62]   A. Broatch, R. Novella, J. García-Tíscar, J. Gomez-Soriano, and P. Pal. "Analysis of combustion acoustic phenomena in compression–ignition engines using large eddy simulation". *Physics of Fluids* 32 (8 Aug. 2020), p. 085101. ISSN: 1070-6631. DOI: 10.1063/5.0011929 (cit. on p. 39).

[63]   R. Issa. "Solution of the implicitly discretised fluid flow equations by operator-splitting". *Journal of Computational Physics* 62 (1 Jan. 1986), pp. 40–65. ISSN: 00219991. DOI: 10.1016/0021-9991(86)90099-9 (cit. on p. 39).

[64]   V. Yakhot and S. A. Orszag. "Renormalization group analysis of turbulence. I. Basic theory". *Journal of Scientific Computing* 1 (1 1986), pp. 3–51. ISSN: 0885-7474. DOI: 10.1007/BF01061452 (cit. on p. 39).

[65]   A. Amsden. *KIVA-3V: A block-structured KIVA program for engines with vertical or canted valves.* Los Alamos National Laboratory (LANL), July 1997. DOI: 10.2172/505339 (cit. on p. 39).

[66]   A. Torregrosa, P. Olmeda, B. Degraeuwe, and M. Reyes. "A concise wall temperature model for DI Diesel engines". *Applied Thermal Engineering* 26 (11-12 Aug. 2006), pp. 1320–1327. ISSN: 13594311. DOI: 10.1016/j.applthermaleng.2005.10.021 (cit. on p. 39).

Chapter 4

Contributions to modeling of uniflow-scavenged two-stroke engines

Contents

4.1 Introduction

This chapter focuses on different heat transfer models and scavenging characteristic curves. Firstly, a state-of-the-art and proposed heat transfer model is presented. The accuracy of the proposed heat transfer model in capturing the temperature profile during scavenging is presented in chapter 5. The proposed model considers the velocity of the air mass flow inside the cylinder, which is calculated using instantaneous mass flows during the opening and closing of the intake and exhaust ports. This consideration distinguishes the proposed model from the other state-of-the-art heat transfer models. The proposed heat transfer model combines the Woschni heat transfer model during the combustion and compression strokes, while the proposed model is activated during scavenging. Secondly, a synthetic scavenging characteristic curve is defined to represent the short-circuiting of air during the scavenging process accurately.

The chapter is structured as follows: Section 4.2 provides a literature review of state-of-the-art heat transfer models and their applicability, along with information on how these models are developed in a 1D model. Section 4.2.2 provides detailed information on the mathematical modeling used to develop the proposed heat transfer model. The details of the scavenging characteristic curves and their impact on engine performance are discussed in Section 4.3.

4.2 In-cylinder heat transfer

Advanced two-stroke engines are being studied for their potential to lower emissions for sustainable mobility. This can be attributed to the compactness of the engine, which can be heavily downsized, and have fewer emissions due to its design and operating range. Extensive literature is available with results for the initialization of the free piston to control pollutants. These assessments mainly focus on simulation, where the engine models are calibrated using the respective engine prototypes experimental results. For the control of a free piston, a fast response dynamic model is presented by Jia et al. [67]. The above-simplified model has shown the advantage of extensive studies as it could be coupled to any computing software and real-time hardware in the loop. The same research group in [68] presented sub-models for starting the process of a free-piston engine generator along with steady-state operation considering heat transfer correlations and air leaks and used the model to

study various starting motor forces and combustion processes. Jia et al. [69] have presented results with resonance-based actuation of free piston engines and have shown improved model prediction to experimental results while comparing results with dynamic modeling. Cha et al. [70] have studied the effect on in-cylinder thermodynamics due to combustion and presented critical observations for isentropic expansion and kinetic energy recovery. Jia et al. [71] proposed a new cascade model to control the free piston and have shown improved peak prediction and settling time. Li et al. [72] assessed a feed-forward controller for tracking performance and compared results with experimental data to demonstrate the effectiveness of the feed-forward control. Feng et al. [73] have implemented a switching strategy between motor/generator power to start the free piston engine to a steady state. Dizo et al. [74] studied a prototype engine where rotating cylinders powered by compressed air and depicted the disadvantages of such engines over conventional combustion engines. Kim et al. [75] have assessed the combustion effect on a free-piston engine for high performance. Kim et al. [75] and Mikalsen et al. [76] (divided into two parts) [77] have implemented precision piston control using PID and PDF (Pseudo Derivative Feedback) controllers, respectively, to control the engine speed and studied the cycle-to-cycle variation in the combustion process. Studies on the effect of varying engine stroke length and compression ratio found fewer advantages in a free-piston engine performance [78].

Another aspect of engine model improvement could be the effect of the heat transfer coefficient. Although, arguably, the existing heat transfer correlations are the only viable solution for automotive four-stroke engines, not for the upcoming two-stroke engine. Dabbaghi et al. [79] studied the effect of different heat transfer correlations to predict the in-cylinder pressure and temperature. They concluded that Anand and Hohenberg's heat transfer correlation has better predictions than Woschni and Sitkeis heat transfer correlation in their engine configuration. A new heat transfer model accounting for tumble motion is predicted in a two-stroke HSDI diesel engine and compared results with the Woschni model to confirm improvements of up to 70% in RMSE, as depicted in [80]. Hou et al. [81] have studied the effect of heat transfer on the ideal air standard cycle by considering the heat loss during the cycle of a real engine and have shown improved engine performance over a diesel engine. In the engine simulation, a highly accurate heat transfer coefficient must be used in the exhaust system to predict engine performance. This led to a proposal of a new heat model by considering the turbulence decay, velocity fluctuations, and results on enhanced predictions in engine performance are presented in

[82]. A two-zone combustion model for SI engines heat transfer correlations is evaluated by Lounici et al. [83], considering heat loss to the chamber and heat exchange during knocking for better predictability. A multi-zone thermodynamic model for SI engine model prediction is assessed by considering flame wrinkling, flame development, geometry, and heat transfer for accurately modeling the engine combustion process [84]. The same has been reassessed by Illán et al. [85], who have shown CFD comparisons for high accuracy. Descieux et al. [86] have performed studies for thermodynamic performance improvement of a diesel engine considering heat transfer and friction loss and showed power and efficiency improvement. Using heat release of combustion data, a calibrated heat transfer correlation has been assessed by Guezennec et al. [87] for enhanced model prediction. Not only the effects of heat transfer on combustion engines are studied but also in sustainable mobilities like battery electric vehicles are also assessed. A numerical review of lithium-ion batteries is presented in [88], studying the effects of heat transfer for thermal run-away. The effect of heat transfer in a Stirling engine is studied for waste heat energy recovery by Catapano et al. [89]. Reliable conjugate heat transfer methodologies to reduce the effect of engine heat losses are depicted in [90]. To reduce heat transfer losses and increase thermal efficiency, an in-cylinder thermal barrier coating technique is studied by Yan et al.[91].

Heat transfer utilizes major energy loss of the total energy produced that is passed to the engine coolant. Of the total heat transfer energy, more than 50% comes from the in-cylinder and the rest, majorly from exhaust ports. Two types of heat transfer occur in the conventional SI and CI engine, one due to convection and the other is radiation. Most heat transfer in SI engines depends on convection, while the heat transfer due to radiation is limited to a maximum of 20%. On the contrary, in CI engines, most heat transfer happens due to radiation; studies have shown that the radiative heat transfer for CI engines can reach up to 40%. A most general heat transfer correlation considering the convective heat transfer correlation is given in Equation 4.1.

$$\dot{Q} = h_g A(T_g - T_w) \tag{4.1}$$

Where h_g is the convective heat transfer coefficient, A is the area exposed which is the combustion chamber surface, and T_g and T_W are the gas and wall temperature, respectively.

4.2.1 State of the art models

Over the years, as mentioned earlier, several researchers have investigated different heat transfer correlations. The correlations investigated use the mean piston velocity to calculate the instantaneous heat transfer coefficient for CI engines and were also usable for SI engines. Convection models used for this assessment are described below.

4.2.1.1 Woschni correlation

Woschni correlation is the most commonly applied heat transfer relation for both diesel and SI engines, and the expression is given in Equation 4.2 [92].

$$h_g = aC_0 B^{0.2} p^{0.8} w^{0.8} T^{-0.53} \tag{4.2}$$

Where the cylinder bore is denoted with B, p, and T are the instantaneous pressure and temperature in the cylinder, respectively, and a is the correction multiplier. The constant C_0 is in the range of 110-130. From Equation 4.2, it can be deduced that the heat transfer coefficient will behave similarly to the in-cylinder pressure evolution with some adjustments given by the other parameters. Furthermore, w is the Woschni correlation given by Equation 4.3:

$$w(\theta) = C_1 \bar{U}_p + C_2 \frac{V_d T_r}{p_r V_r}(p(\theta) - p_m) \tag{4.3}$$

Where $\bar{U}_p$ is the mean piston velocity, V_r is the reference volume, and p_r and T_r are the reference pressure and temperature. These pressure, temperature, and volume can be considered at the start of combustion or when the inlet valve closing occurs. Finally, p is the instantaneous pressure inside the cylinder with respect to the crank angle (θ), and p_m is a function of reference pressure and instantaneous in-cylinder volume given by:

$$p_m = p_r \left(\frac{V_r}{V}\right)^n \tag{4.4}$$

The constants C_1 and C_2 depend on the piston phase, and Table 4.1 provides information on the calibrated values for these constants.

Table 4.1: Woschni Correlation constants

Phase	C_1[-]	$C_2\left[\frac{m}{sk}\right]$
Intake	6.18	0
Compression	2.28	0
Combustion	2.28	$3.24 \times$ 10-3
Expansion	2.28	$3.24 \times$ 10-3
Exhaust	6.18	0

4.2.1.2 Hohenberg

Woschni correlation provides a higher averaged heat transfer coefficient during the cycle due to his approximation. As Hohenberg flaws the results from the Woschni correlation, he gave a new correlation for calculating instantaneous heat transfer by using the following equation in Equation 4.5.

$$h_g = C_1 V_c^{-0.06} p^{0.8} T^{-0.4} (C_2 + \bar{U}_p) \tag{4.5}$$

Where V_c is the cylinder volume, and p and T are the respective pressure and temperature in the combustion chamber. The constant for C_1 and C_2 obtained by Hohenberg was precisely measured for diesel engines by heat balance, heat flux, and combustion chamber temperatures. The values are kept constant at 130 and 1.4, respectively. He has demonstrated that his correlation could predict temperatures with an accuracy of 10% marginal Error [93].

4.2.1.3 Annand

Annand predicted the instantaneous heat transfer coefficient using Nusselt and Reynolds non-dimensional numbers [94]. His correlation considers both convection and radiative heat transfer coefficients. As for this engine application, radiative heat transfer is not used. Therefore, the correlation only considers the convective heat transfer coefficient and is given in Equation 4.6.

$$h_g = \frac{dk_{gas} Re^{0.7}}{B} \tag{4.6}$$

Where Re is the Reynolds number, B is the bore diameter, and k_{gas} is the thermal conductivity of the gas, which can be deduced from experimental polynomial curve fitting using the working temperature of the fluid. The coefficient d is the correction coefficient given by Annand using Sieder-Tate given in Equation 4.7 [95].

$$d = 0.023Pr^{0.4} \tag{4.7}$$

Where Pr is the Prandtl number, furthermore, the flow velocity used in the Reynolds number calculation is the mean piston velocity.

The correlations mentioned above are established based on 4-stroke diesel engine experiments. Due to the differences in the combustion principles between SI and CI engines, practically, these models cannot provide a viable solution but can be considered for SI engines as well. As mentioned earlier, several researchers have theoretically and practically provided that with minor adjustments, the above correlations can also be used for SI engines.

4.2.2 Proposed heat transfer model

The proposed model uses the velocity of the air mass flow calculated using instantaneous mass flows during the intake and exhaust ports opening and closing, which has yet to be accounted for in any heat transfer model described previously. Although the cylinder is considered as a 0D element as described in chapter 3, a spatial-averaged pseudo-mass flow rate inside the cylinder can be calculated using intake and exhaust mass flows, which can be expressed as shown in Equation 4.8.

$$\dot{m}^* = \left| \frac{\dot{m}_{in} + \dot{m}_{out}}{2} \right| \tag{4.8}$$

Where $\dot{m}_{in}$ and $\dot{m}_{out}$ are the instantaneous intake and exhaust mass flow rates, respectively. Furthermore, by using Equation 4.9, the pseudo-velocity variable is defined, which is an approximation for the spatial-averaged velocity field inside the cylinder (C^*), which is calculated as:

$$C^* = \frac{\dot{m}^*}{A\rho} \tag{4.9}$$

In which A is the area of the piston, and ρ is the density of the gases calculated using instantaneous pressure and temperature in the cylinder. Using the velocity, the non-dimensional Reynolds number (Re) is calculated with:

$$Re = \frac{DC^*\rho}{\mu} \tag{4.10}$$

Where D is the diameter of the combustion chamber, μ is the fluid dynamic viscosity. Using the correlation between the Reynolds and Nusselt numbers (Nu), Nu is calculated using Equation 4.11.

$$Nu = bRe^{0.7} \tag{4.11}$$

Where b is the correction coefficient, also, it is known that Nu is a function of convective heat transfer coefficient h_{ins}, a spatial dimension; in this case, the diameter of the combustion chamber (D) is used, and the thermal gases conductivity (k). The appropriate heat transfer coefficient is calculated using this correlation given in Equation 4.12.

$$h_{ins} = \frac{Nuk}{D} \tag{4.12}$$

The results plotted in Figure 4.1. give information on the convective heat transfer coefficient calculations adapted for this engine during scavenging in conjunction with the Woschni heat transfer coefficient calculated during combustion. The results plotted in Figure 4.1 (A) depict mass flow rates in the intake and the exhaust ports. Figure 4.1 (B) depicts the spatial-average mass flow rate calculated using Equation 4.8. Using Equation 4.9 to Equation 4.12, the convective heat transfer coefficient results during scavenging are calculated and plotted using a solid red line, as depicted in Figure 4.1 (C). In contrast, a solid blue line depicting Woschnis heat transfer coefficient calculated using Equation 4.2 is plotted in Figure 4.1 (C). The actual convective heat transfer coefficient actuated in the cylinder is plotted in Figure 4.1 (D). A min/max control objective is used to actuate the switch between the Woschni

heat transfer coefficient during combustion and the proposed transfer model during scavenging. From Figure 4.1 (C) and (D), it can be observed that the blue investigation window marked as 'a' during scavenging is initiated at the moment when the exhaust port opens and lasts till the exhaust ports close. In contrast, the Woschni convective coefficients are actuated during compression, combustion, and expansion strokes.
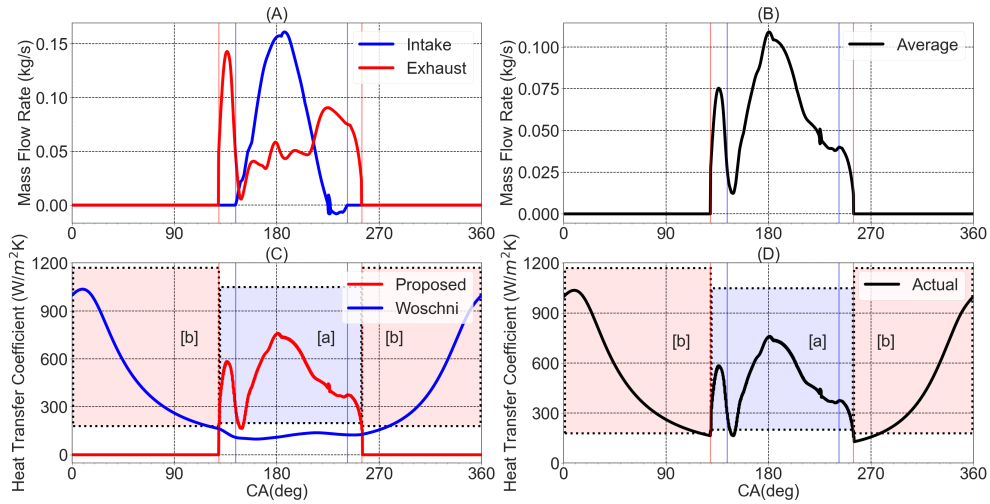

Figure 4.1: A: Mass Flow rate at intake and exhaust pipes, B: Average Mass Flow rate, C: Convective heat transfer for proposed and Woschni models, D: Actual Convective heat transfer of overall cycle.

From Figure 4.1D, a higher heat transfer coefficient is noted during the scavenging process, attributable to the rapid evolution of gas velocity within the cylinder in both space and time, especially in a uniflow scavenged engine. This phenomenon holds greater significance in these engines compared to their four-stroke counterparts.

4.3   Scavenging

The primary research focus of the 2-stroke engine is to attain higher scavenging and improve the engines performance. To attain higher scavenging, Wang et al. [96] optimized several parameters such as bore-stroke ratio, intake

scavenging ports, and intake design and have proven improved brake thermal efficiency using CFD analysis. A hybrid air operation assessment is performed for the same engine configuration to attain higher scavenging efficiency [97]. Once the engine parameters were optimized, the same research group assessed the engine with a turbocharger and presented results with enhanced brake power and torque [98]. The same scientist has also evaluated the effect of piston-shape design for enhanced scavenging and lower fuel consumption [99]. Benson et al. [100] have quantitatively assessed a mixing displacement method to improve scavenging, thereby improving charging efficiency in a two-stroke engine. Research is not only limited to downsized engines but also marine engines are tested for higher performance. Sakellaridis et al. [101] analyzed a marine two-stroke engine with a turbocharger and presented improved engine performance. Other researchers have also studied the effect of ignition timing for higher performance and lower emission in a SI two-stroke engine [102]. A three-phase scavenging model in the marine engine is studied using 2D CFD, and results are presented in [103]. Zhu et al. [104] studied different air control methods to assess a marine two-stroke engine for enhancement in scavenging. Kim et al. [105] studied a marine engines spray angle and injection position for optimum engine performance for low emissions.

Although the determination of the improved scavenging is measured in terms of enhanced engine performance, only a few researchers have studied how to estimate the trapped mass inside the cylinder. This estimation technique uses in-cylinder pressure traces to determine the trapped mass, as depicted by Bares et al. [106]. Carlucci et al. [107] have presented an inexpensive way to predict trapped mass by considering the molar concentration of $CO2$ and oxygen in the tailpipe. Leo et al. [108] proposed a technique in which experimental in-cylinder traces were used to calculate the trapped mass; their predictive methodology also depicts the air-to-fuel ratio. Using air mass flow and lambda sensors, Arsie et al. [109] predicted the trapped mass and air-to-fuel ratio, compared the results with the in-cylinder pressure method, and stated a high accuracy of predictability.

The scavenging model in VEMOD software [60] is distinguished into two zones, namely the fresh zone and the burnt zone. This separation differentiates the mass, temperature, and composition in their respective zones, as depicted in Figure 4.2. It is assumed that at the intake port opening, the total mass inside the cylinder is filled with burnt mass. Furthermore, the intake mass always enters the fresh zone, and the exhaust mass is a mixture of the fresh

mass and burnt mass following a defined scavenging curve. The mass and energy balance is calculated in every time step, and the exhaust temperature is obtained as mass averaged temperature.
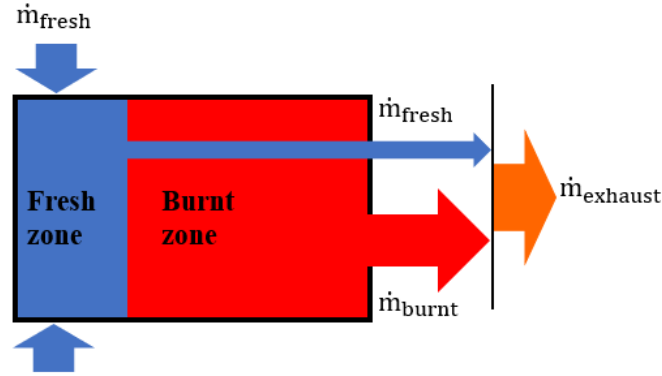

Figure 4.2: Definition of gas environment inside the cylinder

To assess the engines performance under the most desirable operating conditions, several coefficients are defined below. These parameters evaluate the gas exchange efficiency in a two-stroke engine. The correlations that need to be considered include the delivery ratio (DR), trapping efficiency (TE), scavenging efficiency (SE), and charging efficiency (CE).

The DR is the correlation between the mass of air supplied in the scavenging process and its reference mass. The reference mass is defined as the product of the volume and ambient air density and is defined as follows:

$$DR = \frac{m_{inlet}}{m_{ref}} \tag{4.13}$$

Equation 4.14 define the TE, which is a correlation of the mass of air retained in the cylinder to the mass of air supplied during the scavenging process.

$$TE = \frac{m_{ret}}{m_{inlet}} \tag{4.14}$$

The SE is expressed as the correlation between the mass of the residuals

from the previous cycle in the cylinder to the total mass trapped inside the cylinder. This trapped mass constitutes the sum of the mass of fresh charge and the mass of charge unburned from the previous cycle and is defined as follows:

$$SE = \frac{m_{ret}}{m_{trap}} \tag{4.15}$$

The CE is a product of TE and DR, where CE is expressed as the ratio between the mass of air retained in the cylinder to the mass which could fill the entire cylinder volume with the ambient air, which is the reference mass. Equation 4.16 defines CE

$$CE = TE \cdot DR = \frac{m_{ret}}{m_{ref}} \tag{4.16}$$

Figure 4.3 shows the terms that are considered while defining DR, TE, SE, and CE. The necessary calculation to obtain the masses depicted in Figure 4.3 are detailed in subsection 4.3.2.
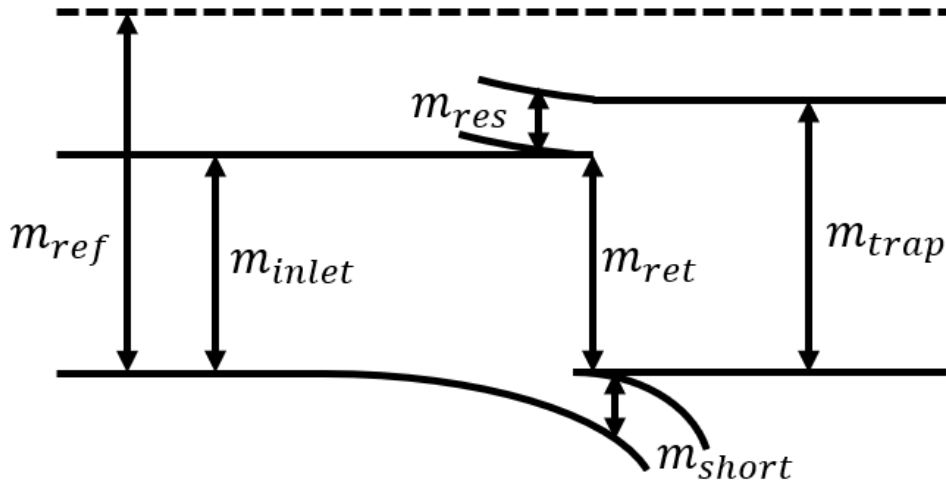
Figure 4.3: Flow diagram for scavenging parameters definition

There are two ideal models of scavenging: perfect displacement and perfect

mixing condition. The former is assumed when the combustion gases leave the chamber without mixing with fresh air. In contrast, in the latter, all the fresh charge perfectly mixes with the exhaust gases inside the cylinder as soon as the fresh charge enters the cylinder. In the case of perfect displacement condition $CE = DR$, where DR$\leq$1, and on the contrary, in the perfect mixing condition $CE = 1 - e^{-DR}$ and DR$\leq$1. As mentioned earlier, these two conditions are ideal conditions, but in the actual scenario, the scavenging process is a combination of both the processes mentioned above. In this thesis, the combination process is termed synthetic scavenging (SS). The major differences observed in the gas dynamics using perfect displacement (PD), perfect mixture (PM), and SS process are depicted subsection 4.3.1.

4.3.1 Gas dynamic analysis

Figure 4.4 shows the characteristics of the scavenging curve through the relationship between the cylinder residual ratio (CBR) and exhaust residual ratio (EBR), calculated using mass and mass flows, respectively and are calculated as follows:

$$CBR = \frac{m_{burnt}}{m_{fresh} + m_{burnt}} \tag{4.17}$$

Where m_{fresh} is the mass fraction of the fresh charge trapped inside the cylinder and m_{burnt} is the residual gases trapped inside the cylinder. On the other hand, EBR is calculated as the ratio of burnt mass flow in the exhaust manifold to the total mass rate in the exhaust and is depicted in Equation 4.18.

$$EBR = \frac{\dot{m}_{burnt}}{\dot{m}_{fresh} + \dot{m}_{burnt}} \tag{4.18}$$

Three different operating characteristics curves are depicted in Figure 4.4, along with four characteristic points, which include initial, transition, anchor, and target points. The three curves PD, PM, and SS start from the initial point of (1,1) and reach the target point (0,0). The target point of (0,0) is imaginary point where it is assumed that the 1D simulation would end. However, in reality this target point in the scavenging process is determined by CBR value which are the residual gases evolving from the next engine cycle.

PD characteristic curve is depicted using a dashed black line in Figure 4.4, where it can be seen that all the residual gases leaving the cylinder are observed in the exhaust manifold. On the contrary, in the PM characteristic curve (depicted using a dotted black line), it can be seen that, with a change in residual inside the cylinder, there is a linear variability in the residual observed in the exhaust manifold. This implies that the fresh charge entering the cylinder mixes with the rest of the exhaust gases leading to a higher short circuit of fresh air as soon as the intake ports open. The transition and anchor points are more relevant for the SS curve depicted with a solid black line. The transition point determines the proportion of the perfect scavenging, while the anchor point characterizes the trends and peaks of the short circuit of air.
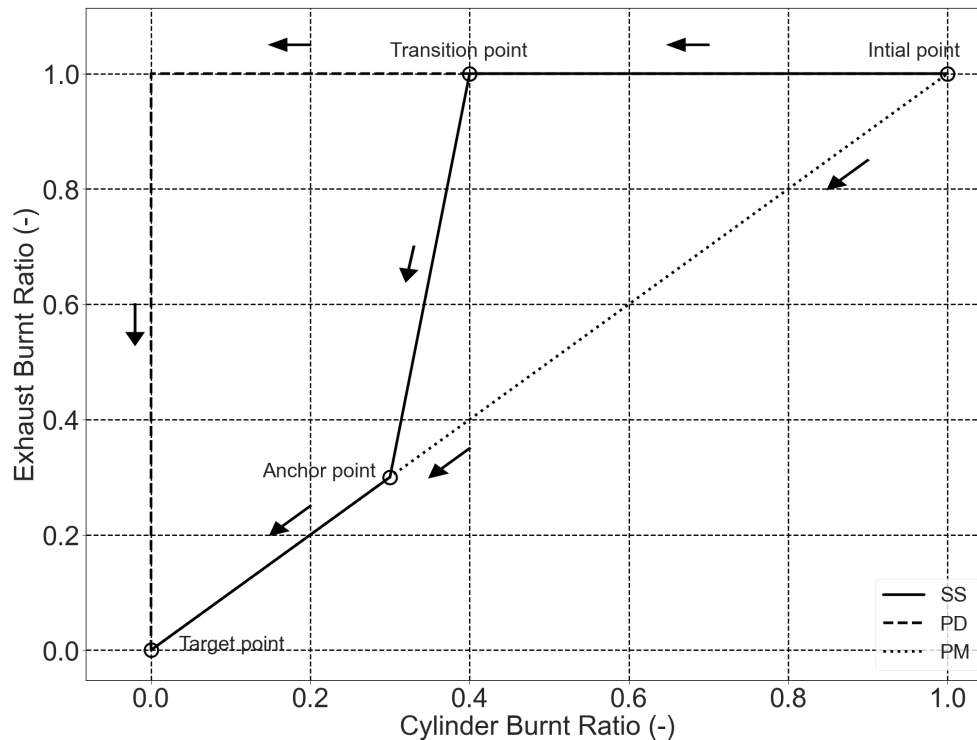
Figure 4.4: Characteristic map of scavenging curve

The major impact while changing the characteristic curve during scavenging can be seen in the total mass of the short circuit of air from the cylinder to the exhaust, trapped mass, and air and gas mass fraction inside the cylin-

der. These results are depicted in Figure 4.5, where PD is depicted using a dashed black line, SS using a solid black line, and PM by a dotted black line, respectively. To calculate the short circuit of air Equation 4.19 is used.

$$m_{short} = \int MF_{Air,burntzone} . \dot{m}_{exhaust} dt \qquad (4.19)$$

Where $\dot{m}_{exhaust}$ is the mass flow rate leaving the cylinder, and $MF_{Air,burntzone}$ is the air mass fraction inside the burnt zone.

To assess the potential differences seen while changing the scavenging curves, simulation based assessment is preformed at 2250 RPM using Config-1 exhaust manifold. Results for the same can bee seen in Figure 4.5. From Figure 4.5A, it can be seen that the PM characteristic scavenging curve provides the highest short circuit of air at approximately 0.28 g by the end of the scavenging process. This is because of the perfect mixture of the burnt gases with the fresh air, and the short circuit of air begins as soon as the intake mass flow interacts with the burnt gases i.e., close to the intake ports opening. On the other hand, due to a lack of perfect mixing between intake and exhaust gases in PD conditions, the short circuit of air is delayed, and a peak mass of about 0.025 g can be observed, which occurs when the cylinder is completely filled with air. In SS condition, which is a combination of both PM and PD characteristics curves, the trends and peaks are observed at the intermediate location of both curves with a peak short circuit of air of up to 0.22 g.

Furthermore, different characteristic curves have an impact on gas exchange occurring during the scavenging process i.e., mass fractions of air and gas. By the end of the scavenging process at 255 CAD, it can be observed from Figure 4.5 C and D that with the PD curve, the cylinder is completely filled with air, and for the same, the exhaust gases are almost negligible. At the same time, the remainder of the cylinder is filled with fuel mass fraction. Moreover, In PM condition, only 73% of the cylinder is filled with fresh charge while the remaining 27% is exhaust gas leading to differences in performance. Due to higher short-circuit of air in PM condition, the trapped is also affected, where a maximum trapped mass of 0.47 g at the end of the scavenging process is seen from Figure 4.5B. While from the same in PD condition, a peak trapped mass of 0.62 g can be seen. In contrast, the SS curve has an intermediate performance of both the scavenging curves.
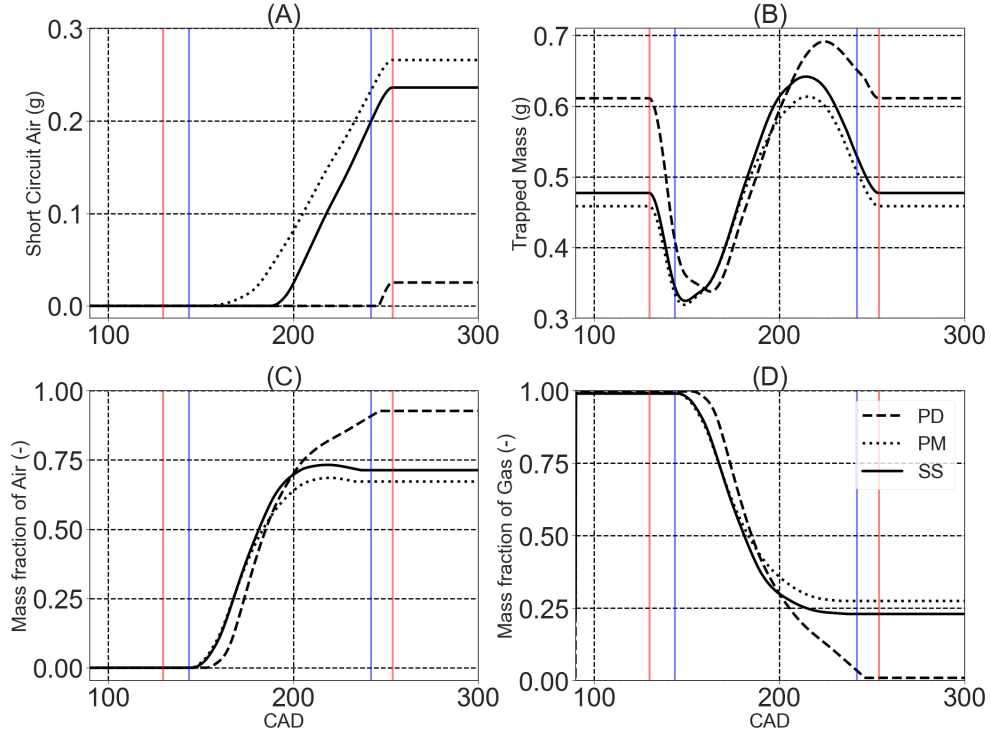
Figure 4.5: Gas dynamics analysis of the engine under different scavenging characteristics curves A. Short circuit Air (g), B. Trapped mass (g), C. Mass fraction of Air(-), and D. Mass fraction of Gas(-)

4.3.2   Scavenging analysis

From the above gas dynamic analysis, the necessary scavenging analysis is depicted in this section. To estimate the performance of the studied advanced two-stroke engine, the information depicted in Figure 4.3 is needed, and the equations depicted below are used for the necessary calculations.

For the calculation of reference mass m_{ref}, displacement volume V_{disp} and density of ambient air ρ are used and is as follows:

$$m_{ref} = V_{disp}\rho \tag{4.20}$$

To calculate the m_{inlet}, Equation 4.21 is used.

$$m_{inlet} = \int \dot{m}_{in,Cylinder} dt \tag{4.21}$$

Where, $\dot{m}_{in,Cylinder}$ denotes the mass flow rate entering the cylinder through the intake ports. To calculate the mass retained in the cylinder Equation 4.22 is used.

$$m_{ret} = m_{inlet} - m_{short} \tag{4.22}$$

As mentioned earlier, VEMOD software is used in developing this engine. The software captured instantaneous results of pressure, temperature, trapped mass, and several other parameters to assess the engine thermofluid dynamically. Therefore, the information related to trapped mass m_{trap} was directly available and used in the calculation. The accuracy of 1D model predictions is validated against experimental and CFD simulation results, which will be demonstrated in chapter 5. To calculate the mass of residual inside the cylinder, the following expression is used:

$$m_{res} = m_{trap} - m_{ret} \tag{4.23}$$

Using the depicted information on the mass calculations, the following analysis has been performed, and the results are tabulated in Table 4.2

Table 4.2: Scavenging parameters for each characteristic curve

Attributes (g)	PD	PM	SS
m_{ref}	0.919	0.919	0.919
m_{inlet}	0.591	0.573	0.575
m_{ret}	0.607	0.307	0.339
m_{short}	0.025	0.265	0.235
m_{res}	0.004	0.150	0.137
m_{trap}	0.611	0.458	0.477

From Table 4.2, it can be observed that a reference mass of 0.91g of air can be supplied to the engine. Furthermore, due to the maximum allowable

port height and under PD conditions, the intake mass is restricted to 0.59g. On the contrary, due to the differences in scavenging characteristic curves, the maximum allowable intake of approximately 0.57g can be seen in PM and SS conditions. Moreover, for the same, it can be observed that the short circuit of the air is higher, about 0.26 and 0.23g, respectively. At the same time, an almost negligible amount of fresh mass is short-circuited in PD conditions. To further assess the performance of the engine under different scavenging characteristic curves, DR, CE, SE, and TE diagrams are used and depicted in Figure 4.6.

As can be observed from Figure 4.6B, the maximum DR is about 0.6 under all three characteristic curves by the end of the scavenging process. From the same, it can also be seen that the three scavenging curves follow similar trends for DR. This limitation in the maximum DR can be attributed to the intake port opening maximum area. Figure 4.6C, depict the information on TE. Observing the trends for TE show that the short-circuit of air has an impact on TE. For instance, in the PD condition, the short-circuit of being close to the end of the scavenging process (from Figure 4.5) leading to higher TE of 0.95. While earlier short-circuit, as seen in PM and SS conditions, provided lower TE. Similarly, SE plotted in Figure 4.6A shows that SE for the PD condition is as high as 0.92, where all the gases in PD condition are pushed out of the combustion chamber due to air inlet. Furthermore, in PD condition it is seen that SE is not absolute 1 as the reminder of the cylinder is filled with fuel, leading to SE lower than 1. While on the other hand, in PM condition, a SE of 0.7 can be observed while the remainder of the cylinder is still filled with burnt gases. Slightly higher SE in SS condition can be observed from Figure 4.6A (solid black line). The CE at the end of the scavenging process is 0.64, 0.45, 0.51 under PD, PM, and SS curves, respectively, results observed from Figure 4.6D. Lower engine performance in terms of CE is attributed to higher short-circuit of fresh charge and reminder of burnt gases inside the cylinder in PM and SS conditions. Adding to the already existing lower DR impacting the CE under the PD condition as well.
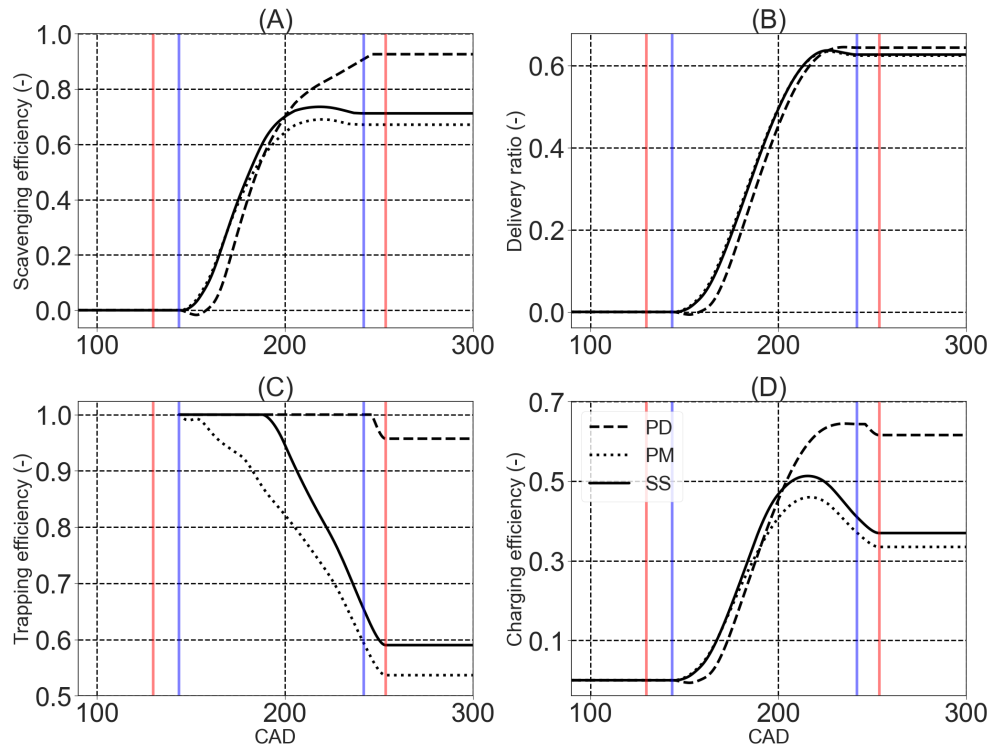
Figure 4.6: Scavenging metric under different scavenging characteristic curves A. Scavenging efficiency, B. Delivery ratio, C. Trapping efficiency, D. Charging efficiency.

Chapter 4 references

[60]   J. Galindo, J. R. Serrano, F. J. Arnau, and P. Piqueras. "Description of a Semi-Independent Time Discretization Methodology for a One-Dimensional Gas Dynamics Model". *Journal of Engineering for Gas Turbines and Power* 131 (3 May 2009). ISSN: 0742-4795. DOI: 10.1115/1.2983015 (cit. on pp. 35, 52).

[67]   B. Jia, A. Smallbone, H. Feng, G. Tian, Z. Zuo, and A. Roskilly. "A fast response free-piston engine generator numerical model for control applications". *Applied Energy* 162 (Jan. 2016), pp. 321–329. ISSN: 03062619. DOI: 10.1016/j.apenergy.2015.10.108 (cit. on p. 44).

[68] B. Jia, Z. Zuo, G. Tian, H. Feng, and A. Roskilly. "Development and validation of a free-piston engine generator numerical model". *Energy Conversion and Management* 91 (Feb. 2015), pp. 333–341. ISSN: 01968904. DOI: 10.1016/j.enconman.2014.11.054 (cit. on p. 44).

[69] B. Jia, Z. Zuo, H. Feng, G. Tian, A. Smallbone, and A. Roskilly. "Effect of closed-loop controlled resonance based mechanism to start free piston engine generator: Simulation and test results". *Applied Energy* 164 (Feb. 2016), pp. 532–539. ISSN: 03062619. DOI: 10.1016/j.apenergy.2015.11.105 (cit. on p. 45).

[70] S. H. Chan and J. Zhu. "Modelling of engine in-cylinder thermodynamics under high values of ignition retard". *International Journal of Thermal Sciences* 40 (1 Jan. 2001), pp. 94–103. ISSN: 12900729. DOI: 10.1016/S1290-0729(00)00274-X (cit. on p. 45).

[71] B. Jia, R. Mikalsen, A. Smallbone, Z. Zuo, H. Feng, and A. P. Roskilly. "Piston motion control of a free-piston engine generator: A new approach using cascade control". *Applied Energy* 179 (Oct. 2016), pp. 1166–1175. ISSN: 03062619. DOI: 10.1016/j.apenergy.2016.07.081 (cit. on p. 45).

[72] K. Li, C. Zhang, and Z. Sun. "Precise piston trajectory control for a free piston engine". *Control Engineering Practice* 34 (Jan. 2015), pp. 30–38. ISSN: 09670661. DOI: 10.1016/j.conengprac.2014.09.016 (cit. on p. 45).

[73] H. Feng, C. Guo, B. Jia, Z. Zuo, Y. Guo, and T. Roskilly. "Research on the intermediate process of a free-piston linear generator from cold start-up to stable operation: Numerical model and experimental results". *Energy Conversion and Management* 122 (Aug. 2016), pp. 153–164. ISSN: 01968904. DOI: 10.1016/j.enconman.2016.05.068 (cit. on p. 45).

[74] J. Dižo, M. Blatnický, M. Sága, and P. Šťastniak. "A Numerical Study of a Compressed Air Engine with Rotating Cylinders". *Applied Sciences* 11 (16 Aug. 2021), p. 7504. ISSN: 2076-3417. DOI: 10.3390/app11167504 (cit. on p. 45).

[75] J. Kim, C. Bae, and G. Kim. "Simulation on the effect of the combustion parameters on the piston dynamics and engine performance using the Wiebe function in a free piston engine". *Applied Energy* 107 (July 2013), pp. 446–455. ISSN: 03062619. DOI: 10.1016/j.apenergy.2013.02.056 (cit. on p. 45).

[76]   R. Mikalsen and A. Roskilly. "The control of a free-piston engine gener-
       ator. Part 1: Fundamental analyses". *Applied Energy* 87 (4 Apr. 2010),
       pp. 1273–1280. ISSN: 03062619. DOI: 10.1016/j.apenergy.2009.06.
       036 (cit. on p. 45).

[77]   R. Mikalsen and A. Roskilly. "The control of a free-piston engine
       generator. Part 2: Engine dynamics and piston motion control". *Ap-
       plied Energy* 87 (4 Apr. 2010), pp. 1281–1287. ISSN: 03062619. DOI:
       10.1016/j.apenergy.2009.06.035 (cit. on p. 45).

[78]   R. Mikalsen and A. Roskilly. "The design and simulation of a two-stroke
       free-piston compression ignition engine for electrical power generation".
       Applied Thermal Engineering 28 (5-6 Apr. 2008), pp. 589–600. ISSN:
       13594311. DOI: 10.1016/j.applthermaleng.2007.04.009 (cit. on
       p. 45).

[79]   M. Dabbaghi, M. Baharom, Z. A. Karim, A. R. A. Aziz, S. E. Mo-
       hammed, and E. Z. Z. A. "Comparative evaluation of different heat
       transfer correlations on a single curved-cylinder spark ignition crank-
       rocker engineHeat transfer modeling in exhaust systems of high-performance
       two-stroke engines". *Alexandria Engineering Journal* 60 (3 June 2021),
       pp. 2963–2978. ISSN: 11100168. DOI: 10.1016/j.aej.2021.01.035
       (cit. on p. 45).

[80]   P. Olmeda, J. Martín, R. Novella, and R. Carreño. "An adapted heat
       transfer model for engines with tumble motion". *Applied Energy* 158
       (Nov. 2015), pp. 190–202. ISSN: 03062619. DOI: 10.1016/j.apenergy.
       2015.08.051 (cit. on p. 45).

[81]   S.-S. Hou. "Heat transfer effects on the performance of an air standard
       Dual cycle". *Energy Conversion and Management* 45 (18-19 Nov. 2004),
       pp. 3003–3015. ISSN: 01968904. DOI: 10.1016/j.enconman.2003.12.
       013 (cit. on p. 45).

[82]   J. M. Luján, H. Climent, P. Olmeda, and V. D. Jiménez. "Heat transfer
       modeling in exhaust systems of high-performance two-stroke engines".
       Applied Thermal Engineering 69 (1-2 Aug. 2014), pp. 96–104. ISSN:
       13594311. DOI: 10.1016/j.applthermaleng.2014.04.045 (cit. on
       p. 46).

[83]   M. S. Lounici, K. Loubar, M. Balistrou, and M. Tazerout. "Investi-
       gation on heat transfer evaluation for a more efficient two-zone com-
       bustion model in the case of natural gas SI engines". *Applied Thermal*

Engineering 31 (2-3 Feb. 2011), pp. 319–328. ISSN: 13594311. DOI: 10.1016/j.applthermaleng.2010.09.012 (cit. on p. 46).

[84] S. Verhelst and C. Sheppard. "Multi-zone thermodynamic modelling of spark-ignition engine combustion – An overview". *Energy Conversion and Management* 50 (5 May 2009), pp. 1326–1335. ISSN: 01968904. DOI: 10.1016/j.enconman.2009.01.002 (cit. on p. 46).

[85] F. Illán and M. Alarcón. "Numerical analysis of combustion and transient heat transfer processes in a two-stroke SI engine". *Applied Thermal Engineering* 30 (16 Nov. 2010), pp. 2469–2475. ISSN: 13594311. DOI: 10.1016/j.applthermaleng.2010.06.018 (cit. on p. 46).

[86] D. Descieux and M. Feidt. "One zone thermodynamic model simulation of an ignition compression engine". *Applied Thermal Engineering* 27 (8-9 June 2007), pp. 1457–1466. ISSN: 13594311. DOI: 10.1016/j.applthermaleng.2006.10.002 (cit. on p. 46).

[87] Y. G. Guezennec and W. Hamama. "Two-Zone Heat Release Analysis of Combustion Data and Calibration of Heat Transfer Correlation in an I. C. Engine". In: Mar. 1999. DOI: 10.4271/1999-01-0218 (cit. on p. 46).

[88] M. Ghiji, S. Edmonds, and K. Moinuddin. "A Review of Experimental and Numerical Studies of Lithium Ion Battery Fires". *Applied Sciences* 11 (3 Jan. 2021), p. 1247. ISSN: 2076-3417. DOI: 10.3390/app11031247 (cit. on p. 46).

[89] F. Catapano, C. Perozziello, and B. M. Vaglieco. "Heat transfer of a Stirling engine for waste heat recovery application from internal combustion engines". *Applied Thermal Engineering* 198 (Nov. 2021), p. 117492. ISSN: 13594311. DOI: 10.1016/j.applthermaleng.2021.117492 (cit. on p. 46).

[90] X. Margot, P. Quintero, J. Gomez-Soriano, and J. Escalona. "Implementation of 1D–3D integrated model for thermal prediction in internal combustion engines". *Applied Thermal Engineering* 194 (July 2021), p. 117034. ISSN: 13594311. DOI: 10.1016/j.applthermaleng.2021.117034 (cit. on p. 46).

[91] Z. Yan, B. Gainey, and B. Lawler. "A parametric modeling study of thermal barrier coatings in low-temperature combustion engines". *Applied Thermal Engineering* 200 (Jan. 2022), p. 117687. ISSN: 13594311. DOI: 10.1016/j.applthermaleng.2021.117687 (cit. on p. 46).

[92]   G. Woschni. "A Universally Applicable Equation for the Instantaneous Heat Transfer Coefficient in the Internal Combustion Engine". In: Feb. 1967. DOI: 10.4271/670931 (cit. on p. 47).

[93]   G. Hohenberg. "Advanced Approaches for Heat Transfer Calculations". *SAE International* (1979). DOI: https://www.jstor.org/stable/44699090 (cit. on p. 48).

[94]   W. J. D. Annand. "Heat Transfer in the Cylinders of Reciprocating Internal Combustion Engines". *Proceedings of the Institution of Mechanical Engineers* 177 (1 June 1963), pp. 973–996. ISSN: 0020-3483. DOI: 10.1243/PIME_PROC_1963_177_069_02 (cit. on p. 48).

[95]   G. Blair. "Design and Simulation of Four-Stroke Engines". *SAE International* (1999) (cit. on p. 49).

[96]   T. I. C. Buidin and F. Mariasiu. "Modeling Approach of an Air-Based Battery Thermal Management System for an Electric Vehicle". *Applied Sciences* 11 (15 July 2021), p. 7089. ISSN: 2076-3417. DOI: 10.3390/app11157089 (cit. on p. 51).

[97]   X. Wang and H. Zhao. "A High-Efficiency Two-Stroke Engine Concept: The Boosted Uniflow Scavenged Direct-Injection Gasoline (BUSDIG) Engine with Air Hybrid Operation". *Engineering* 5 (3 June 2019), pp. 535–547. ISSN: 20958099. DOI: 10.1016/j.eng.2019.03.008 (cit. on p. 52).

[98]   X. Wang and H. Zhao. "Analysis of the Boost System for a High Performance 2-Stroke Boosted Uniflow Scavenged Direct Injection Gasoline (BUSDIG) Engine". In: Sept. 2020. DOI: 10.4271/2020-01-2007 (cit. on p. 52).

[99]   X. Wang and H. Zhao. "Effect of piston shape design on the scavenging performance and mixture preparation in a two-stroke boosted uniflow scavenged direct injection gasoline engine". *International Journal of Engine Research* 22 (5 May 2021), pp. 1484–1499. ISSN: 1468-0874. DOI: 10.1177/1468087419900072 (cit. on p. 52).

[100]   R. S. Benson and P. T. Brandham. "A method for obtaining a quantitative assessment of the influence of charging efficiency on two-stroke engine performance". *International Journal of Mechanical Sciences* 11 (3 Mar. 1969), pp. 303–312. ISSN: 00207403. DOI: 10.1016/0020-7403(69)90048-4 (cit. on p. 52).

[101] N. F. Sakellaridis, S. I. Raptotasios, A. K. Antonopoulos, G. C. Mavropou-los, and D. T. Hountalas. "Development and validation of a new turbocharger simulation methodology for marine two stroke diesel engine modelling and diagnostic applications". *Energy* 91 (Nov. 2015), pp. 952–966. ISSN: 03605442. DOI: 10.1016/j.energy.2015.08.049 (cit. on p. 52).

[102] J. Zareei and A. H. Kakaee. "Study and the effects of ignition timing on gasoline engine performance and emissions". *European Transport Research Review* 5 (2 June 2013), pp. 109–116. ISSN: 1867-0717. DOI: 10.1007/s12544-013-0099-8 (cit. on p. 52).

[103] M. I. Foteinos, A. Papazoglou, N. P. Kyrtatos, A. Stamatelos, O. Zo-gou, and A.-M. Stamatellou. "A Three-Zone Scavenging Model for Large Two-Stroke Uniflow Marine Engines Using Results from CFD Scavenging Simulations". *Energies* 12 (9 May 2019), p. 1719. ISSN: 1996-1073. DOI: 10.3390/en12091719 (cit. on p. 52).

[104] S. Zhu, Y. Gu, H. Yuan, Z. Ma, and K. Deng. "Thermodynamic analysis of the turbocharged marine two-stroke engine cycle with different scavenging air control technologies". *Energy* 191 (Jan. 2020), p. 116533. ISSN: 03605442. DOI: 10.1016/j.energy.2019.116533 (cit. on p. 52).

[105] J.-S. Kim, W.-J. Lee, V. C. Pham, and J.-H. Choi. "A Numerical Study on Fuel Injection Optimization for a ME-GI Dual-Fuel Marine Engine Based on CFD Analysis". *Applied Sciences* 12 (7 Apr. 2022), p. 3614. ISSN: 2076-3417. DOI: 10.3390/app12073614 (cit. on p. 52).

[106] P. B. Moreno. "In-cylinder pressure resonance analysis for trapped mass estimation in automotive engines". Universitat Politècnica de València, Sept. 2017. DOI: 10.4995/Thesis/10251/90423 (cit. on p. 52).

[107] A. P. Carlucci, A. Ficarella, D. Laforgia, and M. Longo. "An Easy and Inexpensive Way to Estimate the Trapping Efficiency of a two Stroke Engine". *Energy Procedia* 82 (Dec. 2015), pp. 17–22. ISSN: 18766102. DOI: 10.1016/j.egypro.2015.11.875 (cit. on p. 52).

[108] R. D. Leo. "Methodologies for Air-Fuel ratio and trapped mass estimation in Diesel engines using the in-cylinder pressure measurement". *Energy Procedia* 82 (Dec. 2015), pp. 957–964. ISSN: 18766102. DOI: 10.1016/j.egypro.2015.11.850 (cit. on p. 52).

[109]   I. Arsie, R. D. Leo, C. Pianese, and M. D. Cesare. "Estimation of in-cylinder mass and AFR by cylinder pressure measurement in automotive Diesel engines". *IFAC Proceedings Volumes* 47 (3 2014), pp. 11836–11841. ISSN: 14746670. DOI: 10.3182/20140824-6-ZA-1003.01602 (cit. on p. 52).

Chapter 5

Analysis of a uniflow-scavenged two-stroke engine

Contents

5.1 Introduction

In chapter 4, a new heat transfer model and a synthetic scavenging curve were presented. The validation of the 1D model developed using VEMOD software is performed by comparing it with 1D and 3D CFD simulation results. Initially, the 1D model is validated for fluid dynamic parameters using experimental data, and the differences in the 1D model predictions lead to the development of the above-mentioned models. In this chapter, the validation of the 1D model with experimental results is presented in section 5.2, which includes two exhaust system layouts, two engine load conditions, and three engine running conditions. The heat transfer assessment is conducted through four different analyses, comparing the 1D model with CFD results.

The subsection 5.3.1 focuses on the performance of the proposed model in capturing temperature and trapped mass profiles at 2250 RPM, while maintaining the same initial conditions as the CFD results. A further assessment of the proposed heat transfer model is carried out by comparing it with state-of-the-art models under similar peak heat transfer coefficients, engine running conditions, and combustion settings. Results are presented in subsection 5.3.2. The sensitivity analysis on the effect on trapped mass is presented in subsection 5.3.3, where the correction coefficients in the heat transfer models, as mentioned in chapter 4, are adjusted. Finally, the robustness of the proposed heat transfer model in predicting temperature and heat transfer coefficient profiles under all tested engine conditions is demonstrated in subsection 5.3.4.

The second half of the chapter focuses on modeling the short-circuit of air. The subsection 5.4.1 showcases the robustness of the synthetic scavenging curves in capturing the short-circuiting of air for all engine running conditions, with comparisons to CFD data. A total of 5 engine running conditions are tested, including 3 full load tests, one partial load test using exhaust configuration 1, and one full load test using exhaust configuration 2. The subsection 5.4.3 presents a sensitivity analysis, incorporating extreme conditions from previous studies, and investigates gas dynamics and scavenging metrics.

5.2 Model validation

As mentioned earlier, fluid-dynamic validation of the model is carried out using experimental results. IMEP calculations are performed for this assessment to showcase the engines overall performance. Moreover, pressures during the combustion process are shown to validate the combustion setting. To further assess the robustness of the model, exhaust manifold pressure and in-cylinder pressure during the scavenging process are also depicted.

Table 5.1 depicts the information on the IMEP calculated for both experimental and model prediction data. As mentioned previously, the experimental campaign consisted of tests at three engine speeds, two exhaust layouts, and two load conditions. This information is also accounted for during the model validation stage. Observing the percentage error between experimental and modeling IMEPs, it can be deduced that the model predicts accurate engine performance with an absolute maximum error below of 3%. The gas dynamic analysis while changing the exhaust system is described in subsection 5.4.2 of this chapter.

Table 5.1: Experimental to 1D model IMEP comparison

Speed/Config/Load	Experimental (bar)	1D model (bar)	Error(%)
2500/C1/FL	3.41	3.34	2.05
2250/C1/FL	3.67	3.75	-2.17
2000/C2/FL	3.59	3.50	2.50
2000/C2/PL	2.85	2.89	-1.40

To assess combustion settings, in-cylinder pressures are depicted in Figure 5.1 for each of the experimental results. On observing the results from Figure 5.1, it can be justified that the combustion methodology followed in modeling this particular engine provided results with an accurate prediction of combustion pressure, as presented in chapter 3.
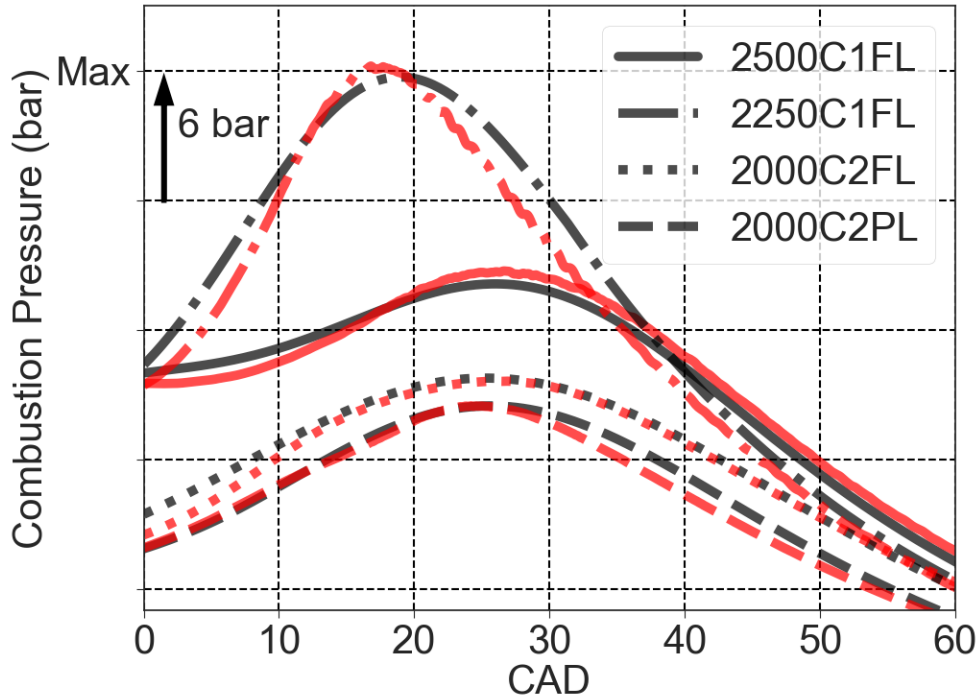
Figure 5.1: 1D model predictions to Experimental data comparison of combustion pressure, In red: Experimental data, and black: Model predictions.

Figure 5.2: depicts the information related to the 1D modeling results compared to experimental data. In Figure 5.2, the plots title gives the information on the engine speed in RPM, load condition-Full Load (FL)/Partial Load (PL), and the last digit 1 or 2 is the exhaust configuration which is either config-1 or config-2 respectively. The results plotted in Figure 5.2 (A)-(D) are the instantaneous pressure traces in the exhaust manifold, while (E)-(H) depict pressure traces inside the cylinder during the scavenging process. The results only illustrate the information while the exhaust ports are open because the gas exchange occurs during this process and defines the trapped mass in the cylinder for the next engine cycle.
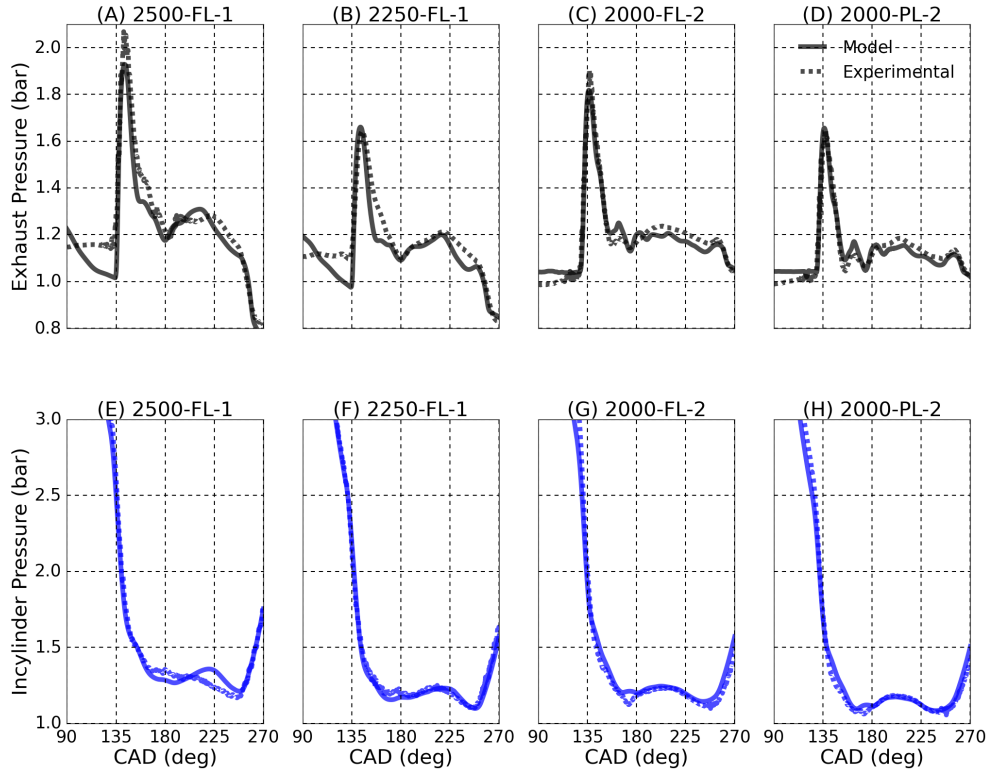
Figure 5.2: Comparison between experimental and 1D modeling results CAD Vs
(A)-(D) Exhaust pressure; (E)-(H) In-cylinder pressure.

Firstly, from Figure 5.2 (E)-(H), it can be observed that the exhaust port
opening occurs at 130 CAD. The results depicted before the exhaust port
opening is the expansion process, where it can be observed that the model-
ing results follow experimental results with close proximity. Also, it can be
observed that the port closing occurs approximately at 255 CAD, and the pro-
cess after this CAD is the compression stroke. During this process, it can be
seen that the 1D model accurately predicts the compression strokes pressure
compared to experimental results. The process between CAD 130 and 255 is
the scavenging process, where the modeling pressure traces follow the exper-
imental measurements with an absolute maximum deviation of less than 2%.
Observing the results, it can be justified that modeling strategies employed in
developing this novel engine provide accurate results during expansion, scav-
enging, and compression strokes in the combustion chamber.

Secondly, as mentioned earlier, during the experimental campaign, different exhaust systems were employed and tested at both full load and partial load conditions; this has also been accounted for during the modeling stage. To achieve coherence between experimental results and 1D model predictions, heat transfer and friction multipliers in the exhaust manifold were calibrated. Once a peak deviation of less than 2% is accomplished, these multipliers were held constant, and simulations were analyzed with different engine speeds and load conditions. Figure 5.2 (A)-(D) shows that the model is calibrated to predict experimental peaks and trends accurately. Figure 5.2 justifies that the model captures the in cylinder fluid dynamics results to a satisfactory level and can be used for further perspective analysis, or the results can be used as initial and boundary conditions for CFD.

5.3 In-cylinder heat transfer model

Heat transfer assessment is conducted in this section, where the state-of-the-art and proposed heat transfer models are compared to capture the in-cylinder temperature profiles during scavenging. Additionally, a perspective analysis is included to showcase the robustness of the model in the latter part. The results of this study are presented in [3].

5.3.1 Effects of heat transfer model

As mentioned in chapter 3, the results obtained from the 1D modeling simulations were utilized as initial conditions for the CFD simulations. This analysis aimed to investigate the thermal effects and the amount of trapped mass inside the cylinder since direct measurement of in-cylinder trapped mass and temperature is not feasible experimentally. Moreover, as mentioned in chapter 4, four different heat transfer coefficients are studied, which include Woschni, Hohenberg, Anand, and the proposed heat transfer model. All the heat transfer models are subjected to and studied under similar initial conditions during scavenging.

This study uses the information from the experimentally validated model at 2250 RPM with Config-1 exhaust manifold. All the heat transfer correlations are validated for the same initial conditions at the exhaust port opening, as
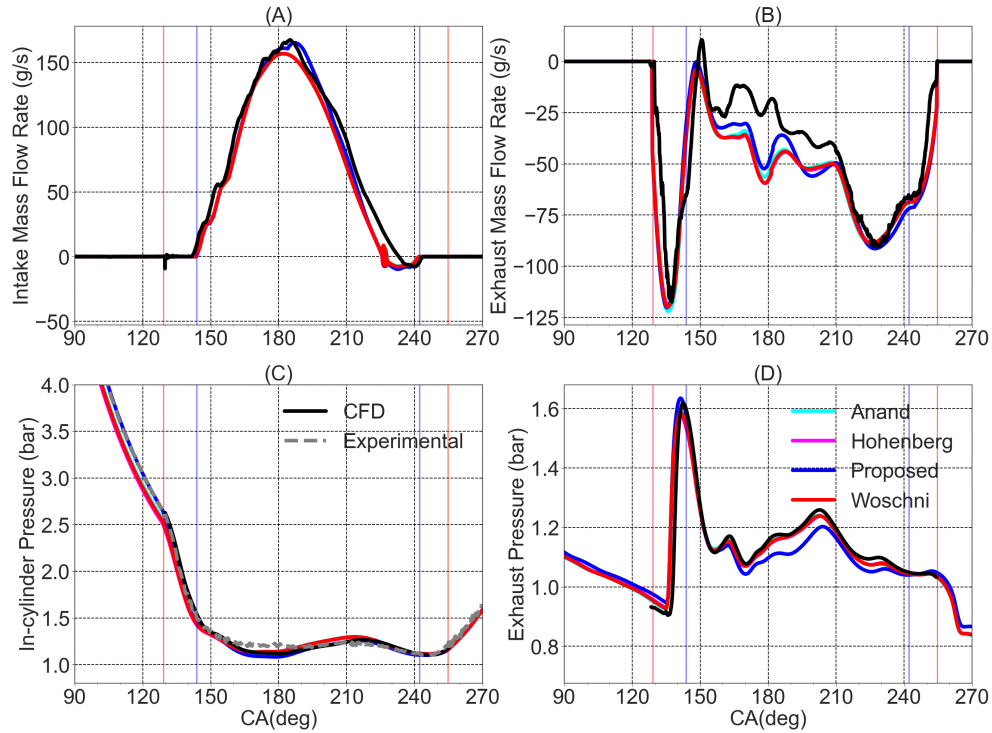
depicted in Figure 5.3.

Figure 5.3: 1D model to CFD comparison for different Heat Transfer Coefficients, A. Intake Mass flow rate, B. Exhaust mass Flow rate, C. In-cylinder pressure during scavenging process, D. Exhaust manifold pressure.

The information in Figure 5.3 shows that the fluid behavior for all heat transfer correlations, compared to CFD, is similar. These include the peaks and trends in the intake mass flow rate Figure 5.3(A), exhaust mass flow rate-Figure 5.3(B), pressure in the cylinder-Figure 5.3, and pressure in the exhaust manifold-Figure 5.3(D) during the scavenging process. At the same time, comparing results with the 1D model, Figure 5.3(C) not only shows the information of the 1D model to CFD comparison but also provides the information with experimental in-cylinder pressure traces. Showing the validation of not only experimental to 1D model but also experimental to CFD simulation predictability.

The study focuses on the effect due to heat transfer in predicting the in-

cylinder temperature. For such studies, not only are the fluid parameters, such as pressure and mass flows in the intake and exhaust, needed for validation, but also the thermal parameter needs to be the same. For this reason, temperature values at the exhaust port opening are the same. This was achieved by calibrating the correction coefficient of each correlation. Maintaining identical initial conditions in in-cylinder pressure and temperature have ensured that the trapped mass at the exhaust port opening will be the same. The information on similar thermal boundary conditions and trapped mass are provided in Figure 5.4.
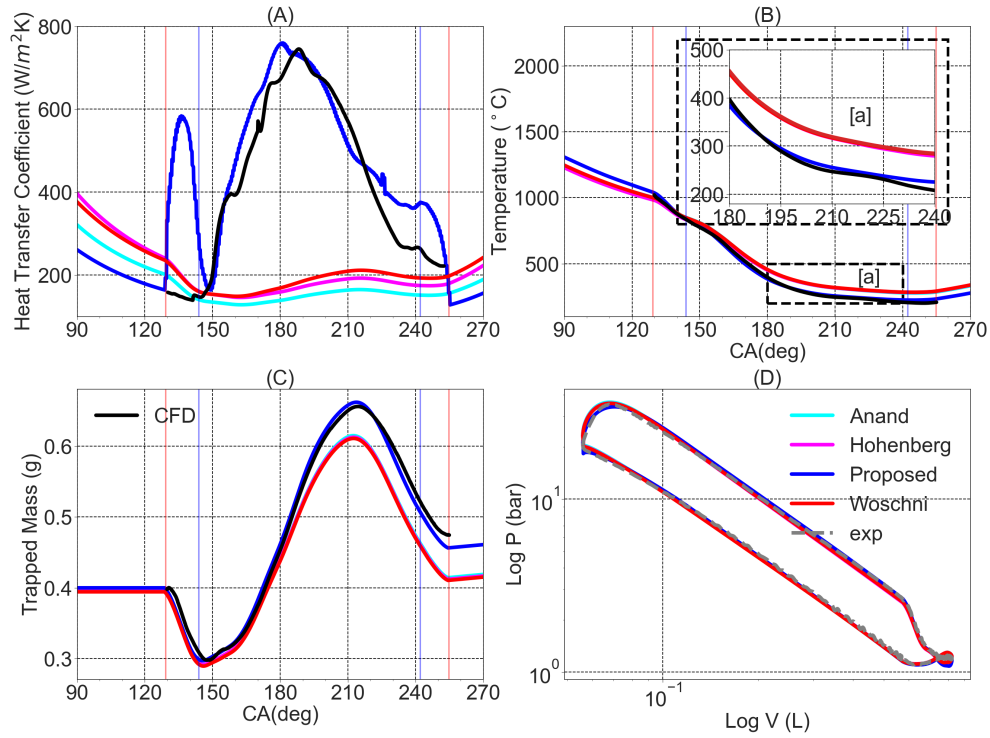
Figure 5.4: 1D model vs. CFD comparison of A. Heat transfer coefficient B. Temperature, C. In-cylinder trapped mass, D. Experimental vs. 1D simulation results in comparison for logarithm pressure Vs. Volume evolution.

Figure 5.4(A) provides information on the heat transfer coefficient used in this study during the scavenging process. Moreover, a solid black line depicting the instantaneous heat transfer coefficient from CFD simulation is depicted in

Figure 5.4(A). It can be seen from Figure 5.4(A) that methodology followed in developing the proposed heat transfer provide similar peaks and follows trends as in CFD simulations during scavenging. While on the other hand, the state-of-the-art heat transfer correlation fails to provide with necessary heat transfer coefficient during the same process. Figure 5.4(B) provides the information with temperature traces achieved due to the adjusted heat transfer coefficient. Figure 5.4(C) depicts the information on the trapped mass inside the cylinder during scavenging. Figure 5.4(B) and (C) shows CFD results plotted with a solid black line, showing the temperature and trapped mass, respectively, which are the same as in the 1D model at the exhaust ports opening. Figure 5.4(D) provides information related to the indicated diagram (in logarithm scales) evolution inside the combustion chamber for the 1D model and experimental data. Figure 5.4(D) results justify that the combustion settings used in the modeling stage provide accurate results. Observing the trends and patterns from Figure 5.3 and Figure 5.4, it can be justified that comparing different heat transfer models is viable as all models have similar behavior.

On observing the instantaneous temperature traces in the zoomed area 'a' in Figure 5.4(B), it can be seen that the classical heat transfer correlations based on the Reynolds number calculated with the mean piston speed predict higher temperature during scavenging compared to CFD results. Due to the lack of temperature predictability during scavenging, the state-of-the-art correlations also fail to reproduce the trapped mass in the cylinder while comparing results with CFD, as shown in Figure 5.4(C) when the exhaust ports close (around 255 CAD). On the other hand, the proposed heat transfer model developed considering the pseudo-velocity inside the cylinder accurately captures the temperature and trapped mass calculated by CFD. To quantify the results for trapped mass and temperature, readings for the same are captured at specific moments and presented in Table 5.2. The four instances are: at the exhaust port opening (130 CAD), intermediate positions (170 and 210 CAD), and finally, at the exhaust port closing (255 CAD). Moreover, since Anand, Hohenberg, and Woschnis heat transfer coefficient provide similar outputs, only results from Woschni are used for further comparisons. Using Equation 5.1 and Equation 5.2, differences in CFD and 1D modeling results are provided in Table 5.2 for in-cylinder trapped mass and temperature, respectively.

$$Error(\%) = \left(\frac{CFD - Model}{CFD}\right)100 \tag{5.1}$$

$$Error(°C) = CFD - Model \tag{5.2}$$

Table 5.2: Comparison of CFD Vs. 1D modeling results of different correlations at 130, 170, 210, and 255 CAD for in-cylinder mass and temperature.

Crank Angle	Trapped mass			Temperature		
	CFD	Proposed(%)	Woschni (%)	CFD	Proposed(°C)	Woschni(°C)
130	0.39	0.39 (0)	0.39 (0)	1015	1024 (-9)	1000 (15)
170	0.37	0.3 (-2.7)	0.36 (2.7)	519	511 (7)	564 (-46)
210	0.65	0.65 (0)	0.60 (7.69)	246	255 (-9)	319 (-73)
255	0.48	0.47 (2.08)	0.42 (12.5)	201	226 (-25)	285 (-84)

Since the initial conditions at the exhaust port opening for CFD and heat transfer models are very similar, no significant differences are found in either trapped mass or temperature. At 170 CAD, the proposed and Woschni heat transfer correlation shows a trapped mass of 0.38 and 0.36 g, respectively. These results are almost the same, as CFD simulations depict a trapped mass of 0.37 g. Contrarily, the temperature predictions using the Woschni correlation show an absolute deviation of $46°C$. This deviation in temperature is due lower convective heat transfer coefficient, which according to the calculation, provides 230 $\frac{W}{m^2 K}$.

On the other hand, the proposed heat transfer correlation calculation provides a convective coefficient of approximately 800 $\frac{W}{m^2 K}$. This coefficient value has led to a lower temperature prediction of $511.8°C$, which is $7°C$ lower than the CFD result of $519°C$. The lack of higher convective coefficients using the Woschni heat transfer correlation led to lower heat dissipation and increased fluid temperature inside the cylinder. These deviations in temperature prediction using the Woschni heat transfer coefficient are even higher at 210 and 255 CAD, where a deviation of $72.3°C$ and $84.4°C$, respectively, can be observed. Due to higher temperature predictions, lower trapped mass can be observed for Woschni heat transfer calculations. About 7% lower trapped mass can be observed at 210 CAD, while a 12.5% lower trapped mass can be seen at 255 CAD. All these deviations are attributed to a lack of proper heat transfer coefficients.

On the other hand, the temperature and trapped mass errors are lower using the proposed heat transfer model, which accounts for the high flow velocity inside the cylinder during the scavenging process and better approaches the

CFD results. Due to this, the fluid inside the cylinder is adequately cooled, and lower fluid temperatures are seen. The proposed heat transfer model predicts about $64°C$ lower temperature while comparing results with Woschni (at 210 CAD). This led to an accurate prediction of trapped mass at 210 CAD. Although at 255 CAD, CFD results depict about $201°C$, and the proposed model provides $25°C$ higher temperature but accurately predicts the trapped mass. Finally, observing trends in Figure 5.4 (B), (C), and Table 4, it can be said that the proposed heat transfer model accurately predicts the temperature and trapped mass by employing a higher convective coefficient compared to state-of-the-art models.

5.3.2   Performance assessment of heat transfer model

In this study, the heat transfer correlations (Woschni and proposed) are assessed under similar combustion settings to evaluate the potential of the proposed heat transfer model. To meet the objectives of the current study, the combustion duration is set to 45 CAD, and the start of combustion at 11 CAD before TDC. At the same time, maintaining a constant air-to-fuel ratio of 14.7. Along with the combustion parameters, the peak of the heat transfer coefficient during combustion (Woschni and Proposed) and scavenging in the proposed heat transfer model is set to the value of 2100 $\frac{W}{m^2 k}/$, as depicted in Figure 5.5 (A). This has been done by calibrating the coefficient b in Eq.16. Moreover, the engine speed and exhaust configuration are the same as in the previous study.
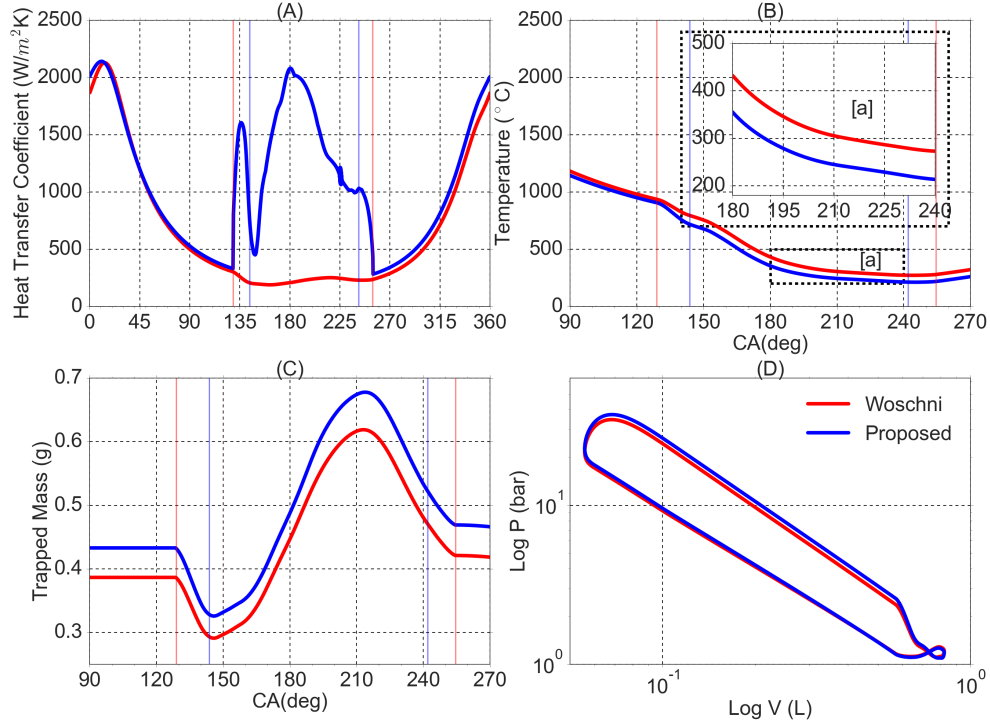
Figure 5.5: Results comparing Woschni and proposed heat transfer model for A. Heat transfer coefficient-1D model B. In-cylinder temperature evolution during scavenging, C. In-cylinder trapped mass, D. logarithm pressure Vs. Volume evolution.

As from the previous study, it is well established that a higher heat transfer coefficient leads to a lower in-cylinder fluid temperature. Similar results on lower fluid temperature using the proposed heat transfer coefficient over the Woschni correlation can be observed from Figure 5.5(B). This led to higher trapped mass using the proposed heat transfer model, as depicted in Figure 5.5(C). Two quantifiable results can be seen in this evaluation, one during scavenging, i.e., temperature profiles and their impact on the trapped mass, and the other is the effect on the combustion pressure due to higher trapped mass, which can be seen in Figure 5.5(D). Quantifying results during scavenging, the results on the instantaneous heat transfer coefficient during scavenging show that the Woschni heat transfer coefficient is as low as $200 \frac{W}{m^2 k}$ (data captured at 210 CAD). While for the same piston position, the proposed heat transfer model provides a peak coefficient of $2100 \frac{W}{m^2 k}$, leading to $80°C$ lower

in temperature, as depicted in the zoom area 'a' in Figure 5.5(B). Due to this lower fluid temperature, a peak trapped mass of 0.68 g can be seen using the proposed heat transfer correlation. On the other hand, the Woschni correlation depicts a peak trapped mass of 0.62 g, which is approximately 9% lower in trapped mass.

Due to the above phenomena, the trapped mass at the exhaust ports closing is higher in the proposed model. A trapped mass of 0.48 g using the proposed model can be seen, while the state-of-the-art model depicts 0.42 g. Due to this additional trapped mass and under similar AFR ratio and combustion settings, an increased pressure during combustion can be observed. To quantify the enhanced performance of the proposed model, the Indicated Mean Effect Pressure (IMEP) is used, given by:

$$IMEP = \frac{1}{V_d} \int pdV \tag{5.3}$$

Where V_d is the displacement volume of the cylinder, p is the pressure, and V is the volume of the cylinder. Using Equation 5.3, an IMEP of 3.49 and 3.92 bar can be observed for Woschni and the proposed heat transfer model, respectively. In other words, approximately a 12% difference in engine performance can be detected when using different heat transfer models.

5.3.3   Sensitivity analysis of heat transfer model

As mentioned earlier, the proposed heat transfer model uses a combination of Woschni heat transfer correlation during combustion and the proposed heat transfer during scavenging calculated using Equation 4.3 and Equation 4.11, respectively. Two constants are used to adjust the correlation coefficients, one to adjust the combustion (coefficient a in the Woschni equation) and the other for the proposed heat transfer coefficient (coefficient b). A sensitivity analysis is performed by varying the two coefficients to assess the impact on the trapped mass at the end of the scavenging process. Furthermore, in this analysis, the engine settings are maintained as in section 4.2. In this analysis, 35 points are studied, with values for coefficient b ranging from 2-6 and coefficient a ranging from 40-100. Figure 5.6 (A) provides information on the effect on trapped mass in absolute terms, while Figure 5.6 (B) depicts the information on the differences in trapped mass with variations in percentage in coefficients

a and b from the mean values. For this calculation, Eq.21 is used.

$$c_i = \left(\frac{v_i}{\overline{v} - 1}\right) 100 \tag{5.4}$$

Where v_i is the respective value of coefficient a, b or trapped mass and $\overline{v}$ is the mean value for coefficient a is 4, while the mean value for coefficient b is 70 and the mean value of trapped mass is approximately 0.455 g. From Figure 5.6, it can be observed that the effect of coefficient b has a higher impact on trapped mass over coefficient a.
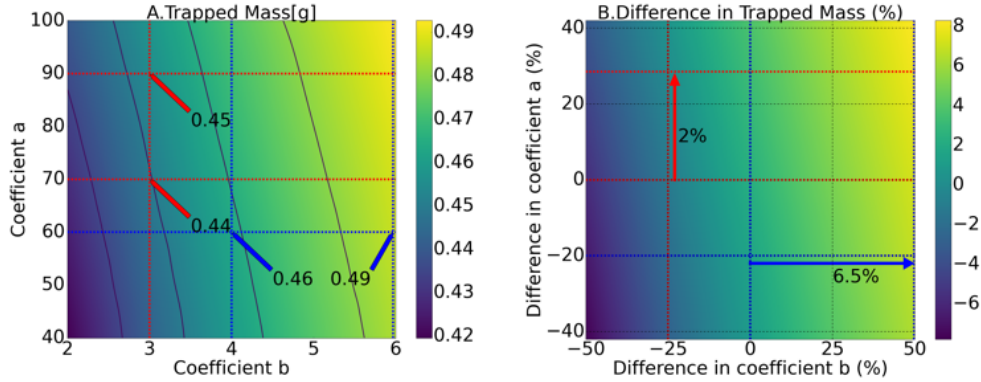

Figure 5.6: A. Effect on trapped mass varying coefficients a and b and B. Difference in trapped mass (%) varying differences in coefficients a and b (%).

For instance, from Figure 5.6 (A), considering a horizontal line at coefficient a of 60 (blue dotted line) and observing the trapped mass at coefficient b of 4 yields a value of 0.46 g. While for the same value of coefficients a and b of 6, it can be seen from Figure 5.6 (A) that the trapped mass has changed to 0.49 g. This change in trapped mass is about 6.5%, as observed in Figure 5.6 (B). On the other hand, from Figure 5.6 (A), for a constant value of coefficient b of 3 (red dotted line) and changing the coefficient a from 70 to 90 results in a trapped mass of 0.44 and 0.45 g, respectively. In other words, a change of 2% in trapped mass can be observed in Figure 5.6 (B). This analysis shows that the results in trapped mass are affected by the coefficient b chosen value, so special care has to be paid for when calibrating the model correlation.

5.3.4 Robustness of heat transfer model

While the previous sections deal with results at a constant engine speed of 2250 RPM, in this section, results for each tested engine speed, exhaust layout, and load conditions are depicted in Figure 5.7.
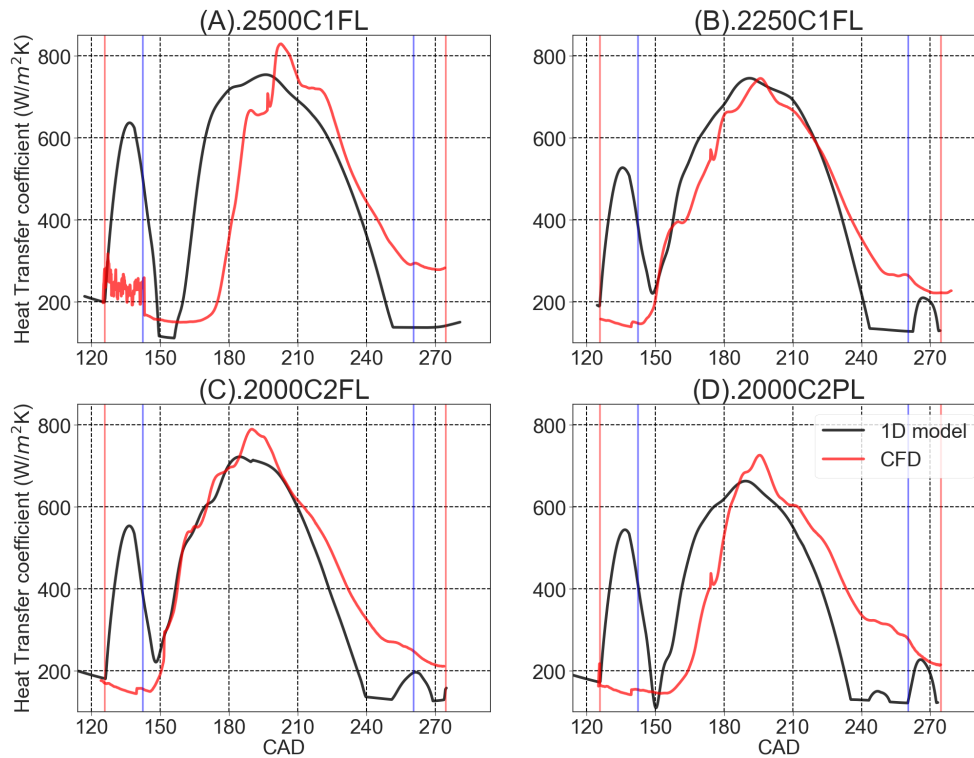

Figure 5.7: CFD to 1D Model comparison of heat transfer coefficient for A. 2500C1FL, B. 2250C1FL, C.2000C2FL and D. 2000C2PL

The results shown in Figure 5.7 show that the proposed model tends to over-predict the heat transfer coefficient for certain engine CADs. Although it is also true that the peaks and trends of the instantaneous heat transfer coefficients are very well captured by the 1D model, which is similar to CFD results. However, when considering the average heat transfer coefficient under respective operating conditions, as illustrated in Table 5.3, it can be justified that the 1D model yields a similar average heat transfer coefficient. Moreover,

upon observing the results presented in Figure 5.8 and Figure 5.9 , it can be substantiated that the proposed 1D heat transfer model accurately predicts the temperature profiles. Along with accurately capturing the trapped mass at the end of the scavenging process within the cylinder, justifying the higher heat transfer coefficient in the 1D model.

Table 5.3: Comparing of Average heat transfer coefficient between 1D and CFD $\frac{W}{m^2 K}$

Speed/Config/Load	1D model	CFD
2500C1FL	453.34	417.03
2250C1Fl	449.32	407.12
2000C2FL	401.07	429.14
2000C2Pl	358.54	342.49
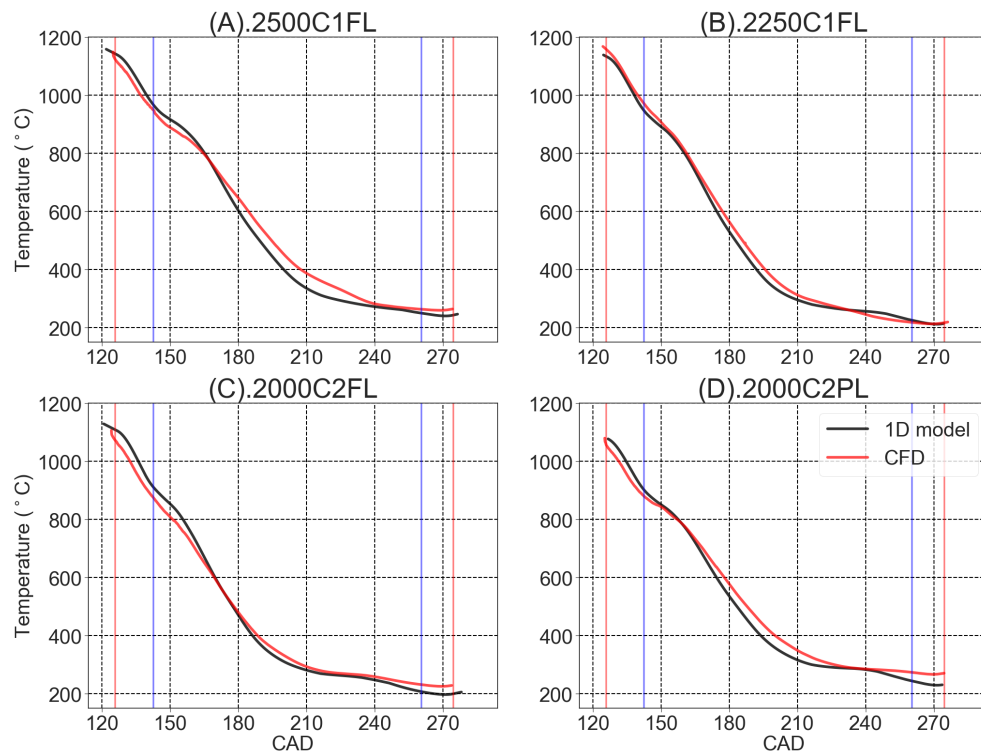
Figure 5.8: CFD to 1D Model comparison of temperature profile for A. 2500C1FL, B. 2250C1FL, C.2000C2FL and D. 2000C2PL
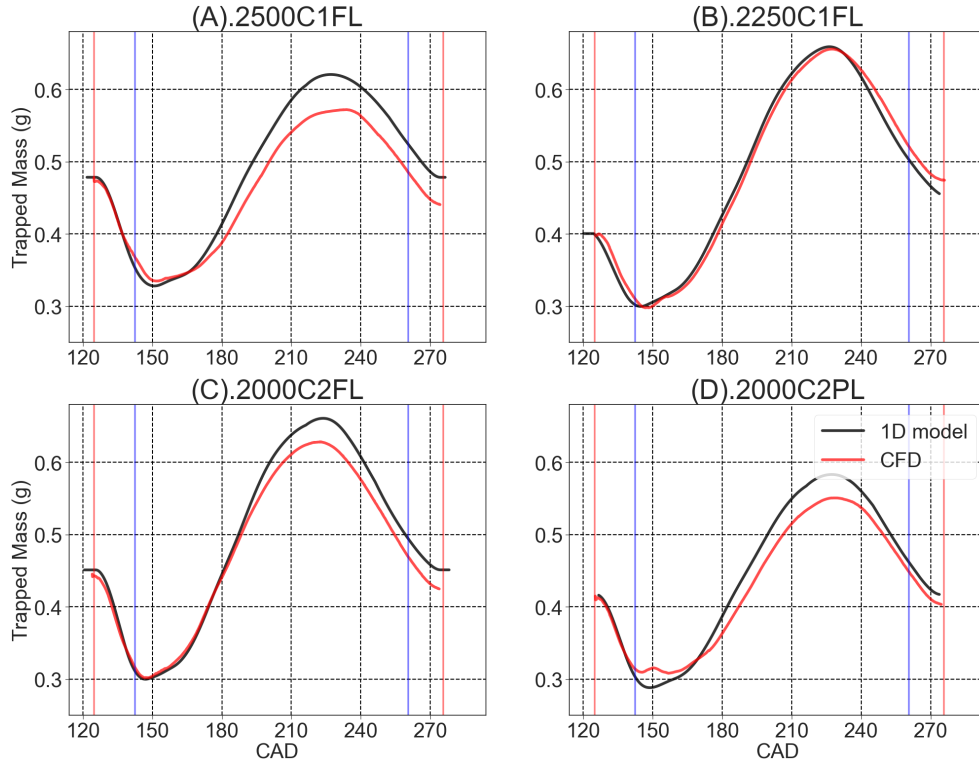
Figure 5.9: CFD to 1D Model comparison of trapped mass profile for A. 2500C1FL,
B. 2250C1FL, C.2000C2FL and D. 2000C2PL

5.4 Scavenging model

The results of the proposed synthetic scavenging curve are presented in this
section. Firstly, the calibration of the model is discussed, followed by the
presentation of gas dynamics and scavenging metrics for the extreme curves.

5.4.1 Scavenging model performance

As mentioned in section 4.3, a SS curve has been proposed. In this assess-
ment, all the experimentally tested conditions are studied. However, a de-
tailed explanation of the results obtained is only presented for the 2250C1FL

configuration as an example. Furthermore, for CFD simulations', initial and boundary conditions were maintained the same as studies performed in heat transfer assessment and the results are as shown in Figure 5.3 and Figure 5.4.

The results presented in Figure 5.10 show the CFD to the 1D model predictions. Figure 5.10A, shows the plot CBR vs. EBR obtained from CFD simulation and 1D SS model. It can be seen that the transition point from the PD condition occurs at 0.4 CBR condition and the anchor point at 0.3 CBR position. While doing such an assumption in 1D modeling yielded a perfect result in a short circuit of air that can be seen from Figure 5.10C. Figure 5.10B, shows the crank angle resolution of the phenomena in which the short circuit of air is observed. The solid line in Figure 5.10B shows the trends in the total gases leaving the cylinder. This includes both fresh charge and burnt gases. Observing the trends and peaks, it can be justified that both CFD and 1D results have coherency. On the other hand, the dashed line depicts the information on the exhaust gases exiting the combustion chamber. This excludes the short-circuiting of the air that occurs during the scavenging process. Two major phenomena can be observed, the starting point at which the short circuit occurs at around 190 CAD, as observed in Figure 5.10B. Secondly, the trend in short-circuiting where the 1D model accurately captures the 3D CFD gas dynamics phenomena. Thanks to the methodology followed yielded accurate results in capturing fluid dynamic effects while comparing results with CFD as seen in Figure 5.10D.
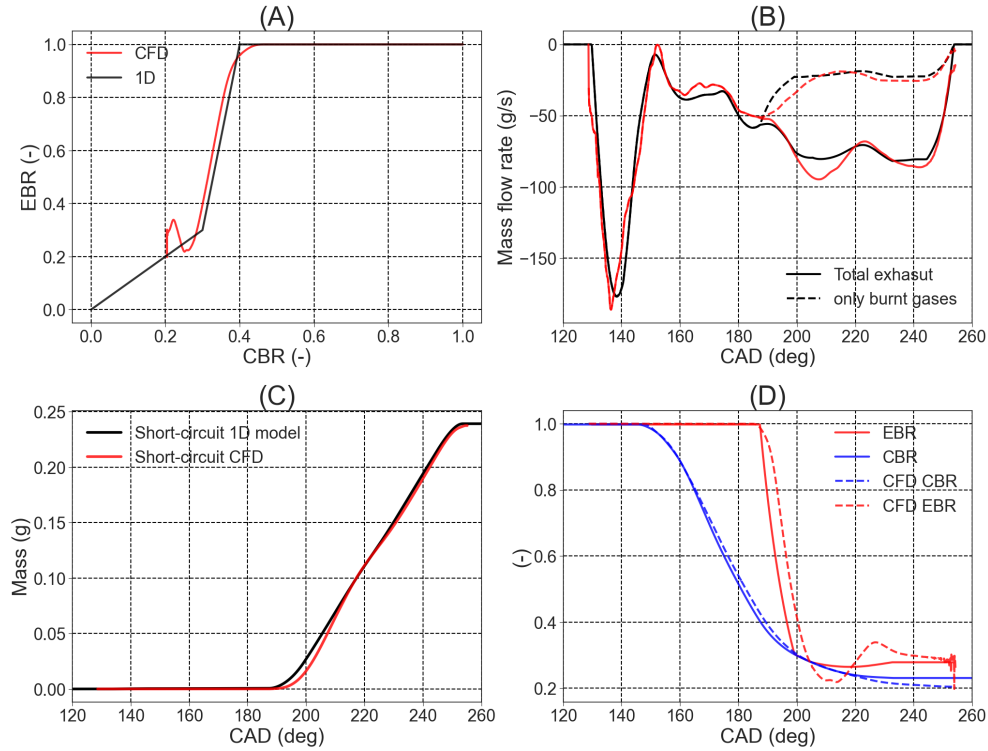
Figure 5.10: A. CFD to 1D comparison of CBR Vs. EBR, crank angle resolution comparison of CFD to 1D model B. Total Exhaust and burnt gases, C. Short circuit of air, and D. EBR and CBR

A similar procedure has been applied to analyze the results of short-circuiting of air for various engine speeds, exhaust configurations, and load conditions. The results are presented in Figure 5.11A-E, illustrating the corresponding SS curve for each operating condition. Additionally, Figure 5.11F-J compares the short circuit of air as predicted by the 1D model and the results obtained from the CFD simulations.

Upon examining the results presented in Figure 5.11, it can be concluded that despite the variations in engine speed and exhaust layout, the transition point remains consistent at a CBR value of 0.4 under full load conditions. However, in the case of partial load conditions, the transition point occurs later, approximately at a CBR position of 0.3, as shown in Figure 5.11 D. This difference in the transition point can be attributed to the lower engine

speed and lower mass flow. This led to a slower mixing of fresh charge and exhaust gases, lowering short-circuiting. The anchor point, on the other hand, depends on factors such as engine speed, exhaust layout, and load conditions. The calibration of the anchor point has been conducted to ensure comparable peaks in the short-circuiting of air.
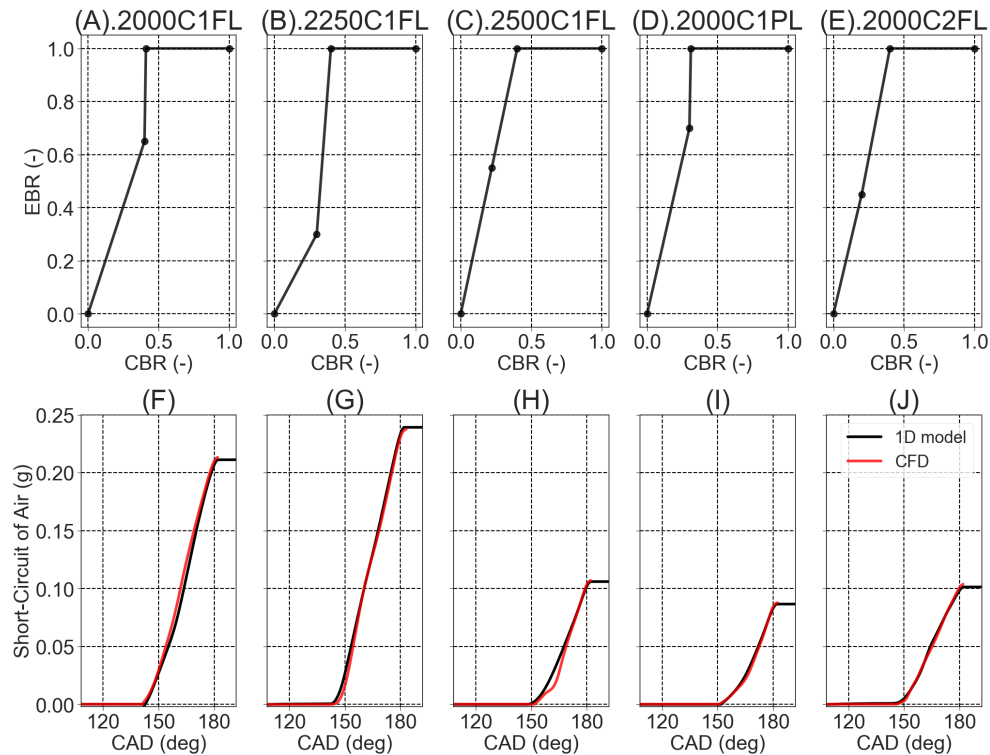

Figure 5.11: A-E. CBR Vs. EBR inputs for 1D model, F-J. Results comparisons of 1D model prediction to CFD results of Short circuit of air (g)

5.4.2 Gas Dynamic behavior under different exhaust layouts

In this assessment, results are compared at similar engine speeds, specifically at 2000 RPM, with consistent combustion, intake, and exhaust port settings. The only variation in this evaluation is the change in the exhaust configuration, and the gas dynamic assessment is presented in Figure 5.12. The A and B subplots in Figure 5.12 illustrate the pressure pulses inside the cylinder and

exhaust manifold, plotted with blue and black solid lines, respectively. In addition, the color green is used to represent forward pressure, indicating that the in-cylinder pressure is higher than the pressure in the exhaust manifold, while red represents reverse pressure. The exhaust mass flow rate as a result of the pressure difference inside the cylinder is depicted in Figure 5.12C. Trapped mass is visualized in Figure 5.12D, and the air and gas mass fractions are shown in E and F, respectively.
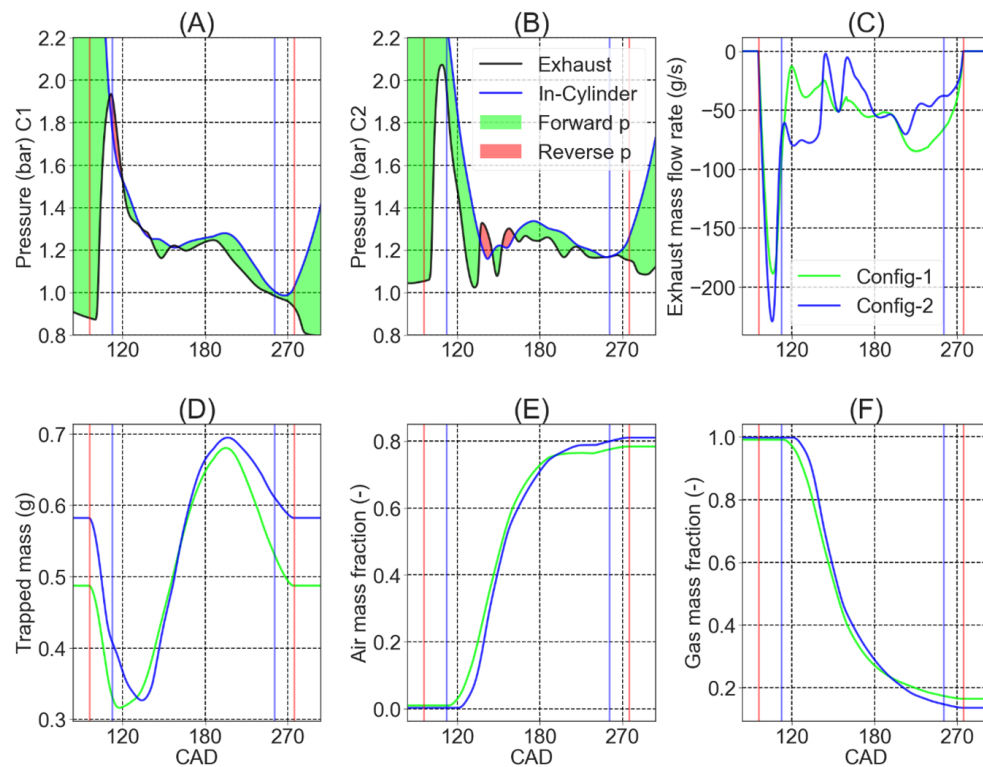

Figure 5.12: A. Pressure pulse in the exhaust manifold and in-cylinder for config-1, B. Pressure pulse in the exhaust manifold and in-cylinder for config-2, C. Exhaust mass flow rate, D. Trapped mass, E. Air mass fraction, F. Gas mass fraction.

Firstly, there are noticeable differences in the exhaust pulses when changing the exhaust configurations. In Figure 5.12A, it is evident that the opening of the exhaust ports leads to a forward pressure, resulting in higher exhaust mass flows in the exhaust manifold. Around 120 CAD, a reverse flow is observed in Figure 5.12A, as a consequence in Figure 5.12C (green solid line), with nearly

zero mass flow rate. Additionally, it can be observed that near the ports closing using exhaust config-1, significant forward pressures are present, facilitating the extraction of a maximum amount of gases from the combustion chamber. On the other hand, with exhaust config-2, there are variations in the pulses inside the cylinder and in the exhaust manifold, as shown in Figure 5.12B, initially, during the exhaust pulse down phase, where most of the exhaust gases are expelled from the cylinder, as depicted in Figure 5.12C (solid blue line). This can be attributed to the forward pressure pulse from Figure 5.12B. Subsequently, a segment (approximately at 140 CAD) where reverse pressure is observed, followed by a small pressure difference, can be seen close to ports closing, leading to lower mass flow rates in the exhaust manifold.

In addition to extracting lower exhaust mass flow near the ports closing and higher exhaust manifold pressure using config-2, a lower short-circuiting of air is observed with config-2 compared to config-1, as shown in Figure 5.11F and J. Due to the lower short-circuiting of air, a higher trapped mass is observed with config-2 exhaust architecture, as depicted in Figure 5.12D. Furthermore, there is a 2% increase in air mass fraction and a decrease in gas mass fraction at the end of the scavenging process, as shown in Figure 5.12E and F, respectively, can be seen. As a result of the higher trapped mass and under a similar air-fuel ratio (AFR) in both configurations, higher fuel injection is observed, leading to increased exhaust mass flows during the exhaust pulse down phase, as illustrated by the solid blue line in Figure 5.12C.

5.4.3 Sensitivity analysis of synthetic scavenging curve

In this evaluation, various engine speeds are examined to assess their corresponding engine performance and scavenging characteristics under an extreme SS curve. This analysis comprehensively studies the engines gas dynamics and scavenging efficiency. Initially, all SS curves for different configurations are plotted on the same graph and presented in Figure 5.13. Based on the observations from Figure 5.13, two distinct conditions are identified: one condition that closely resembles the PD condition, represented by solid red circles, and another condition resembling the PM condition, indicated by solid grey squares. These conditions are labeled as extreme conditions (ExC) -1 and -2, respectively. Moreover, the combustion settings, friction, and heat transfer multipliers for the intake and exhaust manifold were the same.
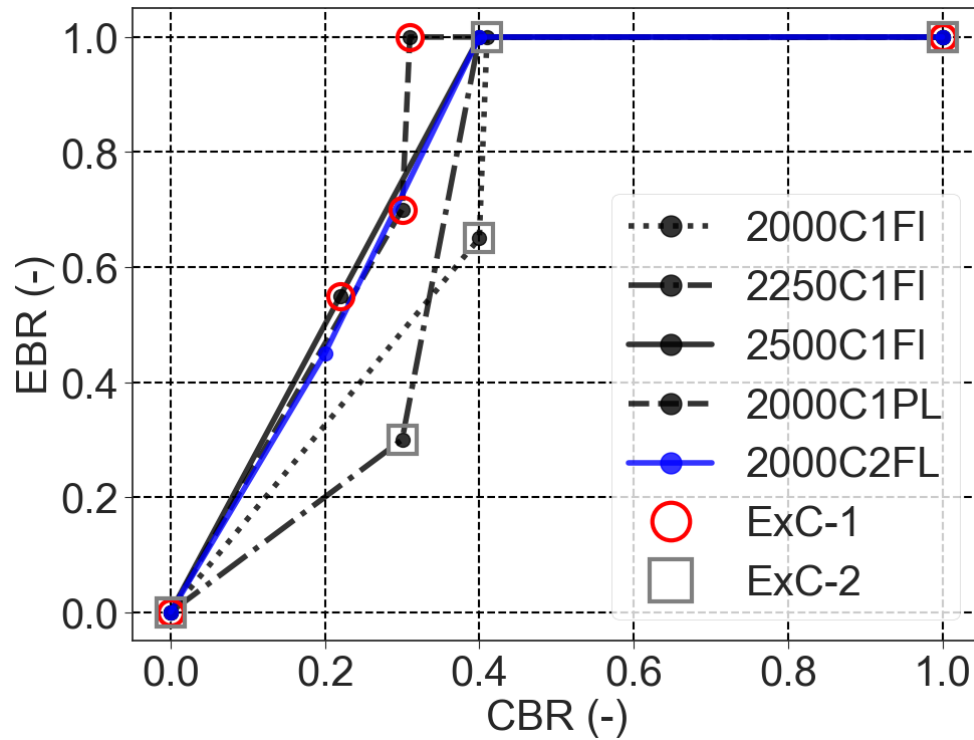
Figure 5.13: CBR Vs. EBR for all engine running conditions, along with a depiction of Extreme SS operating points

Gas dynamic analysis of the engine, including in-cylinder trapped mass, air mass fraction, gas mass fraction, and short-circuit of air, is presented in Figure 5.14 for each engine speed under the ExC conditions. The data captured at the exhaust port closing is depicted in Figure 5.14 for all engine speeds. Two notable observations from Figure 5.14 can be made. Firstly, it allows for a comparison of the impact of the SS curve under the two extreme conditions. Secondly, it demonstrates the influence of engine speed on gas dynamics.

When comparing the data under ExC conditions, ExC1 (closer to the PD condition) is represented by solid red color. In contrast, ExC2 (closer to the PM condition) is depicted using solid blue color in Figure 5.14. As ExC1 closely resembles the PD condition for all three engine speeds, it exhibits lower short-circuiting of air compared to ExC2, as observed in Figure 5.14D. At 2000 RPM with the ExC2 SS curve setting, a peak short-circuiting of air of

0.26 g is observed, whereas under the same engine operating conditions with the ExC1 SS curve, a peak of 0.18 g in air short-circuiting can be seen. The lower short-circuiting in the ExC1 SS curve setting results in a higher trapped mass, as shown in Figure 5.14A. Comparing the air and gas mass fractions, the ExC1 configuration shows higher air trapping and lower gas trapping inside the cylinder. This superior performance of ExC1 over ExC2 is attributed to the delayed transition from the PD to PM condition, as seen in Figure 5.14D. In the ExC1 condition, the transition occurs at the 0.3 CBR position, resulting in less mixing of gases and greater air retention. In contrast, the ExC2 curve exhibits an earlier transition point at the 0.4 CBR position, leading to earlier mixing of air and gases and a higher short-circuiting effect.

Additionally, Figure 5.14A shows that the trapped mass increases with engine frequency while the short-circuiting of air decreases, as evident in Figure 5.14D. However, Figure 5.14B indicates that the air mass fraction decreases at higher engine RPMs. Furthermore, Figure 5.14C illustrates a higher gas mass fraction trapped inside the cylinder. For example, at 2500 RPM with ExC1, a trapped mass of 0.54 g is observed, while for the same ExC condition, a trapped mass of 0.52 g can be seen at 2000 RPM. However, the air mass fraction is 0.84 and 0.82 for 2000 and 2500 RPM, respectively. The gas mass fraction is 0.10 and 0.14, as shown in Figure 5.14C. These differences can be attributed to the engine speed, as faster piston movement leads to quicker port closing, resulting in slower gas exchange to the atmosphere via the exhaust manifold. Therefore, higher air mass fractions are observed at lower engine speeds, where gas exchange is more efficient.
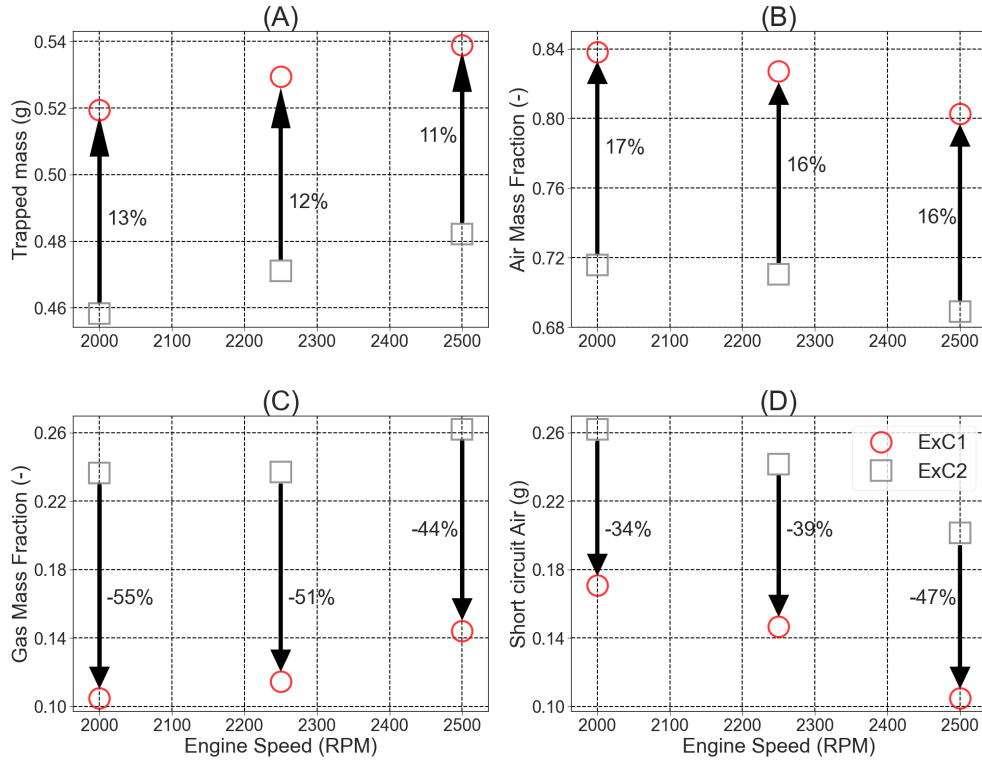
Figure 5.14: Gas dynamic analysis of Extreme SS curve, A. Trapped mass, B. Air mass fraction, C. Gas mass fraction, D. short-Circuit of air

To further quantify the results observed in Figure 5.14, the scavenging assessment utilizing SE, TE, CE, and DR is presented for each running condition under both ExC conditions in Figure 5.15. This assessment provides instantaneous information on scavenging metrics. In the plot, solid lines represent data related to the ExC1 condition, while dashed lines depict the ExC2 operating curve. The colors red, blue, and black correspond to engine running conditions at 2000 RPM, 2250 RPM, and 2500 RPM, respectively. As previously mentioned, the ExC2 SS curve exhibits an early short-circuiting of air, and the crank angle for the start of the short circuit varies with engine speed. For example, based on the results in Figure 5.15D, the start of the short circuit occurs at approximately 185 CAD position for 2000 RPM with the ExC2 characteristic curve, while for the same curve at 2500 RPM, the air short-circuiting initiates around 192 crank angle position. Conversely, when

using the ExC1 SS curve at 2500 RPM, the start of air short-circuiting is observed at 215 CAD position due to the delayed transition from PD to PM condition in the ExC1 operating curve.
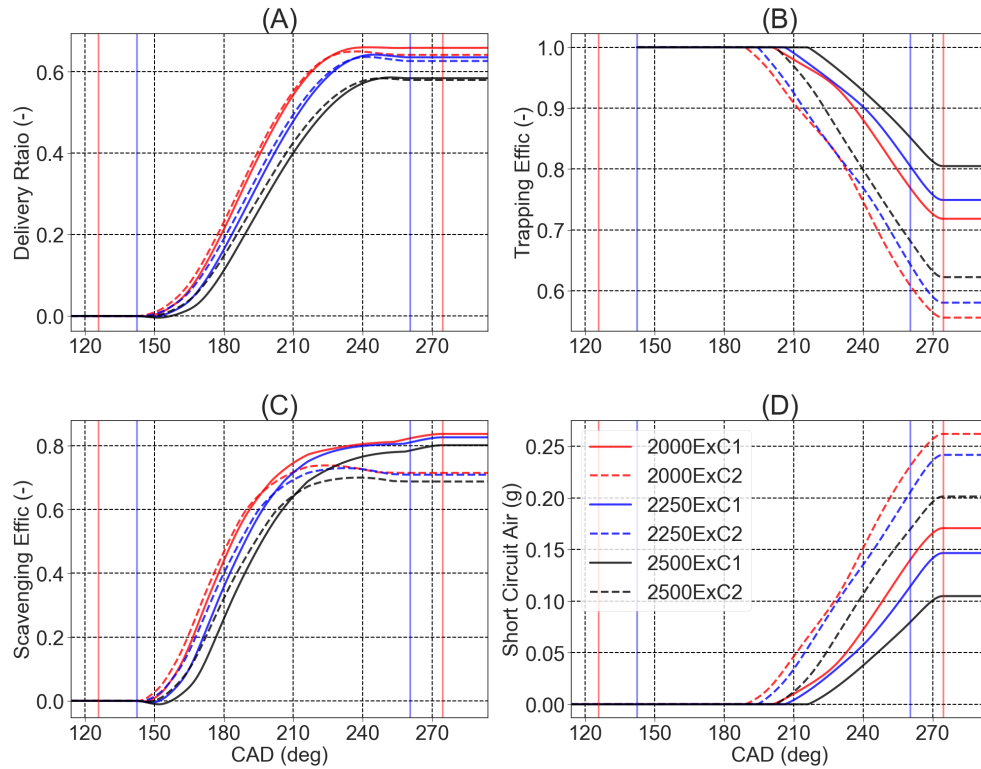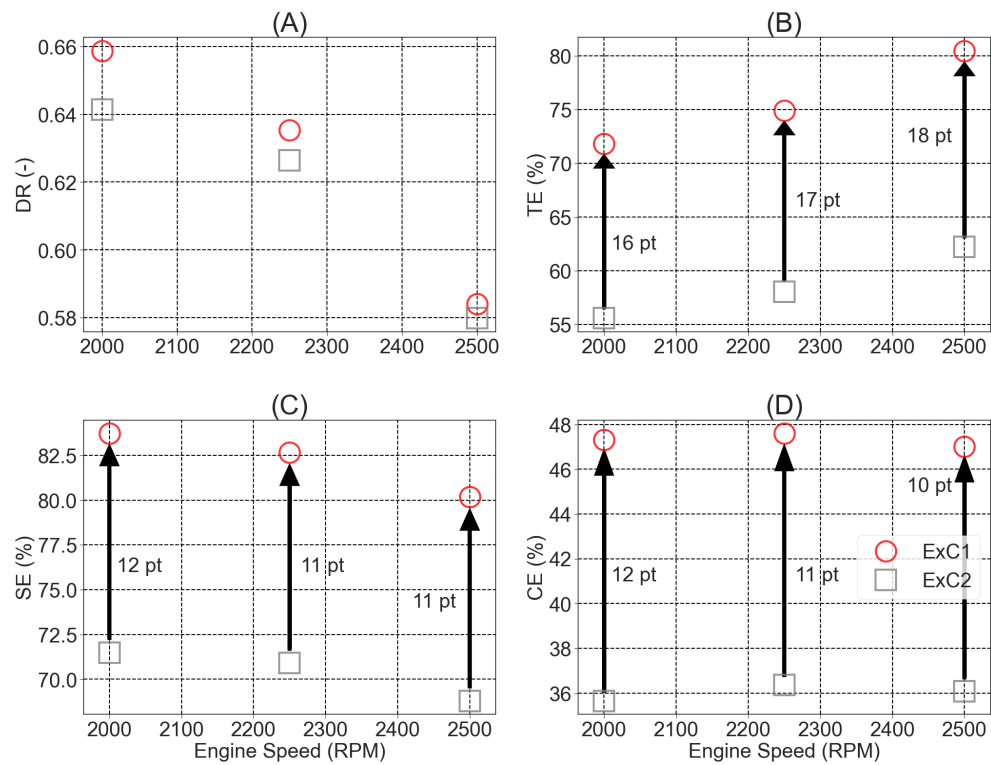

Figure 5.15: Assessment of scavenging metric, A. Delivery ratio, B. Trapping Efficiency, C. Scavenging Efficiency, D. Integral of short-circuit of air

During the assessment of scavenging metrics in Figure 5.15A, it is evident that the ExC SS curves have a negligible impact on the delivery ratio. However, consistent charging efficiencies of 0.47 for ExC1 and 0.36 for ExC2 were calculated, and these values remained constant across different engine speeds. This is because these scavenging metrics are determined based on the reference mass flow rate. Nevertheless, the SS ExC characteristic curve and the engine speed influence the scavenging and TE.

In Figure 5.15B, it is evident that a peak trapping efficiency (TE) of 0.805 (captured at the exhaust port closing) is observed at 2500 RPM. Similarly,

at 2000 RPM with the ExC1 configuration, a TE of 0.72 is observed, which
is higher than the TE at 2500 RPM with the ExC2 SS curve, where a peak
TE of 0.62 is observed. Furthermore, Figure 5.15C provides two significant
observations. Firstly, ExC1 exhibits higher scavenging efficiency (SE) com-
pared to ExC2, consistent with the earlier findings. Secondly, as the engine
speed increases, SE decreases. This can be attributed to the reduced duration
for gas dynamics exchange between the in-cylinder and exhaust as the engine
speed increases. In absolute terms, the same can be observed from Figure 5.16
with a change relative to the ExC2 condition.

Figure 5.16: Assessment of scavenging metric absolute, A. Delivery ratio, B.
Trapping Efficiency, C. Scavenging Efficiency, D. Charging Efficiency

5.4.4   Thermo-fluid dynamic assessment of extreme conditions

As observed from Figure 5.16A, despite having similar discharge coefficients for intake and exhaust ports, there is a marginal change in the DR. To understand the marginal change, thermofluid dynamic assessment is presented in Figure 5.17 at 2000 RPM.
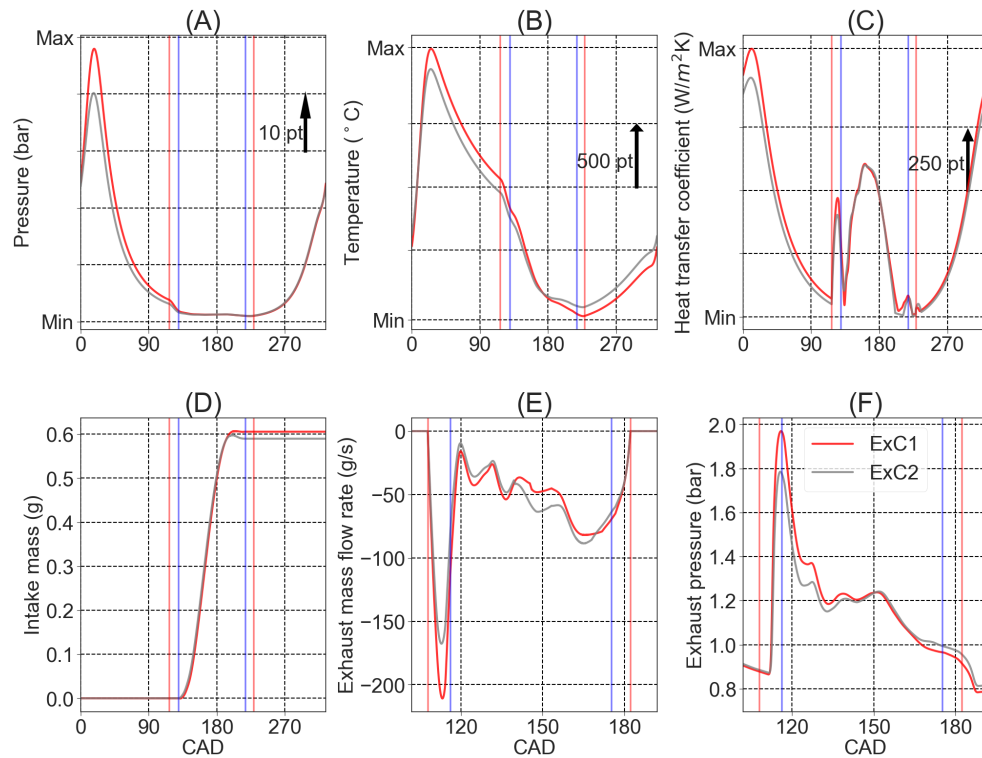

Figure 5.17: A. In-cylinder pressure, B. In-cylinder temperature, C. In-cylinder heat transfer coefficient, D. Intake mass, E. Exhaust mass flow rate, F. Exhaust pressure.

    Observing the results from Figure 5.14A, at 2000 RPM, the trapped mass has increased by 13% while changing from ExC1 to ExC2 SS curve. Due to elevated trapped mass and under similar AFR, 8 points higher combustion pressures can be seen using ExC1 SS curve from Figure 5.17A. Due to higher pressure during combustion, increased in-cylinder temperature and heat transfer coefficient can be observed from Figure 5.17B and C at approximately

30 CAD. Due to this phenomenon, during exhaust port opening, higher exhaust mass flow and increased exhaust manifold pressure can be seen from Figure 5.17 E and F, respectively.

Secondly, it can be seen from Figure 5.17C that despite having similar trends in instantaneous heat transfer coefficient during the scavenging process, the cylinder is further cooled down while operating with ExC1 SS curve Figure 5.17B (solid red line). This can be attributed to the lower short-circuiting of air when operating by ExC1 SS curve that can be seen from Figure 5.14D, by 34%. Along with increased trapping and scavenging efficiencies by 16 and 12 points, respectively, observed from Figure 5.16B and C, hotter exhaust gases are pushed out of the cylinder, and the cooler fresh charge is trapped inside the cylinder. This aided in further cooling down of the cylinder while using ExC1 SS characteristic curve. A cooler cylinder will allow for a higher fresh charge into the cylinder, which can be seen in Figure 5.17D (solid red line), where an improvement of 6% in intake mass can be seen. This has been attributed to the increased DR that can be seen in Figure 5.16A.

Chapter 5 references

[3]   H. Climent, A. Tiseira, J. Gomez-Soriano, and A. Darbhamalla. "In-Cylinder Heat Transfer Model Proposal Compatible with 1D Simulations in Uniflow Scavenged Engines". *Applied Sciences* 13 (6 Mar. 2023), p. 3996. ISSN: 2076-3417. DOI: 10.3390/app13063996 (cit. on pp. xvii, 74).

Chapter 6

Conclusions and future works

Contents

6.1   Summary and conclusions

Aiming for sustainable mobility, regulatory norms are periodically defined to control emissions from automobiles. The new emission norm Euro-7 has called for the adoption of new technology battery-driven vehicles. However, due to limited resources in electricity production and significant distribution losses, the range extender concept is being investigated to support these vehicles. Typically, these range extenders are two-stroke engines. To further reduce the space occupied by these engines, new engine concepts are being studied. These advanced two-stroke engines have fewer moving parts, resulting in reduced frictional and mechanical losses. Additionally, emissions from these engines are lower compared to conventional engine concepts due to their limited range of operating conditions. However, these engine concepts are still in their early stages of development, and their performance can be further improved. To certify such engine concepts across multiple operating points, a robust model is required.

Based on the above considerations, two main objectives are defined in this thesis work. Firstly, to develop an engine model for analyzing engine performance, and secondly, to obtain thermodynamic results inside the cylinder. To achieve these objectives, a uniflow scavenged two-stroke direct injection gasoline engine is tested. The test results are then used to validate and calibrate the 1D model, which is subsequently used to assess fluid dynamics phenomena in the intake and exhaust lines, as well as combustion settings inside the cylinder. Upon observing potential fluid dynamic responses, these results are utilized as initial and boundary conditions for CFD simulations to evaluate thermal metrics inside the cylinder. A comparison between the CFD results and the 1D data reveals that the existing state-of-the-art heat transfer model fails to accurately capture temperature profiles inside the cylinder, and the theoretical scavenging model fails to represent the short-circuiting of air. These limitations result in an unstable model for capturing in-cylinder performance. As a result, a new heat transfer coefficient and a synthetic scavenging curve are proposed to accurately capture the gas dynamics during the scavenging process.

The conclusions drawn from the aforementioned studies are presented in the following subsections: (6.1.1) Overall conclusions, (6.1.2) Compatibility of the heat transfer model, and (6.1.3) Compatibility of the scavenging model.

6.1.1   Overall conclusions

In the present thesis, the tested engine is a 0.76L uniflow scavenged two-stroke, direct ignition engine. In the experimental campaign, three speeds (2000, 2250, and 2500 RPM), with two exhaust layouts (Config-1 and Config-2) and load conditions (FL and PL), are performed. To overcome the combustion instabilities, data from 100 consecutive cycles is captured. The data is post-processed, and the engine performing with the most recurring cycle is selected. The post-processed data is then used for model validation.

VEMOD software is used in developing the novel engine in a 1D fashion. The software groups elements as 0D or 1D elements depending on the spatial dimensions. Pipes, bends, and nodes are used to model the intake and exhaust lines, and the same strategy is employed to model the intake rod. The heat transfer and frictional multipliers inside the pipes were calibrated to attain similar trends as observed in the data captured through experiments tests conducted. To model the intake and exhaust port discharge coefficients of a constant discharge valve is calibrated with respect to piston position to attain similar averaged mass flow rates as in the experimental campaign. Similar injection settings were employed in the injector to mimic experimental averaged fuel injection. The combustion chamber is modeled as a 0D element, and the 1D Euler equations for unsteady compressible non-homentropic flow ensured the gas dynamics inside the engine.

To study the in-cylinder gas dynamics beyond the experimental and 1D model, CFD simulations are employed. Commercial CFD software is employed to study CFD results. A geometrical 3D engine model of the tested engine is developed and used in this assessment. Several aspects in setting up the CFD model were adapted, including the mesh details, numerical schemes, heat transfer, and turbulence model. This study focused on the gas exchange during scavenging. Therefore, the simulation was initiated just before the exhaust ports opened and lasted till the exhaust port was closed. During this simulation run time, both the heat transfer and gas dynamic, including short-circuit of air, are captured and studied.

Firstly, experimental data is used to validate the 1D model. In this validation, information on the combustion pressure is used to validate the combustion and injection settings. Furthermore, pressure in the exhaust manifolds validates the frictional and heat transfer multipliers used in developing the

exhaust manifold. Also, in-cylinder pressure pulse data during scavenging validated the gas dynamic exchange and modeling of the cylinder in 0D mode. Moreover, IMEP calculations are also presented for the tested engine speed and configurations depicting the fluid dynamic properties of the model. These model outputs are used as boundary and initial conditions for the CFD simulation at respective speeds, exhaust layouts, and load conditions to validate thermal effects.

After observing variations in the temperature profile and the subsequent impact on trapped mass resulting from the inadequate heat transfer coefficient provided by the state-of-the-art models during scavenging, a new heat transfer model was proposed. The robustness of the proposed heat transfer and its impact on engine performance is depicted in subsection 6.1.2. Moreover, observing differences in short-circuit of air during scavenging using theoretical scavenging curves and a new scavenging characteristic curve is proposed. The potentiality of the proposed curve is concluded in subsection 6.1.3.

6.1.2 Compatibility of the heat transfer model

In this study, the following are concluded with observations made at 2250RPM, config-1, and full load operating condition:

- Under identical initial conditions for all the heat transfer correlations, it is observed that the state of art correlations, which include Anand, Hohenberg, and Woschni heat transfer correlations, provide similar results during scavenging. The heat transfer coefficient during scavenging can be as low as 200 $W/(m^2K)$, leading to a peak deviation of 85 °C in temperature predictions and up to 12% in deviation for trapped mass predictions are observed. On the other hand, the proposed heat transfer model calculates a peak coefficient of 800 $W/(m^2K)$ during scavenging, leading to a peak temperature deviation of 25 °C along with almost negligible error in trapped mass predictions.

- Under identical combustion settings and similar peak heat transfer coefficient, a difference in trapped mass of up to 6% at the exhaust port closing has been observed using the proposed heat transfer model, while comparing results with Woschni heat transfer coefficient. The gases inside the cylinder are cooled a further 85 °C, leading to a higher trapped

mass. This is translated to differences up to 12% in the IMEP of the engine.

- A sensitivity analysis was performed to evaluate the impact of the model constants on the engine operation. These constants include both Woschni and the proposed heat transfer correlation during scavenging. In this analysis, coefficient b (correction coefficient of proposed heat transfer correlation) is changed by ±50% from the mean value, and coefficient a (correction coefficient of Woschni heat transfer correlation) is changed by ±42%. Results depicted that coefficient b had a more significant impact on trapped mass. A sweep along varying coefficient b and at constant coefficient a can lead to a 15% change in trapped mass. Conversely, a sweep along varying coefficient a and at constant coefficient b can lead to a maximum difference of 5% in trapped mass.

In addition to the observation made above related to the model predictions in heat transfer, temperature, and trapped mass profiles at 2250 RPM config-1-FL, conclusions on the heat transfer profiles made at remaining engine configurations are depicted below:

- Observing the instantaneous heat transfer coefficients profiles at respective engine running conditions, it can be seen that the 1D model over-predicts the heat transfer coefficients at certain CAD while comparing results with CFD simulations. This is due to the fact that the proposed model uses instantaneous mass flow rates at the intake and exhaust manifold. Despite this consideration, it can also be seen that the temperature profile remained unaffected.

- From the same observation, it can also be noted that the average heat transfer coefficient during the scavenging cycle is over-predicted by the 1D model, with an absolute maximum deviation of 10%.

6.1.3 Compatibility of the scavenging model

To accurately capture the short-circuiting of air, a synthetic scavenging (SS) model is proposed. The SS curve consists of four characteristic points: the initial point, transition point, anchor point, and target point. The calibrated

SS curve is studied to accurately capture the start and peak of the short-circuiting of air. The transition point indicates the start of the short-circuiting, while the anchor point is calibrated to achieve the peaks of short-circuiting, which is influenced by engine speed, load condition, and exhaust configuration. For example, at 2000 RPM with similar combustion, port settings, and load conditions, using config-1 exhaust layout results in a peak short-circuiting of air of 0.22g, while config-2 exhaust layout provides 0.10g of short-circuiting is observed.

The impact of the exhaust manifold layout on the gas behavior inside the cylinder is analyzed, focusing on pressure pulses observed inside the cylinder and exhaust manifold, as well as the mass flow rate in the exhaust. With config-1, higher forward pressure near the exhaust port closing leads to greater gas extraction at the end of the scavenging process is seen. Conversely, with config-2, higher exhaust gases are extracted during the port opening phase, where exhaust gases and fresh charge are not perfectly mixed. This results in lower short-circuiting of air aided by higher exhaust pressure. The lower short-circuiting of air, along with higher trapped mass and constant air-fuel ratio, led to a 19% increase in IMEP.

A sensitivity analysis is conducted by analyzing all the calibrated SS curves and selecting extreme operating conditions (ExC1 and ExC2). Results depict that trapped mass is enhanced by an average of 12% when changing from ExC2 to ExC1. Throughout the operating conditions, an average of 16% change in air mass fraction, 49% reduction in gas mass fraction, and 35% reduction in air short-circuiting are observed. This results in an average increase of 16 points in scavenging efficiency, 11 points in trapping efficiency, and 11 points in charging efficiency.

Furthermore, it is observed that changing the SS characteristic curve impacts the delivery ratio (DR) despite maintaining similar discharge coefficients in both ExC conditions. A thermo-fluid dynamic assessment is presented at 2000 RPM engine speed, demonstrating that SE and TE are enhanced by 16 points and 12 points, respectively, when changing from ExC2 to ExC1, thus pushing the exhaust gases out of the cylinder and retaining higher fresh charge inside the cylinder. This leads to further cooling of the cylinder despite similar heat transfer during scavenging and improves the peak intake mass by 6%, resulting in a marginal change in DR.

Therefore, from the above, it can be concluded that for a well-calibrated

heat transfer and scavenging model, thermofluid dynamically stable results can be achieved.

6.2 Future works

Although there are a series of models developed in this thesis work to achieve a thermo-fluid dynamically stable model, there are certain limitations/ additional works that can be performed. Firstly, the 1D engine model is validated on some engine tests, and over the validated model, some potential strategies are proposed. These proposed models are investigated only with simulations. Secondly, it must be noted that the conclusion presented in section 6.1 was drawn from engine tests and simulations under some specific steady-state points. These limitations open the doors for the following future works:

- Since this engine operates using gasoline direct ignition which limits homogeneous mixture formation leads to NO_x formation, which can be studied experimentally. Not only NO_x, but also HC formation during short circuiting, CO formation for different air-to-fuel ratio can also be studied, for different engine speeds and exhaust systems.

- Although it is true that these types of advanced two-stroke engines are used as range extenders and need not work in transient running conditions but can be used in transient situations when there is a surge in energy requirements.

- Evaluate the fuel consumption rate and emission formation and optimize the engine over a wide range of operating conditions.

- Increase the range of operation beyond tested engine speeds to reduce mechanical losses. To achieve the particular objectives of this study, models must be developed.

- Knock is another aspect that would limit the functionality of such engines at higher engine speeds. Therefore, it is important to understand the COV at higher engine speeds and the engine performance.

Additionally, by bringing in some design changes to the existing engine layout, the range and functionality of such engines can be increased and improved.

- Analyse the effects on engine performance and knock with change in stroke length and bore diameter.

- By adding another combustion along with a single piston moving the whole stroke length in both the combustion chamber can provide a higher density of power output for faster charging.

- Eliminating the crankshaft and replacing it with a linear generator can provide additional space to have extra battery placement. This would allow for a variable compression ratio, and futuristic fuels can be used over conventional fuels such as gasoline or LPG.

Global references

[1] J. R. Serrano, H. Climent, P. Piqueras, and A. Darbhamalla. "Energy recovery potential by replacing the exhaust gases recirculation valve with an additional turbocharger in a heavy-duty engine". *Energy Conversion and Management* 271 (Nov. 2022), p. 116307. ISSN: 01968904. DOI: 10.1016/j.enconman.2022.116307 (cit. on pp. xvii, 10).

[2] J. R. Serrano, H. Climent, A. Gomez-Vilanova, A. Darbhamalla, and S. Guilain. "Assessment of Variable Geometry Orifice Compressor Technology Impact in a New Generation of Compression Ignition Powertrains at Low-End and Transient Operation". *Applied Sciences* 12 (24 Dec. 2022), p. 12869. ISSN: 2076-3417. DOI: 10.3390/app122412869 (cit. on pp. xvii, 9).

[3] H. Climent, A. Tiseira, J. Gomez-Soriano, and A. Darbhamalla. "In-Cylinder Heat Transfer Model Proposal Compatible with 1D Simulations in Uniflow Scavenged Engines". *Applied Sciences* 13 (6 Mar. 2023), p. 3996. ISSN: 2076-3417. DOI: 10.3390/app13063996 (cit. on pp. xvii, 74).

[4] S. Schlacke, H. Wentzien, E.-M. Thierjung, and M. Köster. "Implementing the EU Climate Law via the 'Fit for 55' package". *Oxford Open Energy* 1 (Jan. 2022). ISSN: 2752-5082. DOI: 10.1093/ooenergy/oiab002 (cit. on p. 2).

[5] M. Langkamp and V. Bayma. "Evaluation of the Directive 2008/50/EC on Ambient Air Quality". *Science for Sustainability Journal* 3 (Jan. 2019). DOI: 10.53466/VERI6053.S4SLAB (cit. on p. 2).

[6] M. Iriti, P. Piscitelli, E. Missoni, and A. Miani. *Air pollution and health: the need for a medical reading of environmental monitoring data.* 2020 (cit. on p. 2).

[7] D. Bart, P. Enrico, P. Emanuela, D. M. Alexander, M.-F. Fabio, B. Katalin, M. Alessandro, A.-L. Maria, T. Philippe, and V. Elisabetta. "Urban NO2 Atlas" (2019) (cit. on p. 2).

[8] Z. Zhongming, L. Linong, Y. Xiaona, L. Wei, et al. "Emissions of most harmful air pollutants dropped in 2018, marking EU progress under UN Convention" (2020) (cit. on p. 2).

[9] J. Cross and J. Bølstad. "Openness and censorship in the European Union: An interrupted time series analysis". *European Union Politics* 16 (May 2014), pp. 216–240. DOI: 10.1177/1465116514560066 (cit. on p. 2).

[10] R. Čižinská and J. Chládková. "Selected Impacts of Regulation (EU) 2019/631 On Value Creation in the Automative Industry". *Financial Internet Quarterly* 17 (Sept. 2021), pp. 76–87. DOI: 10.2478/fiqf-2021-0022 (cit. on p. 3).

[11] K. Gkoumas, F. Marques dos Santos, M. Stępniak, and F. Pekár. "Research and Innovation Supporting the European Sustainable and Smart Mobility Strategy: A Technology Perspective from Recent European Union Projects". *Applied Sciences* 11 (Dec. 2021), p. 11981. DOI: 10.3390/app112411981 (cit. on p. 3).

[12] N. Sadeleer. "Environmental Law in the EU: A Pathway Toward the Green Transition". In: Mar. 2023, pp. 21–33. ISBN: 978-3-031-24887-0. DOI: 10.1007/978-3-031-24888-7_2 (cit. on p. 3).

[13] M. Amiryar and K. Pullen. "A Review of Flywheel Energy Storage System Technologies and Their Applications". *Applied Sciences* 7 (3 Mar. 2017), p. 286. ISSN: 2076-3417. DOI: 10.3390/app7030286 (cit. on p. 3).

[14] S. Y. Khan. "A comparative study and analysis of PHES and UGPHES systems." PhD thesis. 2015 (cit. on p. 3).

[15] A. Allagui, A. S. Elwakil, M. E. Fouda, and A. G. Radwan. "Capacitive behavior and stored energy in supercapacitors at power line frequencies". *Journal of Power Sources* 390 (June 2018), pp. 142–147. ISSN: 03777753. DOI: 10.1016/j.jpowsour.2018.04.035 (cit. on p. 3).

[16] F. Zhang, P. Zhao, M. Niu, and J. Maddy. "The survey of key technologies in hydrogen energy storage". *International Journal of Hydrogen Energy* 41 (33 Sept. 2016), pp. 14535–14552. ISSN: 03603199. DOI: 10.1016/j.ijhydene.2016.05.293 (cit. on p. 3).

[17] C. Wang, F. Wang, C. Li, W. Chen, H. Wang, and L. Lu. "Investigation on energy conversion instability of pump mode in hydro-pneumatic energy storage system". *Journal of Energy Storage* 53 (Sept. 2022), p. 105079. ISSN: 2352152X. DOI: 10.1016/j.est.2022.105079 (cit. on p. 3).

[18] S. Rehman, L. M. Al-Hadhrami, and M. M. Alam. "Pumped hydro energy storage system: A technological review". *Renewable and Sustainable Energy Reviews* 44 (Apr. 2015), pp. 586–598. ISSN: 13640321. DOI: 10.1016/j.rser.2014.12.040 (cit. on p. 3).

[19] J. Du, Y. Liu, X. Mo, Y. Li, J. Li, X. Wu, and M. Ouyang. "Impact of high-power charging on the durability and safety of lithium batteries used in long-range battery electric vehicles". *Applied Energy* 255 (Dec. 2019), p. 113793. ISSN: 03062619. DOI: 10.1016/j.apenergy.2019.113793 (cit. on p. 4).

[20] R. Carter, A. Cruden, and P. J. Hall. "Optimizing for Efficiency or Battery Life in a Battery/Supercapacitor Electric Vehicle". *IEEE Transactions on Vehicular Technology* 61 (4 May 2012), pp. 1526–1533. ISSN: 0018-9545. DOI: 10.1109/TVT.2012.2188551 (cit. on p. 4).

[21] M. Amiri, M. Esfahanian, M. R. Hairi-Yazdi, and V. Esfahanian. "Minimization of power losses in hybrid electric vehicles in view of the prolonging of battery life". *Journal of Power Sources* 190 (2 May 2009), pp. 372–379. ISSN: 03787753. DOI: 10.1016/j.jpowsour.2009.01.072 (cit. on p. 4).

[22] A. A. A. Al-karakchi, G. Lacey, and G. Putrus. "A method of electric vehicle charging to improve battery life". In: IEEE, Sept. 2015, pp. 1–3. ISBN: 978-1-4673-9682-0. DOI: 10.1109/UPEC.2015.7339846 (cit. on p. 4).

[23] M. A. Rahman, X. Wang, and C. Wen. "A review of high energy density lithium–air battery technology". *Journal of Applied Electrochemistry* 44 (1 Jan. 2014), pp. 5–22. ISSN: 0021-891X. DOI: 10.1007/s10800-013-0620-8 (cit. on p. 4).

[24] H. Farzin, M. Fotuhi-Firuzabad, and M. Moeini-Aghtaie. "A Practical Scheme to Involve Degradation Cost of Lithium-Ion Batteries in Vehicle-to-Grid Applications". *IEEE Transactions on Sustainable Energy* 7 (4 Oct. 2016), pp. 1730–1738. ISSN: 1949-3029. DOI: 10.1109/TSTE.2016.2558500 (cit. on p. 4).

[25] B. Jones, R. J. Elliott, and V. Nguyen-Tien. "The EV revolution: The road ahead for critical raw materials demand". *Applied Energy* 280 (Dec. 2020), p. 115072. ISSN: 03062619. DOI: `10.1016/j.apenergy.2020.115072` (cit. on p. 4).

[26] H. Ritchie, M. Roser, and P. Rosado. "Energy". *Our World in Data* (2022). https://ourworldindata.org/energy (cit. on p. 5).

[27] D. Akinyele and R. Rayudu. "Review of energy storage technologies for sustainable power networks". *Sustainable Energy Technologies and Assessments* 8 (Dec. 2014), pp. 74–91. ISSN: 22131388. DOI: `10.1016/j.seta.2014.07.004` (cit. on p. 5).

[28] H. Ritchie, M. Roser, and P. Rosado. "CO and Greenhouse Gas Emissions". *Our World in Data* (2020). https://ourworldindata.org/co2-and-greenhouse-gas-emissions (cit. on pp. 6, 8).

[29] S. Verma, G. Dwivedi, and P. Verma. "Life cycle assessment of electric vehicles in comparison to combustion engine vehicles: A review". *Materials Today: Proceedings* 49 (2022), pp. 217–222. ISSN: 22147853. DOI: `10.1016/j.matpr.2021.01.666` (cit. on p. 7).

[30] R. Kawamoto, H. Mochizuki, Y. Moriguchi, T. Nakano, M. Motohashi, Y. Sakai, and A. Inaba. "Estimation of CO2 Emissions of Internal Combustion Engine Vehicle and Battery Electric Vehicle Using LCA". *Sustainability* 11 (9 May 2019), p. 2690. ISSN: 2071-1050. DOI: `10.3390/su11092690` (cit. on p. 7).

[31] E. Directive. *90/C81/01,"Emission Test Cycles for the Certification of light duty vehicles in Europe", EEC Emission Cycles, 1999* (cit. on p. 8).

[32] M. Tutuianu, P. Bonnel, B. Ciuffo, T. Haniu, N. Ichikawa, A. Marotta, J. Pavlovic, and H. Steven. "Development of the World-wide harmonized Light duty Test Cycle (WLTC) and a possible pathway for its introduction in the European legislation". *Transportation Research Part D: Transport and Environment* 40 (Oct. 2015), pp. 61–75. ISSN: 13619209. DOI: `10.1016/j.trd.2015.07.011` (cit. on p. 8).

[33] J. Merkisz and J. Pielecha. "Selected remarks about RDE test". *Combustion Engines* 166 (3 Aug. 2016), pp. 54–61. ISSN: 2300-9896. DOI: `10.19206/CE-2016-340` (cit. on p. 8).

[34] M. Dinesh, J. K. Pandey, and G. Kumar. "Study of performance, combustion, and NOx emission behavior of an SI engine fuelled with ammonia/hydrogen blends at various compression ratio". *International Journal of Hydrogen Energy* 47 (60 July 2022), pp. 25391–25403. ISSN: 03603199. DOI: 10.1016/j.ijhydene.2022.05.287 (cit. on p. 9).

[35] G. Xin, C. Ji, S. Wang, H. Meng, K. Chang, and J. Yang. "Effect of ammonia addition on combustion and emission characteristics of hydrogen-fueled engine under lean-burn condition". *International Journal of Hydrogen Energy* 47 (16 Feb. 2022), pp. 9762–9774. ISSN: 03603199. DOI: 10.1016/j.ijhydene.2022.01.027 (cit. on p. 9).

[36] L. Liu, Y. Wu, and Y. Wang. "Numerical investigation on the combustion and emission characteristics of ammonia in a low-speed two-stroke marine engine". *Fuel* 314 (Apr. 2022), p. 122727. ISSN: 00162361. DOI: 10.1016/j.fuel.2021.122727 (cit. on p. 9).

[37] C. Kurien and M. Mittal. "Review on the production and utilization of green ammonia as an alternate fuel in dual-fuel compression ignition engines". *Energy Conversion and Management* 251 (Jan. 2022), p. 114990. ISSN: 01968904. DOI: 10.1016/j.enconman.2021.114990 (cit. on p. 9).

[38] D. Han, Y. Liu, and Z. Huang. *The Use of Ammonia as a Fuel for Combustion Engines*. 2022. DOI: 10.1007/978-981-16-8717-4_16 (cit. on p. 9).

[39] H. L. Yip, A. Srna, A. C. Y. Yuen, S. Kook, R. A. Taylor, G. H. Yeoh, P. R. Medwell, and Q. N. Chan. "A Review of Hydrogen Direct Injection for Internal Combustion Engines: Towards Carbon-Free Combustion". *Applied Sciences* 9 (22 Nov. 2019), p. 4842. ISSN: 2076-3417. DOI: 10.3390/app9224842 (cit. on p. 9).

[40] D. Akal, S. Öztuna, and M. K. Büyükakın. "A review of hydrogen usage in internal combustion engines (gasoline-Lpg-diesel) from combustion performance aspect". *International Journal of Hydrogen Energy* 45 (60 Dec. 2020), pp. 35257–35268. ISSN: 03603199. DOI: 10.1016/j.ijhydene.2020.02.001 (cit. on p. 9).

[41] B. Shadidi, G. Najafi, and T. Yusaf. "A Review of Hydrogen as a Fuel in Internal Combustion Engines". *Energies* 14 (19 Sept. 2021), p. 6209. ISSN: 1996-1073. DOI: 10.3390/en14196209 (cit. on p. 9).

[42] A Onorati et al. "The role of hydrogen for future internal combustion engines". *International Journal of Engine Research* 23 (4 Apr. 2022), pp. 529–540. ISSN: 1468-0874. DOI: 10.1177/14680874221081947 (cit. on p. 9).

[43] A. Omari, B. Heuser, and S. Pischinger. "Potential of oxymethylenether-diesel blends for ultra-low emission engines". *Fuel* 209 (Dec. 2017), pp. 232–237. ISSN: 00162361. DOI: 10.1016/j.fuel.2017.07.107 (cit. on p. 9).

[44] J. V. Pastor, J. M. García-Oliver, C. Micó, A. A. García-Carrero, and A. Gómez. "Experimental Study of the Effect of Hydrotreated Vegetable Oil and Oxymethylene Ethers on Main Spray and Combustion Characteristics under Engine Combustion Network Spray A Conditions". *Applied Sciences* 10 (16 Aug. 2020), p. 5460. ISSN: 2076-3417. DOI: 10.3390/app10165460 (cit. on p. 9).

[45] H. L. Chum and R. P. Overend. "Biomass and renewable fuels". *Fuel Processing Technology* 71 (1-3 June 2001), pp. 187–195. ISSN: 03783820. DOI: 10.1016/S0378-3820(01)00146-1 (cit. on p. 9).

[46] T. He, Z. Wang, X. You, H. Liu, Y. Wang, X. Li, and X. He. "A chemical kinetic mechanism for the low- and intermediate-temperature combustion of Polyoxymethylene Dimethyl Ether 3 (PODE3)". *Fuel* 212 (Jan. 2018), pp. 223–235. ISSN: 00162361. DOI: 10.1016/j.fuel.2017.09.080 (cit. on p. 9).

[47] W. J. Pitz and C. J. Mueller. "Recent progress in the development of diesel surrogate fuels". *Progress in Energy and Combustion Science* 37 (3 June 2011), pp. 330–350. ISSN: 03601285. DOI: 10.1016/j.pecs.2010.06.004 (cit. on p. 9).

[48] J. Serrano, F. Arnau, L. García-Cuevas, and V. Farias. "Oxy-fuel combustion feasibility of compression ignition engines using oxygen separation membranes for enabling carbon dioxide capture". *Energy Conversion and Management* 247 (Nov. 2021), p. 114732. ISSN: 01968904. DOI: 10.1016/j.enconman.2021.114732 (cit. on p. 10).

[49] K. Cameron. *Two-Stroke Engines: Defining Their Purpose.* Apr. 2015. URL: https://www.cycleworld.com/2015/04/06/two-stroke-motorcycle-engines-explained-tech-talk-by-kevin-cameron/ (cit. on p. 20).

[50] W. A. Woods and A. Allison. "Effective Flow Area of Piston Controlled Exhaust and Inlet Ports". In: Feb. 1977. DOI: 10.4271/770411 (cit. on p. 21).

[51] A. Dave, A. Siddiqui, D. Probst, and G. J. Hampson. "Development of a Reed Valve Model for Engine Simulations for Two-Stroke Engines". In: Mar. 2004. DOI: 10.4271/2004-01-1455 (cit. on p. 21).

[52] P. R. Hooper, T. Al-Shemmeri, and M. J. Goodwin. "An experimental and analytical investigation of a multi-fuel stepped piston engine". *Applied Thermal Engineering* 48 (Dec. 2012), pp. 32–40. ISSN: 13594311. DOI: 10.1016/j.applthermaleng.2012.04.034 (cit. on p. 21).

[53] D. L. Endicott and W. J. Tervo. "Combustion Chamber Design for Two-Stroke Cross-Flow Outboard Engines". In: Jan. 1962. DOI: 10.4271/620170 (cit. on p. 21).

[54] Z. Xu, F. Ji, S. Ding, Y. Zhao, Y. Wang, Q. Zhang, F. Du, and Y. Zhou. "Simulation and experimental investigation of swirl-loop scavenging in two-stroke diesel engine with two poppet valves". *International Journal of Engine Research* 22 (6 June 2021), pp. 2021–2034. ISSN: 1468-0874. DOI: 10.1177/1468087420916083 (cit. on p. 21).

[55] Y. Zhou, A. Sofianopoulos, B. Lawler, and S. Mamalis. "Advanced combustion free-piston engines: A comprehensive review". *International Journal of Engine Research* 21.(7) (2020), pp. 1205–1230. DOI: 10.1177/1468087418800612 (cit. on pp. 22, 23).

[56] J. Serrano, F. Arnau, P. Bares, A. Gomez-Vilanova, J. Garrido-Requena, M. Luna-Blanca, and F. Contreras-Anguita. "Analysis of a novel concept of 2-stroke rod-less opposed pistons engine (2S-ROPE): Testing, modelling, and forward potential". *Applied Energy* 282 (Jan. 2021), p. 116135. ISSN: 03062619. DOI: 10.1016/j.apenergy.2020.116135 (cit. on pp. 23, 24).

[57] R. Mikalsen and A. Roskilly. "A review of free-piston engine history and applications". *Applied Thermal Engineering* 27 (14-15 Oct. 2007), pp. 2339–2352. ISSN: 13594311. DOI: 10.1016/j.applthermaleng.2007.03.015 (cit. on pp. 24, 25).

[58] G. Regner, D. Johnson, J. Koszewnik, E. Dion, F. Redon, and L. Fromm. "Modernizing the Opposed Piston, Two Stroke Engine for Clean, Efficient Transportation". In: Jan. 2013. DOI: 10.4271/2013-26-0114 (cit. on p. 26).

[59] J. Galindo, H. Climent, J. De la Morena, D. González-Domínguez, S. Guilain, and T. Besançon. "Assessment of air-management strategies to improve the transient performance of a gasoline engine under high EGR conditions during load-decrease operation". *International Journal of Engine Research* 24.(2) (2023), pp. 506–520 (cit. on pp. 33, 38).

[60] J. Galindo, J. R. Serrano, F. J. Arnau, and P. Piqueras. "Description of a Semi-Independent Time Discretization Methodology for a One-Dimensional Gas Dynamics Model". *Journal of Engineering for Gas Turbines and Power* 131 (3 May 2009). ISSN: 0742-4795. DOI: 10.1115/1.2983015 (cit. on pp. 35, 52).

[61] A. Broatch, R. Novella, J. García-Tíscar, and J. Gomez-Soriano. "Potential of dual spray injectors for optimising the noise emission of gasoline partially premixed combustion in a 2-stroke HSDI CI engine". *Applied Thermal Engineering* 134 (Apr. 2018), pp. 369–378. ISSN: 13594311. DOI: 10.1016/j.applthermaleng.2018.01.108 (cit. on p. 38).

[62] A. Broatch, R. Novella, J. García-Tíscar, J. Gomez-Soriano, and P. Pal. "Analysis of combustion acoustic phenomena in compression–ignition engines using large eddy simulation". *Physics of Fluids* 32 (8 Aug. 2020), p. 085101. ISSN: 1070-6631. DOI: 10.1063/5.0011929 (cit. on p. 39).

[63] R. Issa. "Solution of the implicitly discretised fluid flow equations by operator-splitting". *Journal of Computational Physics* 62 (1 Jan. 1986), pp. 40–65. ISSN: 00219991. DOI: 10.1016/0021-9991(86)90099-9 (cit. on p. 39).

[64] V. Yakhot and S. A. Orszag. "Renormalization group analysis of turbulence. I. Basic theory". *Journal of Scientific Computing* 1 (1 1986), pp. 3–51. ISSN: 0885-7474. DOI: 10.1007/BF01061452 (cit. on p. 39).

[65] A. Amsden. *KIVA-3V: A block-structured KIVA program for engines with vertical or canted valves.* Los Alamos National Laboratory (LANL), July 1997. DOI: 10.2172/505339 (cit. on p. 39).

[66] A. Torregrosa, P. Olmeda, B. Degraeuwe, and M. Reyes. "A concise wall temperature model for DI Diesel engines". *Applied Thermal Engineering* 26 (11-12 Aug. 2006), pp. 1320–1327. ISSN: 13594311. DOI: 10.1016/j.applthermaleng.2005.10.021 (cit. on p. 39).

[67]   B. Jia, A. Smallbone, H. Feng, G. Tian, Z. Zuo, and A. Roskilly. "A fast response free-piston engine generator numerical model for control applications". *Applied Energy* 162 (Jan. 2016), pp. 321–329. ISSN: 03062619. DOI: 10.1016/j.apenergy.2015.10.108 (cit. on p. 44).

[68]   B. Jia, Z. Zuo, G. Tian, H. Feng, and A. Roskilly. "Development and validation of a free-piston engine generator numerical model". *Energy Conversion and Management* 91 (Feb. 2015), pp. 333–341. ISSN: 01968904. DOI: 10.1016/j.enconman.2014.11.054 (cit. on p. 44).

[69]   B. Jia, Z. Zuo, H. Feng, G. Tian, A. Smallbone, and A. Roskilly. "Effect of closed-loop controlled resonance based mechanism to start free piston engine generator: Simulation and test results". *Applied Energy* 164 (Feb. 2016), pp. 532–539. ISSN: 03062619. DOI: 10.1016/j.apenergy.2015.11.105 (cit. on p. 45).

[70]   S. H. Chan and J. Zhu. "Modelling of engine in-cylinder thermodynamics under high values of ignition retard". *International Journal of Thermal Sciences* 40 (1 Jan. 2001), pp. 94–103. ISSN: 12900729. DOI: 10.1016/S1290-0729(00)00274-X (cit. on p. 45).

[71]   B. Jia, R. Mikalsen, A. Smallbone, Z. Zuo, H. Feng, and A. P. Roskilly. "Piston motion control of a free-piston engine generator: A new approach using cascade control". *Applied Energy* 179 (Oct. 2016), pp. 1166–1175. ISSN: 03062619. DOI: 10.1016/j.apenergy.2016.07.081 (cit. on p. 45).

[72]   K. Li, C. Zhang, and Z. Sun. "Precise piston trajectory control for a free piston engine". *Control Engineering Practice* 34 (Jan. 2015), pp. 30–38. ISSN: 09670661. DOI: 10.1016/j.conengprac.2014.09.016 (cit. on p. 45).

[73]   H. Feng, C. Guo, B. Jia, Z. Zuo, Y. Guo, and T. Roskilly. "Research on the intermediate process of a free-piston linear generator from cold start-up to stable operation: Numerical model and experimental results". *Energy Conversion and Management* 122 (Aug. 2016), pp. 153–164. ISSN: 01968904. DOI: 10.1016/j.enconman.2016.05.068 (cit. on p. 45).

[74]   J. Dižo, M. Blatnický, M. Sága, and P. Šťastniak. "A Numerical Study of a Compressed Air Engine with Rotating Cylinders". *Applied Sciences* 11 (16 Aug. 2021), p. 7504. ISSN: 2076-3417. DOI: 10.3390/app11167504 (cit. on p. 45).

115

[75] J. Kim, C. Bae, and G. Kim. "Simulation on the effect of the combustion parameters on the piston dynamics and engine performance using the Wiebe function in a free piston engine". *Applied Energy* 107 (July 2013), pp. 446–455. ISSN: 03062619. DOI: 10.1016/j.apenergy.2013.02.056 (cit. on p. 45).

[76] R. Mikalsen and A. Roskilly. "The control of a free-piston engine generator. Part 1: Fundamental analyses". *Applied Energy* 87 (4 Apr. 2010), pp. 1273–1280. ISSN: 03062619. DOI: 10.1016/j.apenergy.2009.06.036 (cit. on p. 45).

[77] R. Mikalsen and A. Roskilly. "The control of a free-piston engine generator. Part 2: Engine dynamics and piston motion control". *Applied Energy* 87 (4 Apr. 2010), pp. 1281–1287. ISSN: 03062619. DOI: 10.1016/j.apenergy.2009.06.035 (cit. on p. 45).

[78] R. Mikalsen and A. Roskilly. "The design and simulation of a two-stroke free-piston compression ignition engine for electrical power generation". *Applied Thermal Engineering* 28 (5-6 Apr. 2008), pp. 589–600. ISSN: 13594311. DOI: 10.1016/j.applthermaleng.2007.04.009 (cit. on p. 45).

[79] M. Dabbaghi, M. Baharom, Z. A. Karim, A. R. A. Aziz, S. E. Mohammed, and E. Z. Z. A. "Comparative evaluation of different heat transfer correlations on a single curved-cylinder spark ignition crank-rocker engineHeat transfer modeling in exhaust systems of high-performance two-stroke engines". *Alexandria Engineering Journal* 60 (3 June 2021), pp. 2963–2978. ISSN: 11100168. DOI: 10.1016/j.aej.2021.01.035 (cit. on p. 45).

[80] P. Olmeda, J. Martín, R. Novella, and R. Carreño. "An adapted heat transfer model for engines with tumble motion". *Applied Energy* 158 (Nov. 2015), pp. 190–202. ISSN: 03062619. DOI: 10.1016/j.apenergy.2015.08.051 (cit. on p. 45).

[81] S.-S. Hou. "Heat transfer effects on the performance of an air standard Dual cycle". *Energy Conversion and Management* 45 (18-19 Nov. 2004), pp. 3003–3015. ISSN: 01968904. DOI: 10.1016/j.enconman.2003.12.013 (cit. on p. 45).

[82] J. M. Luján, H. Climent, P. Olmeda, and V. D. Jiménez. "Heat transfer modeling in exhaust systems of high-performance two-stroke engines". *Applied Thermal Engineering* 69 (1-2 Aug. 2014), pp. 96–104. ISSN:

13594311. DOI: 10.1016/j.applthermaleng.2014.04.045 (cit. on p. 46).

[83] M. S. Lounici, K. Loubar, M. Balistrou, and M. Tazerout. "Investigation on heat transfer evaluation for a more efficient two-zone combustion model in the case of natural gas SI engines". *Applied Thermal Engineering* 31 (2-3 Feb. 2011), pp. 319–328. ISSN: 13594311. DOI: 10.1016/j.applthermaleng.2010.09.012 (cit. on p. 46).

[84] S. Verhelst and C. Sheppard. "Multi-zone thermodynamic modelling of spark-ignition engine combustion – An overview". *Energy Conversion and Management* 50 (5 May 2009), pp. 1326–1335. ISSN: 01968904. DOI: 10.1016/j.enconman.2009.01.002 (cit. on p. 46).

[85] F. Illán and M. Alarcón. "Numerical analysis of combustion and transient heat transfer processes in a two-stroke SI engine". *Applied Thermal Engineering* 30 (16 Nov. 2010), pp. 2469–2475. ISSN: 13594311. DOI: 10.1016/j.applthermaleng.2010.06.018 (cit. on p. 46).

[86] D. Descieux and M. Feidt. "One zone thermodynamic model simulation of an ignition compression engine". *Applied Thermal Engineering* 27 (8-9 June 2007), pp. 1457–1466. ISSN: 13594311. DOI: 10.1016/j.applthermaleng.2006.10.002 (cit. on p. 46).

[87] Y. G. Guezennec and W. Hamama. "Two-Zone Heat Release Analysis of Combustion Data and Calibration of Heat Transfer Correlation in an I. C. Engine". In: Mar. 1999. DOI: 10.4271/1999-01-0218 (cit. on p. 46).

[88] M. Ghiji, S. Edmonds, and K. Moinuddin. "A Review of Experimental and Numerical Studies of Lithium Ion Battery Fires". *Applied Sciences* 11 (3 Jan. 2021), p. 1247. ISSN: 2076-3417. DOI: 10.3390/app11031247 (cit. on p. 46).

[89] F. Catapano, C. Perozziello, and B. M. Vaglieco. "Heat transfer of a Stirling engine for waste heat recovery application from internal combustion engines". *Applied Thermal Engineering* 198 (Nov. 2021), p. 117492. ISSN: 13594311. DOI: 10.1016/j.applthermaleng.2021.117492 (cit. on p. 46).

[90] X. Margot, P. Quintero, J. Gomez-Soriano, and J. Escalona. "Implementation of 1D–3D integrated model for thermal prediction in internal combustion engines". *Applied Thermal Engineering* 194 (July 2021),

p. 117034. ISSN: 13594311. DOI: `10.1016/j.applthermaleng.2021.117034` (cit. on p. 46).

[91]   Z. Yan, B. Gainey, and B. Lawler. "A parametric modeling study of thermal barrier coatings in low-temperature combustion engines". *Applied Thermal Engineering* 200 (Jan. 2022), p. 117687. ISSN: 13594311. DOI: `10.1016/j.applthermaleng.2021.117687` (cit. on p. 46).

[92]   G. Woschni. "A Universally Applicable Equation for the Instantaneous Heat Transfer Coefficient in the Internal Combustion Engine". In: Feb. 1967. DOI: `10.4271/670931` (cit. on p. 47).

[93]   G. Hohenberg. "Advanced Approaches for Heat Transfer Calculations". *SAE International* (1979). DOI: `https://www.jstor.org/stable/44699090` (cit. on p. 48).

[94]   W. J. D. Annand. "Heat Transfer in the Cylinders of Reciprocating Internal Combustion Engines". *Proceedings of the Institution of Mechanical Engineers* 177 (1 June 1963), pp. 973–996. ISSN: 0020-3483. DOI: `10.1243/PIME_PROC_1963_177_069_02` (cit. on p. 48).

[95]   G. Blair. "Design and Simulation of Four-Stroke Engines". *SAE International* (1999) (cit. on p. 49).

[96]   T. I. C. Buidin and F. Mariasiu. "Modeling Approach of an Air-Based Battery Thermal Management System for an Electric Vehicle". *Applied Sciences* 11 (15 July 2021), p. 7089. ISSN: 2076-3417. DOI: `10.3390/app11157089` (cit. on p. 51).

[97]   X. Wang and H. Zhao. "A High-Efficiency Two-Stroke Engine Concept: The Boosted Uniflow Scavenged Direct-Injection Gasoline (BUSDIG) Engine with Air Hybrid Operation". *Engineering* 5 (3 June 2019), pp. 535–547. ISSN: 20958099. DOI: `10.1016/j.eng.2019.03.008` (cit. on p. 52).

[98]   X. Wang and H. Zhao. "Analysis of the Boost System for a High Performance 2-Stroke Boosted Uniflow Scavenged Direct Injection Gasoline (BUSDIG) Engine". In: Sept. 2020. DOI: `10.4271/2020-01-2007` (cit. on p. 52).

[99]   X. Wang and H. Zhao. "Effect of piston shape design on the scavenging performance and mixture preparation in a two-stroke boosted uniflow scavenged direct injection gasoline engine". *International Journal of Engine Research* 22 (5 May 2021), pp. 1484–1499. ISSN: 1468-0874. DOI: `10.1177/1468087419900072` (cit. on p. 52).

[100] R. S. Benson and P. T. Brandham. "A method for obtaining a quantitative assessment of the influence of charging efficiency on two-stroke engine performance". *International Journal of Mechanical Sciences* 11 (3 Mar. 1969), pp. 303–312. ISSN: 00207403. DOI: 10.1016/0020-7403(69)90048-4 (cit. on p. 52).

[101] N. F. Sakellaridis, S. I. Raptotasios, A. K. Antonopoulos, G. C. Mavropoulos, and D. T. Hountalas. "Development and validation of a new turbocharger simulation methodology for marine two stroke diesel engine modelling and diagnostic applications". *Energy* 91 (Nov. 2015), pp. 952–966. ISSN: 03605442. DOI: 10.1016/j.energy.2015.08.049 (cit. on p. 52).

[102] J. Zareei and A. H. Kakaee. "Study and the effects of ignition timing on gasoline engine performance and emissions". *European Transport Research Review* 5 (2 June 2013), pp. 109–116. ISSN: 1867-0717. DOI: 10.1007/s12544-013-0099-8 (cit. on p. 52).

[103] M. I. Foteinos, A. Papazoglou, N. P. Kyrtatos, A. Stamatelos, O. Zogou, and A.-M. Stamatellou. "A Three-Zone Scavenging Model for Large Two-Stroke Uniflow Marine Engines Using Results from CFD Scavenging Simulations". *Energies* 12 (9 May 2019), p. 1719. ISSN: 1996-1073. DOI: 10.3390/en12091719 (cit. on p. 52).

[104] S. Zhu, Y. Gu, H. Yuan, Z. Ma, and K. Deng. "Thermodynamic analysis of the turbocharged marine two-stroke engine cycle with different scavenging air control technologies". *Energy* 191 (Jan. 2020), p. 116533. ISSN: 03605442. DOI: 10.1016/j.energy.2019.116533 (cit. on p. 52).

[105] J.-S. Kim, W.-J. Lee, V. C. Pham, and J.-H. Choi. "A Numerical Study on Fuel Injection Optimization for a ME-GI Dual-Fuel Marine Engine Based on CFD Analysis". *Applied Sciences* 12 (7 Apr. 2022), p. 3614. ISSN: 2076-3417. DOI: 10.3390/app12073614 (cit. on p. 52).

[106] P. B. Moreno. "In-cylinder pressure resonance analysis for trapped mass estimation in automotive engines". Universitat Politècnica de València, Sept. 2017. DOI: 10.4995/Thesis/10251/90423 (cit. on p. 52).

[107] A. P. Carlucci, A. Ficarella, D. Laforgia, and M. Longo. "An Easy and Inexpensive Way to Estimate the Trapping Efficiency of a two Stroke Engine". *Energy Procedia* 82 (Dec. 2015), pp. 17–22. ISSN: 18766102. DOI: 10.1016/j.egypro.2015.11.875 (cit. on p. 52).

[108] R. D. Leo. "Methodologies for Air-Fuel ratio and trapped mass esti-
       mation in Diesel engines using the in-cylinder pressure measurement".
       Energy Procedia 82 (Dec. 2015), pp. 957–964. ISSN: 18766102. DOI:
       10.1016/j.egypro.2015.11.850 (cit. on p. 52).

[109] I. Arsie, R. D. Leo, C. Pianese, and M. D. Cesare. "Estimation of in-
       cylinder mass and AFR by cylinder pressure measurement in automo-
       tive Diesel engines". *IFAC Proceedings Volumes* 47 (3 2014), pp. 11836–
       11841. ISSN: 14746670. DOI: 10.3182/20140824-6-ZA-1003.01602
       (cit. on p. 52).

"If I'm going to fall, I don't want to fall back on anything, I want to fall forward."

Denzel Washington